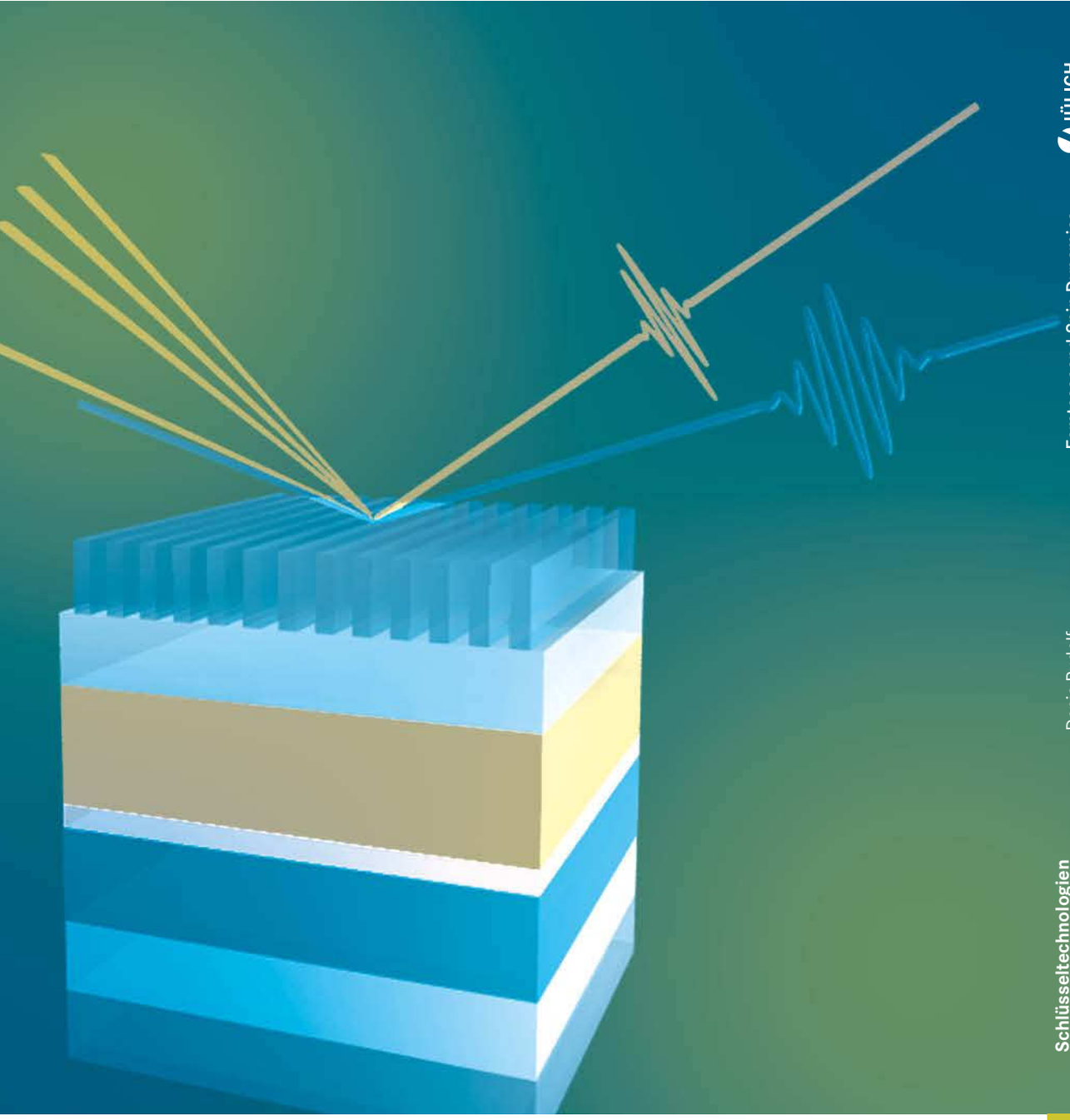

Femtosecond Spin Dynamics

Denis Rudolf

JÜLICH
FORSCHUNGSZENTRUM

Schlüsseltechnologien
Key Technologies

Schlüsseltechnologien / Key Technologies
Band / Volume 70
ISBN 978-3-89336-894-5

JÜLICH
FORSCHUNGSZENTRUM

70

Member of the Helmholtz Association

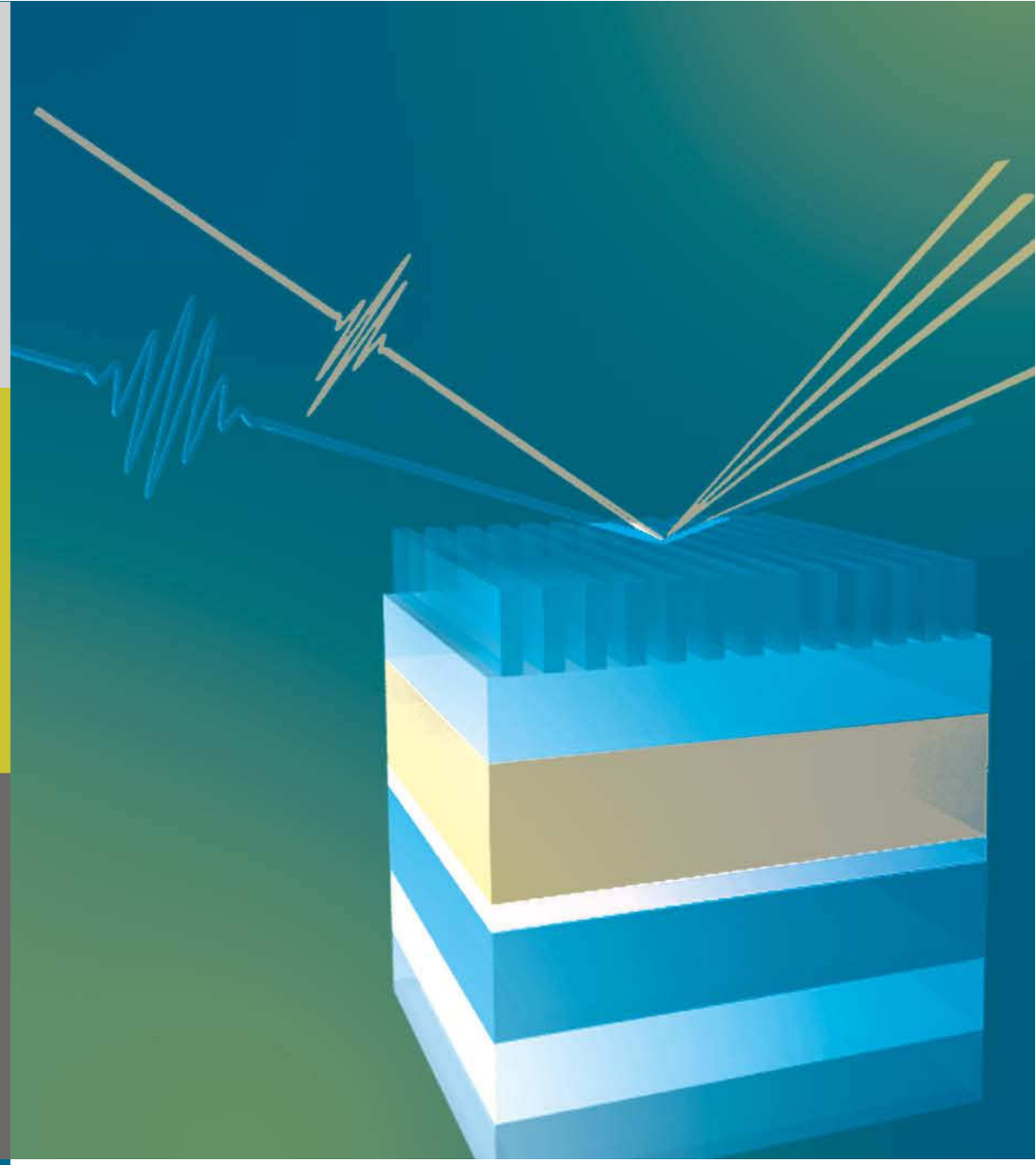

Femtosecond Spin Dynamics in Magnetic Multilayers Employing High Harmonics of Laser Radiation

Denis Rudolf

JÜLICH
FORSCHUNGSZENTRUM

Schriften des Forschungszentrums Jülich
Reihe Schlüsseltechnologien / Key Technologies Band / Volume 70

Forschungszentrum Jülich GmbH
Peter Grünberg Institute (PGI)
Electronic Properties (PGI-6)

Femtosecond Spin Dynamics in Magnetic Multilayers Employing High Harmonics of Laser Radiation

Denis Rudolf

Schriften des Forschungszentrums Jülich
Reihe Schlüsseltechnologien / Key Technologies Band / Volume 70

ISSN 1866-1807 ISBN 978-3-89336-894-5

Bibliographic information published by the Deutsche Nationalbibliothek.
The Deutsche Nationalbibliothek lists this publication in the Deutsche
Nationalbibliografie; detailed bibliographic data are available in the
Internet at http://dnb.d-nb.de.

Publisher and Distributor: Forschungszentrum Jülich GmbH
Zentralbibliothek
52425 Jülich
Tel: +49 2461 61-5368
Fax: +49 2461 61-6103
Email: zb-publikation@fz-juelich.de
www.fz-juelich.de/zb

Cover Design: Grafische Medien, Forschungszentrum Jülich GmbH

Printer: Grafische Medien, Forschungszentrum Jülich GmbH

Copyright: Forschungszentrum Jülich 2013

Schriften des Forschungszentrums Jülich
Reihe Schlüsseltechnologien / Key Technologies, Band / Volume 70

D 464 (Diss., Duisburg, Univ., 2013)

ISSN 1866-1807
ISBN 978-3-89336-894-5

The complete volume is freely available on the Internet on the Jülicher Open Access Server (JUWEL)
at www.fz-juelich.de/zb/juwel

Neither this book nor any part of it may be reproduced or transmitted in any form or by any
means, electronic or mechanical, including photocopying, microfilming, and recording, or by any
information storage and retrieval system, without permission in writing from the publisher.

Zusammenfassung

Ziel dieser Arbeit ist die Untersuchung der laser-induzierten, element-selektiven Spin-Dynamik in ferromagnetischen Schichtsystemen auf der Femtosekunden-Zeitskala. Als Modelsystem dienen zwischenschicht-austausch-gekoppelte Ni/Ru/Fe-Schichten, an denen zeitaufgelöste, element-selektive, magneto-optische Messungen an der 3p Absorptionskante von Eisen (54 eV) und Nickel (67 eV) in der Geometrie des transversalen, magneto-optischen Kerr-Effektes (T-MOKE) durchgeführt wurden. Als Strahlquelle wurden im Neon-Gas erzeugte Hohe Harmonische der 1.5 eV Laser-Strahlung verwendet, deren Pulsdauer weniger als 10 fs beträgt. In Pump-Probe-Experimenten erfolgte die Anregung durch die 1.5 eV Laserpulse und die Messung der Spin-Dynamik durch Pulse von Hohen Harmonischen. Zunächst wurde die element-selektive, temperatur-abhängige Magnetisierungsumkehr der Eisen- und Nickel-Schicht in einem externen Magnetfeld untersucht und die Energie der Zwischenschicht-Austauschkopplung J_1 für die antiferromagnetisch gekoppelten Eisen- und Nickel-Schichten aus Magnetometer-Messungen bestimmt. Im nächsten Schritt wurde die Dynamik von J_1 auf der Femtosekunden-Zeitskala in Pump-Probe-Experimenten sowohl mit einem 3.0 eV Abfragepuls als auch mit Hohen Harmonischen als Abfragepuls gemessen. Zeit-aufgelöste Messungen der magnetischen Hysteresen haben gezeigt, dass J_1 innerhalb von wenigen hundert Femtosekunden nach der Laser-Anregung vorübergehend reduziert wird, und damit der Dynamik der Magnetisierung von Nickel folgt. Darüberhinaus wurden zeit-aufgelöste, schicht-selektive Messungen für parallele und antiparallele Ausrichtung der Magnetisierung der Eisen- und Nickel-Schicht für unterschiedliche Energiedichten der Anregung (Fluenzen) durchgeführt. Das zentrale und überraschende Resultat der Messungen ist, dass die (untere) Eisen-Schicht *für die parallele Ausrichtung* innerhalb eines bestimmten Fluenz-Bereiches zeitweise über ihre Gleichgewichts-Magnetisierung, die vor dem Auftreffen der Laser-Anregung gemessen wurde, "aufmagnetisiert" wurde. *Für die antiparallele Ausrichtung* dagegen, wurde die Eisen-Schicht bei gleicher Fluenz vorübergehend entmagnetisiert. Für die höchste im Experiment erreichte Fluenz wurde die Eisen-Schicht sowohl für die parallele als auch für die antiparallele Ausrichtung demagnetisiert, wenn auch die Demagnetisierung für die

antiparallele Ausrichtung größer ausfiel. Unabhängig von der relativen Magnetisierungs-Ausrichtung und der Fluenz wurde die (obere) Nickel-Schicht immer demagnetisiert. Die Spin-Dynamik in der Eisen-Schicht, die eine deutliche Abhängigkeit von der relativen Ausrichtung zeigt, wurde als eine Folge des superdiffusiven Spin-Transports von der Ni- zu der Eisen-Schicht interpretiert und durch Rechnungen bestätigt. Die Ursache für den Spin-Transport liegt in der unterschiedlichen mittleren freien Weglänge für Majoritäts- und Minoritätselektronen in einem Ferromagneten. Die Übereinstimmung zwischen Rechnungen und Messungen innerhalb eines definierten Fluenz-Bereichs ist sehr gut. Die Abweichungen zwischen Model und Experiment für die höchste im Experiment erreichte Fluenz können darauf zurückgeführt werden, dass auch Spin-Umkehr-Prozesse zu der laser-induzierten Spin-Dynamik auf der Femtosekunden-Zeitskala beitragen.

Abstract

This work explores laser-induced, element-selective, femtosecond spin dynamics in ferromagnetic layered structures. As a model system, interlayer exchange coupled Fe/Ru/Ni layers were investigated in time- and element-selective, magneto-optical measurements at the 3p absorption edges of Fe (54 eV) and Ni (67 eV) in the transversal magneto-optical Kerr effect (T-MOKE) geometry. Spin dynamics was initiated by femtosecond laser excitation with 1.5 eV photon energy. The temporal evolution of magnetization was probed by sub-10 fs pulses of laser high harmonics generated in Ne gas.

First, element-selective, temperature-dependent magnetization reversal of the Fe and Ni layers in external magnetic field is traced and the interlayer exchange coupling energy J_1 is derived for the antiferromagnetically coupled Fe and Ni layers from magnetometer measurements. In the next step, femtosecond dynamics of J_1 is studied in pump-probe experiments with 1.5 eV optical pump and both 3.0 eV and laser high harmonics probe. In time-resolved measurements of magnetic hysteresis, J_1 is transiently quenched on the femtosecond timescale by the action of the pump laser, following the demagnetization of the Ni layer. Moreover, time- and layer-resolved measurements for parallel and antiparallel magnetization orientation of the Fe and Ni layers and for various pump fluences were carried out. The central and surprising result is, that the (buried) Fe layer is transiently magnetized above its equilibrium magnetization prior to laser excitation *for parallel orientation* and demagnetized *for antiparallel orientation* for a defined pump fluence range. For the highest fluence reached in the experiment, the Fe magnetization is quenched for both parallel and antiparallel orientation, albeit, for antiparallel orientation, the quenching is higher. Regardless of the relative orientation of the Ni and Fe magnetization and optical pump fluence, the (top) Ni layer is always demagnetized. The magnetization orientation-dependent spin dynamics in the Fe layer (magnetization for parallel, demagnetization for antiparallel orientation) is interpreted as a consequence of superdiffusive spin transport from the Ni to the Fe layer. The spin transport originates from the different mean free path of majority and minority electrons in a ferromagnet.

Calculations based on the model for superdiffusive spin transport agree well with ex-

perimental data within a defined fluence range. The deviation between the model and measurements for the highest fluence reached in the experiment suggests, that spin-flip processes contribute to laser-induced spin dynamics on the femtosecond timescale.

Contents

1. Introduction **1**

2. Theoretical Background **5**

2.1. Itinerant Ferromagnetism of 3d Metals 5

2.2. Interlayer Exchange Coupling 7

2.3. Magnetization Dynamics 8

2.4. Laser-Induced Femtosecond Spin Dynamics in Ferromagnets 10

2.4.1. Three-Temperature Model 10

2.4.2. Atomistic Spin Models and the Landau-Lifshitz-Bloch Equation . . . 13

2.4.3. Microscopic Models 15

3. Experimental Background **25**

3.1. Non-Resonant and Resonant Magneto-Optical Effects 25

3.2. Laser High Harmonics in Noble Gases 36

3.3. Experimental Setup 41

4. Experimental Results and Discussion **51**

4.1. Static Results 51

4.1.1. Layer-Selective Magnetization of Interlayer Exchange Coupled Fe/Ru/Ni -Layers 51

4.2. Femtosecond Dynamics 63

4.2.1. Laser-Induced Femtosecond Dynamics of Interlayer Exchange Coupling in Fe/Ru/Ni -Layers 63

4.2.2. Laser-Induced Femtosecond Spin Dynamics in Fe/Ru/Ni -Layers . . 69

5. Summary and Outlook **85**

A. Appendix **87**

Bibliography **93**

Publications **117**

Acknowledgements **119**

Curriculum Vitae **121**

1. Introduction

The experimental realization of a bipolar transistor by J. Bardeen and W. H. Brattain in 1947 [1] launched the era of electronic integrated circuits and microelectronic devices such as computers. More and more, the new technology revolutionized everyday life all over the world. An other important development is the emergence of public computer networks and internet starting in the 1990s, which nowadays play a dominant role in economy, politics and science as well as in everyday social and cultural life.

However, the conventional electronics has limitations regarding the power consumption, memory size and reliability. Due to miniaturization of the electronic circuits, quantum mechanical effects such as tunneling have to be taken into account. Therefore, to push the performance of electronic circuits still higher, new concepts have to be explored [2], one of which is based on the manipulation of the electron spin. The birth of a new type of electronics, named spintronics, taking advantage of the electron spin, dates back to the late 1980s, when groups of P. Grünberg and A. Fert independently discovered the Giant Magnetoresistance Effect (GMR) [3, 4], that revolutionized the computer industry. Consequently, the discovery was honored by the Nobel prize in Physics in 2007. Remarkably, if a current is send through two ferromagnetic layers separated by a non-ferromagnetic, nanometer sized metal spacer layer, the resistance depends on the relative magnetization orientation. GMR structures have become state-of-the-art technology in the read heads of hard disc drives, until they were replaced by more efficient magnetic tunnel junctions in 2005.

From the scientific perspective, during the last 25 years a plethora of new physical effects associated with the electronic spin has been discovered [5]. It was predicted [6, 7] and demonstrated [8], that spin-polarized electrons can transfer the transverse spin component to the magnetization and even reverse it through spin-torque transfer. Nowadays, this effect is e.g. applied to write bits in magnetic memory (MRAM) [2]. On the other hand, the spin Hall [9, 10] and inverse spin Hall [11, 12] effects allow the conversion of charge to spin current and vice versa. Spin current generated in a temperature gradient by means of the Spin Seebeck effect [13] is an active area of spintronics research as well

(spincalorics).

Therefore, it is not surprising to see a growing number of spintronic devices like magnetic sensors [14], transistors [15], logics [16, 17] and memory [2] applied in emerging electronic circuits. Notably, during the last ten years a significant progress was achieved in the field of magnetic memory. To increase the areal storage density and to circumvent the superparamagnetic limit, the companies Seagate and Hitachi implemented the technology of perpendicular magnetic recording in 2005-2006. For further progress, new strategies for small magnetic bits, e.g. pre-patterned substrates or magnetic nanoparticles [18] are currently pursued. However, magnetic nanoparticles exhibit an enhanced magnetic anisotropy resulting in higher magnetic fields necessary for the write head of the hard disc drive to reverse the magnetization. With the help of local laser heating (heat-assisted magnetic recording [18]) this problem can be tackled. A different concept of memory was developed by S. S. P. Parkin et al., who introduced the principle of three-dimensional magnetic wires, where magnetic bits are shifted by charge current pulses without any mechanical parts [19].

Apart from the enhancement of the areal storage density of magnetic memory, there is an intense research in progress, which aims to decrease the required time to switch, i.e. write, a magnetic bit. The magnetization can be reversed either by external magnetic fields, by spin-polarized charge currents or by ultrashort, intense laser pulses [20, 21]. For magnetic field and spin-polarized current pulses, the switching time is restricted to hundreds of picoseconds [22], whereas femtosecond laser-induced magnetization reversal in GdFeCo films occurs already after about 30 ps [20].

Not only the field of spintronics is progressing. The last 20 years were also marked by continuous improvements of the technical parameters of lasers pushing the pulse duration to attoseconds. After the first experimental demonstration of a continuous wave ruby laser by T. H. Maiman [23] in 1960, it took about 30 years to build the first Ti:Sapphire-based femtosecond lasers ([24] and references therein). The advent of high peak intensity, ultrashort pulse lasers enabled the generation of laser high harmonics in noble gases [25, 26]. A solid theoretical understanding of high harmonic generation [27] and a continuous optimization of laser parameters such as pulse duration and pulse energy as well as a careful optimization of the high harmonic light sources [28, 29] resulted in new experimental tools taking advantage of attosecond to femtosecond time-resolution [30], photon energies up to several hundreds of eV [31], high coherence and useful photon fluxes [29].

Since the new light sources cover the 3p absorption edges of the important ferromagnets Fe, Co and Ni (50 eV-70 eV), magneto-optical experiments, being hitherto performed

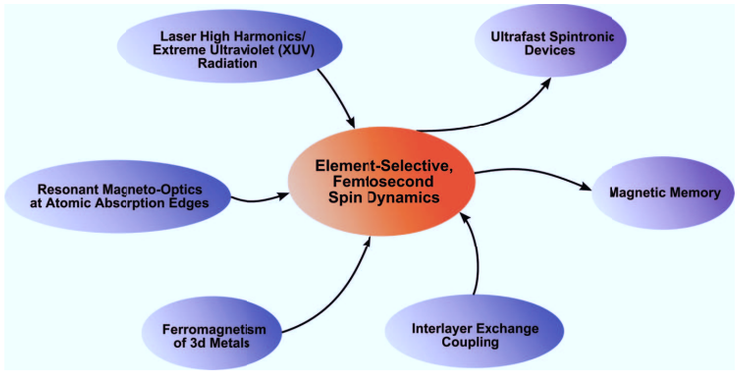

Figure 1.1.: This work is about element-selective, femtosecond spin dynamics in interlayer exchange coupled ferromagnetic layers. The element-selectivity is achieved by means of resonant magneto-optics at atomic absorption edges using laser high harmonics. Possible applications of femtosecond spin dynamics are ultrafast spintronic devices and magnetic memory.

at synchrotron light sources [32–36], became feasible using desktop laser sources within the last few years. Magneto-optical experiments at the elemental absorption edges are superior to measurements with visible light because of the high magnetic contrast (tens of percents), element- and layer-selectivity and, important for imaging and scattering experiments, the small wavelengths (< 30 nm). In addition, the femtosecond to attosecond pulse duration enables time-resolved measurements with high temporal resolution [37].

Many electronic processes such as the dynamics of excited electrons in metals [38] take place on the femtosecond timescale. Surprisingly, E. Beaurepaire et al. showed in 1996 [39], that on a subpicosecond timescale the magnetization of Ni can be transiently quenched after irradiation by an intense, femtosecond laser pulse. This discovery marked the birth of a fascinating research field of laser-induced, ultrafast spin dynamics, which aimes to understand the fundamental interactions among photons, electrons, spins, phonons and magnons as well as to optically manipulate magnetic materials.

This thesis can be allocated to the research fields of magnetism and spintronics applying femtosecond laser-based high harmonics radiation (Fig. 1.1). In particular, it is dedicated to laser-induced, femtosecond spin dynamics in layered structures employing magneto-optical measurements at the 3p absorption edges of the transition metals [40]. As a model

system, we focused on interlayer exchange coupled Fe/Ru/Ni layers. The thesis is structured as follows:

1. The chapter 'Theoretical Background' covers theoretical aspects of ferromagnetism of 3d metals, interlayer exchange coupling and magnetization dynamics. It introduces different models for laser-induced femtosecond spin dynamics in ferromagnets, being currently controversially debated in the scientific community.

2. The chapter 'Experimental Background' treats the fundamentals of the effects being exploited in the experiments such as non-resonant and resonant magneto-optics and laser high harmonic generation in noble gases. Moreover, the experimental setup and its characterization are presented.

3. The chapter 'Experimental Results' presents static and femtosecond dynamic measurements on Fe/Ru/Ni -based layers. First, the static, layer-selective magnetization and magnetization reversal of interlayer exchange-coupled Fe/Ru/Ni trilayers was investigated using laser high harmonics. Second, femtosecond dynamics of the interlayer exchange coupling energy J_1 was measured and the relevant physical processes are discussed on a qualitative basis. Third, time- and layer-selective spin dynamics of Fe/Ru/Ni -based layers was measured and compared with calculations based on the superdiffusive spin transport theory [41]. Good agreement between the theory and experiment for a moderate laser excitation corroborates the presence of laser-induced spin transport on the femtosecond timescale.

2. Theoretical Background

2.1. Itinerant Ferromagnetism of 3d Metals

3d metals (Scandium to Zinc) belong to the group of technologically important materials. It is well known, that 3d metals Fe, Co and Ni are ferromagnetically ordered at room temperature. The ferromagnetic order is caused by delocalized (itinerant) 3d electrons [42]. The magnetic moment per atom of Fe, Co and Ni is predominantly carried by the spin angular momentum of the electron and amounts to 2.2 Bohr magnetons (μ_B) for Fe, 1.7 μ_B for Co and 0.6 μ_B for Ni, respectively [22]. In contrast to atoms and molecules, the magnetic moment of solid state Fe, Co and Ni is a non-integer number, which reflects the itinerant character of their ferromagnetic order [42]. The contribution to the magnetic moment arising from the orbital angular momentum of 3d electrons amounts to about 0.1 μ_B [22].

The origin of magnetism in 3d metals can be understood based on the model of free electrons [42]. Initially, the density of states is equally filled with spin-up and spin-down electrons. A transfer of spin-down to spin-up density results in an increase of the total kinetic energy. On the other hand, this also results in a reduction and gain of the Coulomb energy, because the average distance between the spin-up electrons is increased [42, 43]. The physical origin of that is the Pauli principle. In the case of two electrons with parallel spin, the spatial part of the two particle wave function must be antisymmetric when the two electrons are exchanged, which doesn't allow two electrons with equal spin quantum number to be very close to each other [44]). Thus, ferromagnetism arises from the competition between the kinetic and the Coulomb energy.

Ferromagnetism can be explained from the perspective of the band structure (Stoner-Wohlfarth model [44]), where the d bands of spin-up and spin-down electrons are shifted with respect to each other by the Stoner exchange energy, which is about 1 eV for Fe, Co and Ni [22]. Spin-up and spin-down bands are filled according to the Fermi-Dirac statistics and the magnetization reads

$$M = \mu_B \frac{n_\uparrow - n_\downarrow}{V} \ , \tag{2.1}$$

where $n_{\uparrow,\downarrow}$ denotes the total number of spin-up and spin-down electrons, respectively, and V denotes the volume of the sample. In the Stoner-Wohlfarth model, the temperature-dependence of the magnetization is due to the temperature-dependence of the Fermi-Dirac distribution [22, 44].
The basic idea, that one-electron energies $E(k)$ are reduced due to the Coulomb interaction with other electrons, can be expressed in a mean-field approach by [44]

$$E_{\uparrow} = E(k) - I \cdot n_{\uparrow}/N \tag{2.2}$$

$$E_{\downarrow} = E(k) - I \cdot n_{\downarrow}/N \ , \tag{2.3}$$

with I being the material-specific Stoner parameter (in eV) and N the total number of atoms. The Stoner parameter I represents the exchange interaction and describes the reduction of the one-electron energies due to electron correlations [44]. It can be shown, that ferromagnetism occurs, if the product of the density of states at the Fermi level, $D(E_F)$, and I is sufficiently high [44], which is expressed by

$$I \cdot \frac{V}{2N} D(E_F) > 1 \ . \tag{2.4}$$

For 3d metals, Eq. 2.4, which is called the Stoner criterion, is only satisfied for Fe, Co and Ni.
Due to the Pauli principle, the probability to find two electrons with equal spin quantum number at the same spatial coordinate is zero. Consequently, two electrons with the same spin are spatially separated and therefore, they gain Coulomb energy. From the point of view of one arbitrary electron, the surrounding charge density is reduced due to the reduced probability to find electrons with the same spin in its neighbourhood (exchange hole) [42, 44].
Reaching the Curie temperature T_C, the macroscopic, spontaneous magnetization M_S vanishes and the material undergoes a phase transition from the ferromagnetic to paramagnetic state. The Curie temperatures of Fe, Co and Ni are 1043 K, 1388 K, 631 K, respectively [22]. The Stoner model greatly overestimates T_C and predicts, that M_S and atomic magnetic moments vanish simultaneously [42]. In itinerant ferromagnets Fe, Co and Ni, M_S is strongly reduced close to T_C because of randomization of the direction of atomic magnetic moments, but their magnitude is nearly preserved [42]. The temperature-dependence of M_S is well described in mean-field models, where the interaction between spins is mapped onto the problem of non-interacting spins placed in a effective magnetic field, which arises from the surrounding spins [42]. At temperatures close to T_C, long-range spin fluctuations have to be considered [42, 45], whereas at low temperatures, M_S

is reduced by spin waves [22, 44].
Spin waves are collective excitations of a large number of spins, which can be excited at very low energies and exhibit a quadratic dispersion relation [22, 44]. Like phonons, spin waves are quasi-particles, which carry the angular momentum of $\pm\hbar$. On the average over the whole sample, they reverse one single spin [44]. In contrast to collective excitations, one single spin can also be reversed, if one spin-up electron from the filled majority band is excited to empty minority band above the Fermi level (Stoner excitation) [45].

2.2. Interlayer Exchange Coupling

Interlayer exchange coupling (IEC) occurs between the magnetization of two or more ferromagnetic layers, which are separated by a non-ferromagnetic interlayer. Considering two ferromagnetic layers FM_1 and FM_2, which magnetization vectors M_1 and M_2 enclose the angle Θ, the energy term due to IEC can be written as a series [46]

$$E = -J_1 \cos\Theta - J_2 \cos^2\Theta + ... \,, \tag{2.5}$$

where higher order terms are usually negligible. If J_2 is negligible and $J_1 < 0$, M_1 and M_2 are aligned antiparallel to minimize E. For $J_1 > 0$, M_1 and M_2 are aligned parallel. In case J_1 is negligible, 90°-coupling of M_1 and M_2 is established for $J_2 < 0$.
For metallic interlayers, oscillations of J_1 as a function of the interlayer thickness d are

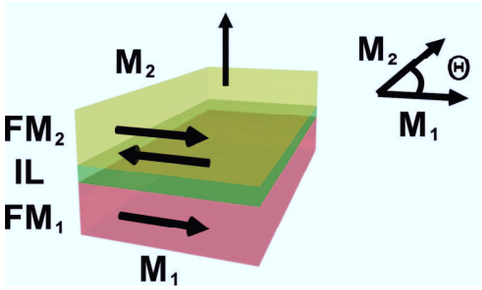

Figure 2.1.: Trilayer comprising two ferromagnetic layers FM_1 and FM_2 and a non-ferromagnetic interlayer IL. The magnetizations M_1 and M_2 of FM_1 and FM_2 enclose the angle Θ. According to Eq. 2.5, the interlayer exchange coupling between M_1 and M_2 can be either parallel, antiparallel or 90°-coupling [46].

observed [46, 47]. These oscillations are attributed to spin-polarized, standing electron waves inside the interlayer IL perpendicular to the interfaces [46] (quantum interferences [48]). The condition for the standing electron waves to occur reads [46]

$$2|\boldsymbol{k}_\perp| = n\frac{2\pi}{d},\ n = 1, 2, 3, \dots\ , \tag{2.6}$$

where $\boldsymbol{k}_\perp$ denotes the wave vector component inside the interlayer perpendicular to the layers and $\boldsymbol{k} = \boldsymbol{k}_\parallel + \boldsymbol{k}_\perp$ is located on the Fermi surface of the interlayer material. As a consequence of Eq. 2.6, the oscillation period of J_1 is $2|\boldsymbol{k}_\perp|$. The highest contribution to standing electron waves arises from those $\boldsymbol{k}_\perp$ from the Fermi surface, which are most occupied. In real materials of the spacer layer, multiple $|\boldsymbol{k}_\perp|$ with a high density of states may exist simultaneously depending on the Fermi surface, which results in superposition of multiple oscillation periods.

The oscillation of J_1 as a function of d is explained in the Bruno model of interlayer exchange coupling [48]. The interference of the electron wave reflected multiple times from the interfaces FM_1/IL and IL/FM_2 induces an oscillation of the density of states in the spacer layer depending on d. For example, the density of states is increased for constructive interference and decreased for destructive interference. The oscillations of the density of states are transferred to oscillations of the energy. For ferromagnetic layers FM_1 and FM_2, the reflection amplitudes are spin-dependent. Consequently, J_1 can be calculated as energy difference between the parallel and antiparallel magnetization alignment of FM_1 and FM_2.

2.3. Magnetization Dynamics

Magnetization dynamics in ferromagnetic films, i.e. temporal and spatial changes of magnetization $\boldsymbol{M}(\boldsymbol{x}, t)$ due to applied external magnetic fields and charge currents as well as due to illumination with laser pulses, span a large range of timescales from years to femtoseconds [22]. Some examples of magnetization dynamics are thermally activated domain wall movement on the timescale of seconds [49], magnetization precession and reversal on the timescale of nano- and picoseconds [22] and laser-induced magnetization dynamics on the femtosecond timescale [50].

A widely studied phenomenon is the damped magnetization precession, where the magnetization $\boldsymbol{M}(\boldsymbol{x}, t)$ precesses around the effective magnetic field $\boldsymbol{H_{eff}}(\boldsymbol{x}, t)$ and simultane-

ously relaxes towards the orientation of $\boldsymbol{H_{eff}}$ [51]. This phenomenon is described by the Landau-Lifshitz-Gilbert (LLG) equation [51, 52]

$$\frac{d\boldsymbol{M}}{dt} = -\frac{\gamma_{gm}}{1+\alpha^2}(\boldsymbol{M} \times \boldsymbol{H_{eff}}) - \frac{\alpha\,\gamma_{gm}}{|\boldsymbol{M}|(1+\alpha^2)}[\boldsymbol{M} \times (\boldsymbol{M} \times \boldsymbol{H_{eff}})] \,, \tag{2.7}$$

where γ_{gm} denotes the gyromagnetic ratio, α the Gilbert damping and $\boldsymbol{H_{eff}}$ the effective magnetic field, which contains contributions from ferromagnetic exchange, external magnetic fields, magneto-static stray fields and magneto-crystalline anisotropy [51]. The microscopic origin of damping and relaxation is due to electron-magnon, electron-phonon and magnon-magnon interactions [42].

The LLG equation is useful, e.g. to model nanosecond dynamics of magnetic vortex in a high frequency magnetic field [53]. On the other hand, the LLG theory assumes the magnitude of the magnetization, $|\boldsymbol{M}|$, to be constant in time. Contrary to that, a quenching of $|\boldsymbol{M}|$ in 3d ferromagnets on the femtosecond timescale has been observed experimentally [50]. Therefore, new models to explain laser-induced femtosecond spin dynamics in ferromagnets have been developed. Some of the most frequently used models are presented in the next chapter.

2.4. Laser-Induced Femtosecond Spin Dynamics in Ferromagnets

Since the first studies of the interaction between laser pulses and ferromagnets by M. B. Agranat et al. [54], G. L. Bona et al. [55] and A. Vaterlaus et al. [56, 57], many new effects related to the manipulation of magnetization by short light pulses have been discovered. Some of them together with their interpretation are summarized in the Appendix (Tab. A.1). Despite a considerable progress in theory and modeling of femtosecond spin dynamics, up to now, the microscopic processes are not fully understood yet. This can be attributed to the complex interactions between photons, charge- and spin-carriers, phonons and magnons in thermal non-equilibrium. In this chapter, a short review of the models proposed to explain ultrafast spin dynamics is given. We start with phenomenological models, which are the Three-Temperature Model, Atomistic Spin Models and Landau-Lifshitz-Bloch equation. Microscopic theories including the Zhang-Hübner model, coherent spin-photon coupling, interaction between charge- and spin-carriers, phonons and magnons as well as the superdiffusive spin transport are discussed in the second half of this chapter.

2.4.1. Three-Temperature Model

The Three-Temperature Model assumes, that the solid can be described by three thermodynamic, interacting subsystems, electrons, phonons and spins. They are considered to be thermal reservoirs, which can exchange energy among each other and are in internal but not external equilibrium [39, 54, 58]. Initially, in a typical laser-based pump-probe experiment, the energy is deposited by the laser pulse into the electronic subsystem via optical excitations from the valence bands to the unoccupied states above the Fermi level. After the thermal equilibration of the electron population to the Fermi-Dirac distribution via electron-electron interactions, which takes about 100 fs for Ni [59], the energy is transferred to the phonons and spins. Neglecting the spins for a moment, the thermal energy flow from the electrons to the phonons is governed by the two following coupled, nonlinear differential equations [60]

$$C_e(T_e(t))\frac{dT_e(t)}{dt} = -G_{ep}\left[T_e(t) - T_p(t)\right] + P(t) \tag{2.8}$$

$$C_p(T_p(t))\frac{dT_p(t)}{dt} = -G_{ep}\left[T_p(t) - T_e(t)\right] \ , \tag{2.9}$$

where $T_e(t)$, $T_p(t)$ and $C_e(T_e(t))$, $C_p(T_p(t))$ are the electronic and phononic temperatures and temperature-dependent heat capacities, respectively. $P(t)$ denotes the optical power volume density of the laser pulse and G_{ep} is the electron-phonon coupling constant, which is assumed to be temperature-independent.
Given, that C_e and C_p are nearly constant within the relevant temperature range, the electron-phonon equilibration time is

$$\tau_{ep} = \frac{C_e \cdot C_p}{C_e + C_p} G_{ep}^{-1} \tag{2.10}$$

and amounts to about 0.6 ps for Ni [59].
The cooling of the thermalized electron system proceeds not only via electron-phonon coupling, but also by diffusive electron transport, which can be simulated by adding $\partial/\partial z\ (K_e\ \partial/\partial z\ T_e(z))$ on the right side of Eq. 2.8 [62, 63]. Here, z denotes the depth coordinate of the sample and K_e the electronic heat conductivity.
Taking the spin subsystem into account, the differential equations can be extended in a straightforward manner to [39]

$$C_e(T_e(t))\frac{dT_e(t)}{dt} = -G_{ep}\left[T_e(t) - T_p(t)\right] - G_{es}\left[T_e(t) - T_s(t)\right] + P(t) \tag{2.11}$$

$$C_p(T_p(t))\frac{dT_p(t)}{dt} = -G_{ep}\left[T_p(t) - T_e(t)\right] - G_{sp}\left[T_p(t) - T_s(t)\right] \tag{2.12}$$

$$C_s(T_s(t))\frac{dT_s(t)}{dt} = -G_{es}\left[T_s(t) - T_e(t)\right] - G_{sp}\left[T_s(t) - T_p(t)\right]\ . \tag{2.13}$$

Here, $C_s(T_s(t))$ is the heat capacity of the spin subsystem and G_{sp} and G_{es} denote the temperature-independent spin-phonon and electron-spin coupling constants. In a different approach, R. Chimata et al. [58] considered only the coupling between electrons and spins and neglected the spin-phonon interaction.
For Ni, the heat capacities can be determined as follows. It is known, that the heat capacity for conduction electrons is given by $C_e(T) = \gamma T$ [44] with $\gamma = 0.98 \cdot 10^3$ $\mathrm{Jm^{-3}K^{-2}}$ for Ni [61]. Furthermore, $C_p(T)$ can be determined from the Debye model [44] and, consequently, $C_s(T) = C_{total}(T) - C_e(T) - C_p(T)$ can be calculated from the measured total heat capacity $C_{total}(T)$ (Fig. 2.2). At $T = 300$ K, C_e is about one order of magnitude, C_s even about two orders of magnitude smaller than C_p, which is nearly constant in the whole temperature range from 200 K to 1600 K (Fig. 2.2). If the temperature is rising, $C_e(T)$ increases linearly with T, while C_s becomes discontinuous due to the ferromagnetic to paramagnetic phase transition at the Curie temperature, but still stays well below C_p at elevated temperatures.
To simulate the temperature dynamics and equilibration times between the three reservoirs

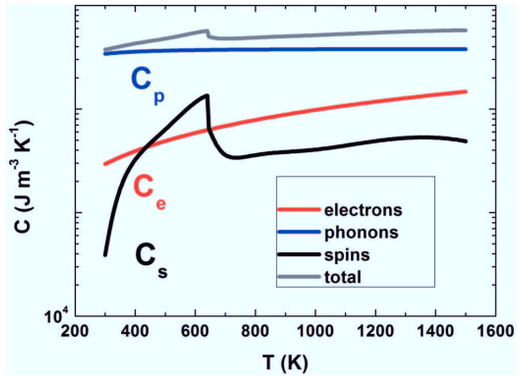

Figure 2.2.: Temperature-dependent heat capacity C_P for Ni [61] decomposed into the contributions from electrons, phonons and spins. The transition from the ferro- to the paramagnetic phase around T_C=640 K is evident in the spin contribution.

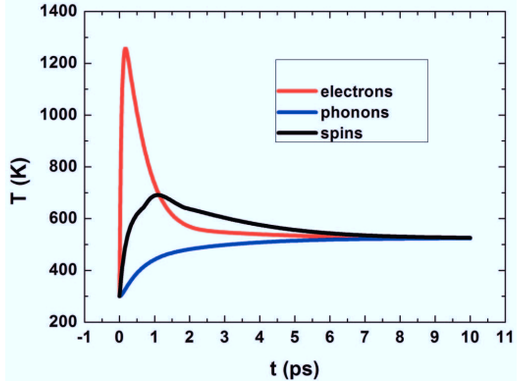

Figure 2.3.: Electron, phonon and spin temperatures of Ni after heating with a 100 fs laser pulse with 1.3 mJ cm^{-2} absorbed fluence, calculated using Eq. 2.11-2.13. The heat capacities are from Fig. 2.2, whereas the coupling constants G_{ep}, G_{es} and G_{sp} are from [39].

for Ni, heat capacities [61] and coupling constants $G_{ep} = 8{\cdot}10^{17}$ W m^{-3} K^{-1}, $G_{es} = 6{\cdot}10^{17}$ W m^{-3} K^{-1} and $G_{sp} = 0.3{\cdot}10^{17}$ W m^{-3} K^{-1} [39] are used as input parameters for Eq. 2.11-2.13, which are solved numerically. The results are shown in Fig. 2.3. First, the electron system is heated by the laser pulse to about twice the Curie temperature. Energy is then rapidly transfered to the spin system, which temperature rises on the sub-picosecond time scale. Within few ps, the energy is then gradually transfered to the phonons with moderate temperature increase due to their high heat capacity compared to the electrons and spins (Fig. 2.2). The three reservoirs are in thermal equilibrium after about 10 ps. On the longer time scale, the heat is conducted into the substrate, which is not included in the model.

While the laser-induced, transient changes of the reflectivity can in some cases be related to the electron temperature ([62] and references therein), the spin temperature cannot be directly accessed by transient changes of the magneto-optical quantities such as the Kerr rotation and ellipticity as well as the magnetic asymmetry. Recently, N. Kazantseva et al. [64] raised doubts, whether the concept of the spin temperature is at all adequate for a non-equilibrium spin system. Based on the stochastic Landau-Lifshitz-Gilbert equation with a classical spin Hamiltonian, they showed, that the spin temperature can exceed the Curie point without complete microscopic demagnetization. Furthermore, the recovery of the microscopic magnetization can be much slower than the recovery of the spin temperature. In addition, the temperature of the spin-up and spin-down subsystems is not necessarily the same [65], which is not accounted for in the model. An alternative approach is to consider three reservoirs comprising spin-up and spin-down electrons as well as phonons [66].

2.4.2. Atomistic Spin Models and the Landau-Lifshitz-Bloch Equation

For future progress in magnetism and, particulary, in spin dynamics, it is desirable to connect different theoretical approaches, starting from the Spin Density Functional Theory (SDFT) via atomistic spin models towards macrospin micromagnetic models [58, 67]. The parameters needed for atomistic spin models like the exchange or anisotropy constants, can be calculated from SDFT. On the other hand, from the atomistic spin models, the equilibrium, temperature-dependent magnetization and susceptibility can be computed and used as input for micromagnetic models.

Recently, atomistic spin models have been applied to model laser-induced femtosecond spin

dynamics in the ferromagnetic Ni [64] and in the ferrimagnetic GdFeCo alloy [20, 21, 68]. The starting point is the Hamiltonian

$$H = -\frac{J_{atom}}{2}\sum_{ij}\boldsymbol{S}_i \cdot \boldsymbol{S}_j - D\sum_i (S_i^z)^2 - \mu_S \boldsymbol{B}\cdot\sum_i \boldsymbol{S}_i \ , \tag{2.14}$$

where z is the quantization axis, $\boldsymbol{S}_i$ the spin on the lattice site i, J_{atom} the exchange integral, D the anisotropy constant, μ_S the spin magnetic moment and $\mu_0\boldsymbol{B}$ is the external magnetic field. The spin dynamics is calculated using the stochastic Landau-Lifshitz-Gilbert equations [21, 64]

$$\frac{\partial \boldsymbol{S}_i(t)}{\partial t} = -\frac{\gamma_{gm}}{(1+\lambda_{LLG}^2)\mu_S}\left[\boldsymbol{S}_i(t)\times\boldsymbol{H}_i(t) + \lambda_{LLG}\boldsymbol{S}_i(t)\times(\boldsymbol{S}_i(t)\times\boldsymbol{H}_i(t))\right] \tag{2.15}$$

$$\boldsymbol{H}_i(t) = -\frac{\partial H}{\partial \boldsymbol{S}_i} + \boldsymbol{h}_i(t) \tag{2.16}$$

$$\left\langle h_i^a(t) h_j^b(t')\right\rangle = \delta_{ij}\delta_{ab}\delta(t-t')2\mu_S\lambda_{LLG}k_BT/\gamma_{gm} \ , \tag{2.17}$$

with γ_{gm} being the gyromagnetic ratio and, important for modeling of ultrafast spin dynamics, λ_{LLG} is the coupling between the electron and spin bath. Thermal fluctuations are included via Eq. 2.17, where the brackets $\langle ...\rangle$ denote the thermal average [69], i,j are the lattice sites and a,b the Cartesian coordinates.

The pump laser pulse, which heats the bath of conduction electrons, is mimicked by a heat pulse and the coupling strength between the electron and the spin bath is determined by λ_{LLG}. Subsequently, the electron bath cools down due to the energy transfer to the phonon bath following the Two-Temperature-Model (Eq. 2.8-2.9). Note, that although electron and phonon temperatures are well defined assuming internal equilibrium, for a non-equilibrium spin ensemble, the concept of temperature is still questionable [64]. If one considers a continuous, spatially averaged density of magnetic moments, i.e. the magnetization, rather than single atomic spins, the usual micromagnetic approach is based on the Landau-Lifshitz-Gilbert (LLG) equation [52], which describes the damped precessional motion of magnetization in the presence of an effective magnetic field. The restriction of the LLG equation is, that the magnitude of magnetization is conserved. However, to adequately treat laser-induced femtosecond spin dynamics, first, the longitudinal relaxation, i.e. the change in the magnitude of magnetization, and second, the temperature dependence of micromagnetic parameters and effective magnetic fields below and above T_C have to be taken into account [70]. Such a micromagnetic equation, called Landau-Lifshitz-Bloch (LLB) equation, has been derived by D. A. Garanin [71]. Similar to the stochastic Landau-Lifshitz-Gilbert equation, the coupling between the electron and spin

bath is given by λ_{LLB} and the time-dependent electron temperature is computed from the Two-Temperature-Model. U. Atxitia et al. showed the ability of the LLB approach to model femtosecond spin dynamics in Ni [70, 72] as well as Co and Gd [73] and found, for certain conditions, that their model is equivalent to the microscopic model proposed by B. Koopmans et al. [74], which will be discussed in the second half of the chapter 2.4.3 in more detail.

2.4.3. Microscopic Models

Zhang-Hübner Model

The Zhang-Hübner model ([75] and references therein) is a quantum-mechanical theory to describe the laser-induced demagnetization on the femtosecond timescale. In short, the main assumptions of the theory are [75]:
1. One monolayer of Ni is treated with a Hubbard-like Hamiltonian H, which includes the band structure and spin-orbit coupling.
2. The wavefunction at $t = 0$ reads

$$\Psi(t=0) = \sum_{kl} c_{kl} \exp\left(-(\omega - E_{kl})^2/\tau_{laser}^2\right)\phi_{kl} \ ,$$

with ϕ_{kl} being the eigenstate of momentum k and band l, E_{kl} the eigenenergy of the state kl, τ_{laser} the laser pulse duration, ω the central angular frequency of the laser pulse and c_{kl} the normalization factor. The dynamics are calculated by solving the time-dependent Schrödinger equation

$$i\hbar\frac{\partial}{\partial t}\Psi = H\Psi \ .$$

Note, that only the pump and not the probe laser field is taken into account.
3. The intrinsic quantities such as the expectation value of the spin angular momentum $S_z(t) = \left\langle \Psi(0)|\hat{S}_z|\Psi(t)\right\rangle$ and the total particle number $N(t) = \left\langle \Psi(0)|\hat{N}|\Psi(t)\right\rangle$ as well as the linear and non-linear optical and magneto-optical susceptibilities are computed.
The variation of model parameters, the exchange interaction J_{ZH}, the spin-orbit coupling λ_{ZH}, the degree of electron localization and the pulse duration of the optical pump lead to a deeper understanding of the ultrafast charge and spin dynamics within the Zhang-Hübner model. The main results are [75]:
1. If the exchange interaction J_{ZH} is increased, it accelerates the spin relaxation (demagnetization) time τ_M. The scaling is approximately $\tau_M \sim 1/J_{ZH}$. Note, that, by chance or not, the model proposed by B. Koopmans et al. [76] predicts the same scaling.

2. An increase of the spin-orbit coupling λ_{ZH} results in faster τ_M.
3. The spin response is delayed with respect to the charge response both in the intrinsic quantities $S_z(t)$ and $N(t)$ as well as in the susceptibilities.
4. The more the electrons are localized, the slower is the dynamics. This remarkable prediction can be compared to time-resolved experiments on half-metals and magnetic dielectrics [50], where, indeed, a slowing down of the demagnetization time was observed.
5. The shorter the laser pulse, the faster is the dynamics.

Recently, G. P. Zhang et al. [77–79] addressed the question of the connection between the magneto-optical effects and the genuine spin dynamics in femtosecond laser pulse experiments, which was also disputed by some other authors (e.g. [80, 81]). For the case of Ni, G. P. Zhang et al. showed, that the magneto-optical and the spin response for pump photon energies below 2 eV are correlated, whereas above 2 eV, the temporal evolution of the magneto-optical and the spin response significantly deviates from each other. In addition, if the pump laser pulses are as short as 12 fs, the magneto-optical response precedes the genuine spin response.

Coherent Spin-Photon Coupling

In [82], J.-Y. Bigot et al. report about experimental evidence for coherent spin-photon coupling being present in Ni and $CoPt_3$ films during the femtosecond laser pulse excitation. In single pulse experiments, they showed, that the Faraday ellipticity and rotation, normalized to the transmitted energy density, significantly decrease, if the laser pulse is sufficiently intense. In pump-probe experiments with parallel and perpendicular polarization orientation of the linearly polarized pump and probe pulses, the authors found coherent electronic and magnetic contributions. They noticed, referring to a relativistic single particle Hamiltonian, that spin-photon coupling is provided by the Zeeman and spin-orbit interaction. Following this work, H. Vonesch and J.-Y. Bigot [83] developed a model combining the relativistic single particle Hamiltonian with the density matrix formalism to calculate the time-resolved magneto-optical response. In eight fine-structure levels of a hydrogen-like atom, the electron is exposed to static and pulsed laser electromagnetic fields and, additionally, the magneto-optical response is calculated using the first and third order polarizations of the atom. Indeed, although being a small effect, the authors found 0.2 % demagnetization induced by coherent spin-photon coupling and showed, that both, the spin and orbital angular momentum, contribute to the population dynamics.

Interaction between Charge-, Spin-Carriers, Phonons and Magnons

In the Three-Temperature model (Chapter 2.4.1), the energy transfer between the charge carriers (electrons and holes), phonons and spins is considered, but no attention is payed to the transfer of angular momentum between the three reservoirs. A sizable demagnetization can be microscopically interpreted as spin-flip scattering of electrons, where plenty of the majority electrons reverse their spin. For the reason of angular momentum conservation, the spin has to be transferred to elementary excitations, e.g. phonons or magnons. Initially, it was not clear, whether the angular momentum transfer to the lattice can occur on the sub-ps timescale, when the electron and phonon systems are not yet in thermal equilibrium. To address this issue, B. Koopmans et al. [84] developed a model of ultrafast demagnetization based on electron-phonon spin-flip scattering. The assumptions of the model are the following:

1. The electrons are spinless particles with a constant density of states. In their internal, thermal equilibrium, the occupation number $n_e(E, T_e)$ follows from the Fermi-Dirac distribution. Therefore, once $n_e(E, T_e)$ is known for a certain time t, the electronic temperature $T_e(t)$ can be calculated.

2. The lattice is described as an ensemble of harmonic oscillators with a constant density of modes with equal energy E_p being in internal equilibrium. The occupation number $n_p(E_p, T_p)$ follows from the Bose-Einstein distribution, from which $T_p(t)$ can be derived.

3. The spin system comprises an ensemble of identical two-level systems obeying the Boltzmann statistics. The energy between the two levels, E_m, depends linearly on the average spin density $s(T_s)$, which is the ensemble-averaged expectation value of the spin operator S_z. From the knowledge of $s(T_s)$, the spin temperature $T_s(t)$ can be derived. Like the electrons and phonons, the spins are assumed to be in internal equilibrium.

4. Initially, the electrons with the energy E are excited by the laser pulse with the photon energy $\hbar\omega$ to the states with the energy $E + \hbar\omega$. Subsequently, the three systems can interact with each other in the following way. First, electron-phonon scattering, which takes place with a constant rate K_{ep}, can be either spin-conserving or not, described by the Elliot-Yafet spin-flip probability α_{EY} [85]. If the electron reverses its spin in the electron-phonon collision, the excess angular momentum is transferred to the lattice. Furthermore, electron-electron collisions are also included in the model and take place with a constant rate K_{ee}.

The dynamics of $n_e(t)$, $n_p(t)$ and $s(t)$ is calculated using three coupled Boltzmann "Stosszahlansatz" equations [38]. Following the above points, it was found, that the demagnetization

can be faster than the electron-phonon equilibration time.
In further publications [74, 76, 86, 87], the model was reformulated in the sense, that a Hamiltonian, which describes the interactions among the three systems, was introduced in the occupation-number representation, but the assumptions 1.-4. remained valid. B. Koopmans et al. [76] succeeded to show, that, if the same mechanism of spin reversal in electron-phonon collisions is responsible for subpicosecond demagnetization as well as for the Gilbert damping of the subnanosecond macrospin oscillations, the demagnetization time τ_M and the damping constant α are connected via

$$\tau_M \approx c_0 \frac{\hbar}{k_B T_C} \frac{1}{\alpha} \ , \tag{2.18}$$

where $c_0 = 1/8$ for Ni, k_B denotes the Boltzmann constant and T_C the Curie temperature. Soon after this hyphothesis was published, two groups [88, 89] attempted to test it in rare-earth (Gd, Tb, Dy, Ho) and transition metal (Pd) doped $Ni_{80}Fe_{20}$ samples. The doping significantly increased the Gilbert damping compared with pure $Ni_{80}Fe_{20}$ films as measured with time-resolved MOKE [88] and FMR [89], whereas T_C was not affected. Consequently, Eq. 2.18 predicts a faster demagnetization time with increasing dopant concentration. However, the measured τ_M either did not depend on the dopant concentration or even increased with higher concentration of Tb, Dy and Ho. J. Walowski et al. [88] noted, that for efficient spin-flip scattering, band-mixing of spin-up and spin-down bands is necessary and conjectured, that this condition is not fulfilled in Dy doped samples. On the other hand, I. Radu et al. [89] observed a systematic slowing down of the de- and remagnetization time with increasing Tb, Dy and Ho concentration and proposed a 'slow relaxing impurity model' to explain their findings. This model is based on, first, the anisotropic exchange coupling of the rare earth 4f magnetic moments to the 3d magnetic moment of Fe and Ni and, second, on the thermal population of the exchange split 4f states. Once the 3d magnetic moment changes, the anisotropy of the 4f-3d exchange interaction causes a modulation of the 4f exchange splitting. The thermal population of the 4f levels does not follow these changes instantaneously, but rather delayed by the rare-earth spin-lattice relaxation time.
In a recent publication, B. Koopmans et al. [74] derived an analytical equation for magnetization dynamics $m(t)$ on the basis of the aforementioned assumptions. $m(t)$ is coupled to the Two-Temperature Model (Eq. 2.8,2.9) via T_e and T_p and reads

$$\frac{dm(t)}{dt} = R \cdot m(t) \frac{T_p(t)}{T_C} \left(1 - m(t) \coth \left(\frac{m(t) T_C}{T_e(t)} \right) \right) \ , \tag{2.19}$$

with $m = M/M(T = 0\ \mathrm{K})$. The demagnetization rate $R \sim \alpha_{EY} T_C^2/\mu_{at}$ depends on the Elliot-Yafet spin-flip probability α_{EY}, Curie temperature T_C and the atomic magnetic moment μ_{at}. It has to be noted, that, recently, U. Atxitia and O. Chubykalo-Fesenko [73] showed, that Eq. 2.19 is a special case of Landau-Lifshitz-Bloch equation for $S = 1/2$, $\lambda_{LLB} = \lambda_{0,LLB} \cdot T_p/T_e$ without the precessional term. B. Koopmans et al. [74] distinguish between the two limits, $R \cdot \tau_E >> 1$ (type I dynamics) and $R \cdot \tau_E << 1$ (type II dynamics), where τ_E is the electron-phonon equilibration time. Type I dynamics shows up as one step, fast demagnetization process, as observed e.g. in Ni and Co, and type II dynamics is associated with a fast demagnetization at the beginning followed by a second slow demagnetization, as measured e.g. in Gd. Thus, the model succeeds in describing both dynamics with an appropriate set of parameters. Depending on the fluence of the pump pulse and the initial sample temperature, a transition from type I to type II dynamics is possible. Furthermore, the authors obtained $\alpha_{EY} = p\langle b^2 \rangle$ for Ni, Co and Gd from fitting the experimental data and compared it with *ab initio* calculations of the spin-mixing parameter $\langle b^2 \rangle$ [90]. For reasonable values of the material-dependent parameter p, *ab initio* calculations compared well with measured data. In other words, to explain the femtosecond laser-induced demagnetization of Ni by spin-flip electron-phonon collisions, the model of B. Koopmans et al. [74] requires $\alpha_{EY} \sim 0.1$, which is supported by *ab initio* calculations from D. Steiauf and M. Fähnle [90]. An other *ab initio* work by K. Carva et al. [91] confirmed the results of [90] for Ni in the Elliott approximation [92]. In addition, the authors calculated the spin-flip probability by a more general approach yielding somewhat smaller values. More important, they noted, that a large demagnetization is not necessarily a consequence of a large spin-flip probability, but rather a difference between the transition rates of spin-up to spin-down compared to spin-down to spin-up scattering. They found the difference to be negligible for low electronic temperature T_e, but higher for thermalized electrons with T_e of several thousands of K and significantly higher for a non-equilibrium electron distribution. A rough estimate of demagnetization per Ni atom is given by about 0.1 μ_B/200 fs.

In addition to the above-described phonon-assisted demagnetization, other collective excitations, magnons, are considered to play an important role in femtosecond spin dynamics of ferromagnets. In time-, energy- and spin-resolved Two-Photon-Photoemission studies on Co films, M. Cinchetti et al. [93] observed time-dependent oscillations in the spin-polarization for $E - E_F = 0.4$ eV. They attributed a transient increase in the normalized spin- polarization about 120 fs after the laser excitation to magnon creation in the spin-flip electron-magnon collisions of minority electrons. Thus, this process leads to a transient

increase of the net magnetization and cannot explain demagnetization. On the other hand, E. Carpene et al. [94] performed time- and probe-photon energy-dependent reflectivity and L-MOKE studies on Fe films and found slower electron-phonon thermalization time $\tau_{ep} = (240\pm10)$ fs than the fluence-dependent demagnetization times $\tau_M = 50-75$ fs. They proposed, that the conservation of angular momentum is fulfilled due to the creation of magnons and estimated the electron-magnon equilibration time on the basis of a theory for electron-phonon relaxation [95], replacing the phonon by the magnon dispersion relation. Indeed, in a time-, energy-, momentum- and spin-resolved Two-Photon-Photoemission experiment on Fe films combined with *ab initio* many-body calculations, A. B. Schmidt et al. [96] showed, that magnons can be excited on the timescale of few femtoseconds. Therefore, it is necessary to further explore the connection between ultrafast demagnetization and magnon creation in specially designed experiments as well as in devoted theories.

Superdiffusive Spin Transport

The previous section described local interactions between charge carriers, spins, phonons and magnons after femtosecond laser excitation. However, hot electrons in metals with energy E above the Fermi level and spin σ move through the sample with a velocity $v(E,\sigma)$ and lifetime $\tau(E,\sigma)$, until they decay to lower energy levels via electron-electron and electron-phonon collisions. It has to be noted, that, due to the strong dielectric screening in metals [43], the time-averaged, net charge flow is zero. The dielectric screening is incorporated into theories of femtosecond laser-induced, non-equilibrium electron dynamics in noble metals, e.g. by N. Del Fatti et al. [97] (see also references therein).
Model systems to study excited charge carrier transport on the femtosecond timescale are metals having exclusively sp-bands above E_F, like Au and Cu, with high velocities and lifetimes [38, 98]. S. D. Brorson et al. [99] measured the transient reflectivity of Au films on sapphire by optical pumping from the front side and probing from the backside through the transparent substrate in a time-of-flight approach. They detected the arrival of hot electrons, the delay time of which increased linearly with the film thickness. Similarly, J. Hohlfeld et al. [62] observed thickness-dependent transport effects in transient reflectivity measurements on Au films. Moreover, R. Knorren et al. [38] included charge carrier transport in their model to adequately describe results from time- and spin-resolved Two-Photon-Photoemission (2PPE) from Cu and the transition metal ferromagnets Fe, Co and Ni. The time-of-flight experiment from [99] was extended to measure spin transport by A. Melnikov et al. [100], who optically excited spins in a layer of Fe, which subse-

quently traveled through a layer of Au and were detected on the Au surface by means of magnetization-induced, second harmonic generation.

It is known, e.g. from 2PPE measurements [38] and *ab initio* GW+T calculations [101], that the lifetimes and velocities for hot electrons in Fe, Co and Ni are spin-dependent. In particular, the lifetime-velocity-product is usually higher for majority than for minority electrons [101]. In 2010, M. Battiato et al. [41, 102] proposed the superdiffusive spin transport model to explore the role of spin-dependent transport effects for the laser-induced demagnetization.

The main assumptions of the model can be summarized as follows.

1. Electrons are excited by photons or other electrons to states above E_F. The spin-dependent electronic structure of the material is taken into account. The dynamics of the excited holes is not considered due to their low velocities.

2. The excited electron moves in a random direction in a straight trajectory with velocity $v(E, \sigma, z)$ (the z coordinate is perpendicular to the film surface) until, with a probability of $1/\tau(E, \sigma, z)$ per unit time, it collides with a phonon, impurity or other electron. Before the first collision, the electrons are named first generation electrons, before the second collision, second generation electrons, etc.. The z-dependence of the velocity becomes important for inhomogeneous films and multilayers.

3. The electrons scatter elastically on phonons and impurities, but inelastically on other electrons. The inelastic scattering is treated in a classical two-particles collision theory. The electron momentum after scattering is assumed to be not correlated to the momentum before scattering.

The input parameters for the model are the excitation rate of the first generation electrons by photons and the ratio of excited majority to minority electrons as well as the energy- and spin-dependent electron lifetimes $\tau(\sigma, E)$ and velocities $v(\sigma, E)$. All parameters are taken from *ab initio* calculations [81, 101, 103] apart from the extrapolation of the lifetimes and velocities to $E = E_F$.

The starting point is the electron flux $\phi(z, t; z_0, t_0)$ in (z, t) caused by an electron generated at position z_0 at the time t_0:

$$\phi(z,t;z_0,t_0) = \frac{\left[\widetilde{\Delta t}\right]}{2\,(t-t_0)^2} \exp\left(-(t-t_0)\left[\frac{\widetilde{\Delta t}}{\tau}\right]\frac{1}{[\widetilde{\Delta t}]}\right)\Theta((t-t_0)-|[\widetilde{\Delta t}]|)\;, \tag{2.20}$$

where

$$\left[\frac{\widetilde{\Delta t}}{\tau}\right](z;z_0) = \int_{z_0}^{z} dz'/(\tau(z')v(z')) \tag{2.21}$$

and

$$\left[\widetilde{\Delta t}\right](z;z_0) = \int_{z_0}^{z} dz'/v(z') \ . \tag{2.22}$$

Here, $\Theta((t-t_0)-|[\widetilde{\Delta t}]|)$ is the unit step function. The lifetime τ and velocity v are material-dependent parameters, and are therefore dependent on the z position for a multilayer structure. Replacing the single electron by a distribution of laser-excited electrons $S^{ext}(\sigma,E,z,t)$, the resulting electron flux can be written as

$$\Phi(z,t) = \int_{-\infty}^{+\infty} dz_0 \int_{-\infty}^{t} dt_0 \ S^{ext}(z_0,t_0)\phi(z,t;z_0,t_0) \ . \tag{2.23}$$

Now, the first generation electron distribution $n^{[1]}(\sigma,E,z,t)$ can be calculated by solving the continuity equation

$$\frac{\partial n^{[1]}}{\partial t} + \frac{n^{[1]}}{\tau} = -\frac{\partial \Phi}{\partial z} + S^{ext}. \tag{2.24}$$

Replacing the source term S^{ext} by

$$S^{[2]}(\sigma,E,z,t) = \sum_{\sigma'} \int_{0}^{\infty} p(\sigma,\sigma',E,E',z)\frac{n^{[1]}(\sigma',E',z,t)}{\tau(\sigma',E',z)}dE' \tag{2.25}$$

in Eq. 2.23 and 2.24, it is possible to calculate the distribution of the second generation electrons $n^{[2]}$. The elastic and inelastic scattering contributions and generation of cascade electrons from the initial distribution $n^{[1]}$ are taken into account by the transition probability $p(\sigma,\sigma',E,E',z)$. For inelastic electron-electron scattering, the maximum energy transfer is treated within classical physics of collisions. Although spin-flip scattering can be included in p, it is assumed to be negligible.
By subsequent solving Eq. 2.24 with the correct source term, the electron distribution $n(\sigma,E,z,t) = \sum_{i=1}^{\infty} n^{[i]}$ can be derived. Given, that every majority (minority) electron carries a magnetic moment of μ_B ($-\mu_B$), the magnetization reads

$$M(E,z,t) = \mu_B \left[n(\uparrow,E,z,t) - n(\downarrow,E,z,t)\right] \ . \tag{2.26}$$

For comparison with time-resolved, magneto-optical reflectivity (P-, L-, T-MOKE) or transmission (Faraday effect, MCD) measurements, the spatial averaging is accomplished by

$$\frac{Q(t)-Q(t<0)}{Q(t<0)} = \frac{\int_0^d dz \ M(z,t)\exp\left(-z/\lambda_{opt}\right)}{\int_0^d dz \ M(z,t<0)\exp\left(-z/\lambda_{opt}\right)} - 1 \ , \tag{2.27}$$

where Q denotes the magneto-optical quantity of interest, d is the film thickness and λ_{opt} the optical penetration depth of the probe light.
Lastly, superdiffusion can be classified as a mode of transport in between the diffusive and ballistic transport, which, in addition, incorporates the electron thermalization. Conveniently, the variance of the displacement of the particle distribution $\sigma^2(t) \sim t^{\gamma_{tr}}$ is used to classify the mode of transport. For $\gamma_{tr} = 1$ the transport is diffusive, whereas for $\gamma_{tr} = 2$ it is ballistic. However, in the case of the superdiffusive spin transport $\gamma_{tr} = \gamma_{tr}(t)$ starting in the ballistic regime with a continuous transition to the diffusive regime.

3. Experimental Background

3.1. Non-Resonant and Resonant Magneto-Optical Effects

This chapter will review the fundamentals of resonant as well as non-resonant magneto-optical effects with a special focus on the transversal magneto-optical Kerr effect (T-MOKE) being applied in this work. We call 'resonant magneto-optics' all the effects, where transitions between the atomic core levels and valence bands with the highest unoccupied density of states are involved, whereas the transitions within the bands close to the Fermi energy are referred to as 'non-resonant magneto-optics'. We start with the classical electrodynamics and the Lorentz-Drude model of the dielectric tensor and continue with the quantum-mechanical models, which show the importance of the spin-orbit splitting and spin-polarization for magneto-optical effects. Subsequently, magneto-optics at the core level absorption edges of the 3d ferromagnets Fe, Co and Ni will be discussed and some important experiments will be reviewed. Moreover, we will show the close relation between MOKE and resonant magnetic scattering. This work is about magneto-optics of stacked ferromagnetic and non-magnetic layers and therefore, the magneto-optical simulation of (multi)layers will be discussed at the end of this chapter.

We start with the classical continuum electrodynamics to derive the transversal magneto-optical Kerr effect (T-MOKE). From the Maxwell equations [104], the wave equation for the electric field $\boldsymbol{E}$,

$$\boldsymbol{k}(\boldsymbol{k}\cdot\boldsymbol{E}) - \boldsymbol{k}^2\boldsymbol{E} + \frac{\omega^2}{\epsilon_0 c^2}\underline{\boldsymbol{\epsilon}}\,\boldsymbol{E} = \boldsymbol{0}\ , \tag{3.1}$$

can be deduced. Here, $\boldsymbol{k}$ denotes the wave vector, ω the angular frequency, ϵ_0 the permittivity of free space, c the vacuum velocity of light and

$$\underline{\boldsymbol{\epsilon}} = \epsilon_0 \cdot \begin{pmatrix} \epsilon_{xx} & \epsilon_{xy} & 0 \\ -\epsilon_{xy} & \epsilon_{xx} & 0 \\ 0 & 0 & \epsilon_{zz} \end{pmatrix} \tag{3.2}$$

is the dielectric tensor, the specific structure of which can be understood from the classical oscillator model (Lorentz-Drude model [105], see below). Note, that Eq. 3.1 is only valid

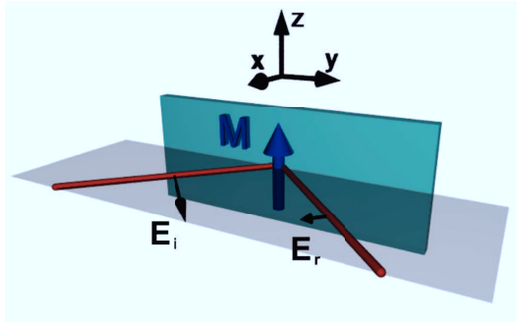

Figure 3.1.: Transversal MOKE geometry. The magnetization $\boldsymbol{M}$, located simultaneously perpendicular to the incidence plane of light and in the sample's plane, changes the amplitude and phase of the p-polarized electric field. E_i denotes the incident and E_r the reflected electric field.

for wavelengths much larger than the lattice constant, which is not the case for X-rays, where scattering has to be treated on the atomic level [106]. For the chosen coordinate system, the magnetic field $\boldsymbol{H}$ and the magnetization $\boldsymbol{M}$ point into the z-direction (Fig. 3.1). For the wave vector being perpendicular to $\boldsymbol{H}$, the solution of Eq. 3.1 consists of two orthogonal modes with perpendicular (p) and parallel (s) polarization with respect to $\boldsymbol{H}$. The resulting refractive indices are $n_s = \sqrt{\epsilon_{zz}}$ and $n_p = \sqrt{\epsilon_{xx} + \epsilon_{xy}^2/\epsilon_{xx}}$. In the Lorentz-Drude model, it can be shown, that only ϵ_{xy} depends on the magnetization [105] and therefore, T-MOKE is only observed for p-polarized light.
In the next step, the Fresnel reflection coefficient r_{pp} can be determined, applying the continuity condition for the electric field $\boldsymbol{E}$ and the electric displacement field $\boldsymbol{D}$ at the sample-vacuum interface. Given, θ is the angle of incidence with respect to the sample's normal and $\boldsymbol{M}^{\pm}$ the magnetization either oriented in the $+z$- or $-z$-direction, the reflection coefficient reads [105]

$$r_{pp}(\boldsymbol{M}^{\pm}) = \frac{n_p^2 \cos\theta - \sqrt{n_p^2 - \sin^2\theta} \pm \epsilon_{xy}/\epsilon_{xx} \cdot \sin\theta}{n_p^2 \cos\theta + \sqrt{n_p^2 - \sin^2\theta} \pm \epsilon_{xy}/\epsilon_{xx} \cdot \sin\theta} \,. \tag{3.3}$$

Expanding r_{pp} in the first order of $\epsilon_{xy}/\epsilon_{xx}$ yields [107, 108]

$$r_{pp}(\boldsymbol{M}^{\pm}) \approx \frac{\epsilon_{xx}\cos\theta - \sqrt{\epsilon_{xx} - \sin^2\theta}}{\epsilon_{xx}\cos\theta + \sqrt{\epsilon_{xx} - \sin^2\theta}} \left(1 \pm \frac{\sin 2\theta}{\epsilon_{xx}^2 \cdot \cos^2\theta - \epsilon_{xx} + \sin^2\theta} \cdot \epsilon_{xy}\right) \tag{3.4}$$

or

$$r_{pp}(\boldsymbol{M}^{\pm}) \approx X(\epsilon_{xx},\theta)(1 \pm Y(\epsilon_{xx},\theta)\cdot\epsilon_{xy}) \tag{3.5}$$

$$X(\epsilon_{xx},\theta) = \frac{\epsilon_{xx}\cos\theta - \sqrt{\epsilon_{xx}-\sin^2\theta}}{\epsilon_{xx}\cos\theta + \sqrt{\epsilon_{xx}-\sin^2\theta}} \tag{3.6}$$

$$Y(\epsilon_{xx},\theta) = \frac{\sin 2\theta}{\epsilon_{xx}^2\cdot\cos^2\theta - \epsilon_{xx} + \sin^2\theta}\ , \tag{3.7}$$

where $X(\epsilon_{xx},\theta)$ and $Y(\epsilon_{xx},\theta)$ are the non-magnetic contributions, which depend on θ as well as ϵ_{xx} and thus the photon energy.
Note, that ϵ_{xx}, ϵ_{xy} and $r_{pp}(\boldsymbol{M}^{\pm})$ are complex numbers.
Conveniently, the magnetic asymmetry

$$A = \frac{1}{2}\frac{|r_{pp}(\boldsymbol{M}^{+})|^2 - |r_{pp}(\boldsymbol{M}^{-})|^2}{|r_{pp}(\boldsymbol{M}^{+})|^2 + |r_{pp}(\boldsymbol{M}^{-})|^2} = \frac{2\ \Re(Y(\epsilon_{xx},\theta)\cdot\epsilon_{xy})}{1+|Y(\epsilon_{xx},\theta)\cdot\epsilon_{xy}|^2} \approx 2\ \Re(Y(\epsilon_{xx},\theta)\cdot\epsilon_{xy}) \tag{3.8}$$

is measured in the experiments. By scanning the photon energy and the angle of incidence, it is possible to derive $\epsilon_{xx}(\hbar\omega)$ and $\epsilon_{xy}(\hbar\omega)$ from measurements [105].
The two other, in the visible spectral range even more frequently applied MOKE geometries, are the longitudinal (Fig. 3.2) and polar MOKE (Fig. 3.3). In general, the reflected

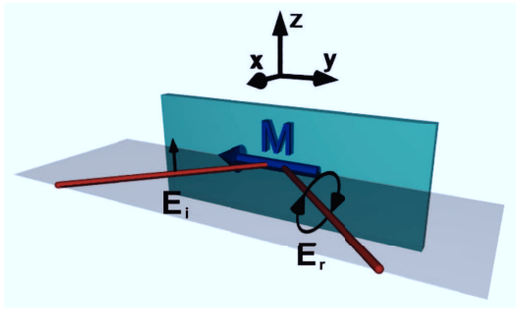

Figure 3.2.: Longitudinal MOKE geometry. The magnetization $\boldsymbol{M}$, located simultaneously in the incidence plane of light and the sample's plane, turns the polarization direction of the incident, linearly polarized light and induces an elliptical polarization. E_i denotes the incident and E_r the reflected electric field.

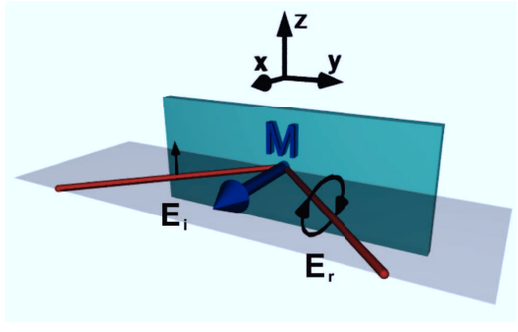

Figure 3.3.: Polar MOKE geometry. The magnetization $\boldsymbol{M}$, located simultaneously in the incidence plane of light and perpendicular to the sample's plane, turns the polarization direction of the incident, linearly polarized light and induces an elliptical polarization. E_i denotes the incident and E_r the reflected electric field.

electric field vector $\boldsymbol{E_r}$ is connected to the incident linearly polarized electric field vector $\boldsymbol{E_i}$ via

$$\boldsymbol{E_r} = \underline{\boldsymbol{R}}\boldsymbol{E_i} \ , \tag{3.9}$$

and the reflection matrix reads

$$\underline{\boldsymbol{R}} = \begin{pmatrix} r_{ss} & r_{sp} \\ r_{sp} & r_{pp} \end{pmatrix} \ . \tag{3.10}$$

Due to the non-diagonal matrix element r_{sp}, which is zero for T-MOKE, the polarization state of the initially linearly polarized electric field is changed according to

$$\tan\left(\theta_K + i \cdot \varepsilon_K\right) = \frac{r_{sp}}{r_{pp,ss}} \ , \tag{3.11}$$

where θ_K denotes the rotation of the main polarization axis and ε_K the phase shift or the ellipticity. Thus, the reflected light is elliptically polarized and its polarization axis is rotated.
In analogy to P-MOKE, the likewise effect with linearly polarized light in transmission geometry is called Faraday effect. The magnetization-induced intensity modulation, as observed in the T-MOKE geometry with linearly p-polarized light, is also present for circulary polarized light in the Faraday geometry (Fig. 3.4) and is referred to as magnetic

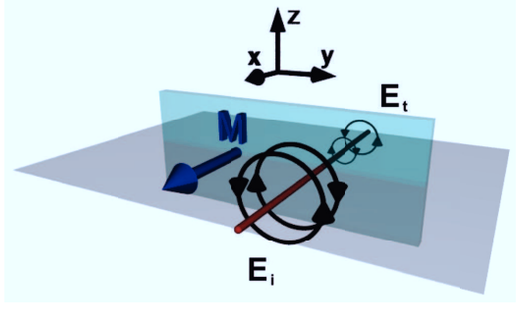

Figure 3.4.: MCD geometry. The transmission of the circularly polarized light depends on the direction of the magnetization $\boldsymbol{M}$ or, alternatively, on the helicity of light indicated by the two circles. E_i denotes the incident and E_t the transmitted electric field.

circular dichroism (MCD). Given one fixed light helicity, the sample thickness d, the transmission coefficient T and magnetization $\boldsymbol{M}$ oriented either in $+x$- or in $-x$-direction, the MCD asymmetry reads

$$A = \frac{T(\boldsymbol{M}^+) - T(\boldsymbol{M}^-)}{T(\boldsymbol{M}^+) + T(\boldsymbol{M}^-)} \approx 2\frac{\omega d}{c}\Re\left(\frac{\epsilon_{xy}}{\sqrt{\epsilon_{xx}}}\right) . \tag{3.12}$$

Like all the hitherto discussed magneto-optical effects, MCD is, in first approximation, linear in ϵ_{xy} and thus the magnetization. Furthermore, it has to be noted, that keeping the magnetization fixed and reversing the helicity of light produces the same MCD asymmetry.

In a simple, classical oscillator model, the so-called Lorentz-Drude model [105], it is possible to derive expressions for $\epsilon_{xx}(\omega)$ and $\epsilon_{xy}(\omega)$, which exhibit a resonant behaviour with respect to the oscillation frequency. The starting point is the equation of electron motion in the presence of the electric field $\boldsymbol{E}$ of light and static magnetic field $\boldsymbol{B}$. If $\boldsymbol{B}$ is oriented in the z-direction, the Lorentz force $\boldsymbol{F_L} = e \cdot \boldsymbol{dx}/dt \times \boldsymbol{B}$ will act in the x-y-plane and the electron will perform a rotational motion about the z-axis. In this sense, the dielectric tensor, which represents the electron response to the electric field of light, rotates the electric field vector $\boldsymbol{E}$ about the z-axis.

Moreover, for $\omega_L << \omega$ and for the linear approximation in ω_L, the Lorentz-Drude model predicts ϵ_{xy} to be highest at the inflexion points of the resonance peak, which reads

$$\epsilon_{xy} = i\omega_L \frac{d\epsilon_{zz}}{d\omega} \ , \tag{3.13}$$

with $\omega_L = e|\boldsymbol{B}|/(2m)$ being the Larmor frequency, e and m the electron charge and mass. For ferromagnets, the approximation is valid for photon energies in the visible spectral range and higher, since $\hbar\omega_L$ is in the range of 10 to 100 meV for magnetic fields inside a ferromagnet (Weiss fields).

Although the Lorentz-Drude model provides some basic understanding of magneto-optical effects, the correct microscopic description can be only given in the quantum mechanical picture. It has been known since 1932 [109, 110], that the spin-orbit interaction is essential for magneto-optical effects. P. N. Argyres estimated the order of magnitude of the Faraday and polar Kerr effect for Fe and Ni from first principles in 1955 [111]. He included the spin-orbit interaction in the Hamiltonian and, using perturbation theory, derived expressions for the optical conductivity and polarizability in the first order of the spin-orbit energy. Despite the crude estimation of the transition matrix elements, he achieved an order of magnitude agreement between the theory and experiment. It has to be noted, that a net magnetization is needed for a non-zero Kerr effect. In the approximation of [111], the Faraday and polar Kerr effects are both linear in the magnetization.

In the following paragraph, the fundamentals for *ab initio* calculations of the optical conductivity will be presented. In short, the optical conductivity tensor $\underline{\boldsymbol{\sigma}}(\omega)$ is related to the dielectric tensor $\underline{\boldsymbol{\epsilon}}(\omega)$ via

$$\underline{\boldsymbol{\sigma}}(\omega) = \frac{\omega}{4\pi i} \left(\underline{\boldsymbol{\epsilon}}(\omega) - 1\right) \ . \tag{3.14}$$

There are two contributions to the elements of $\underline{\boldsymbol{\sigma}}(\omega)$, which arise from the intraband and interband transitions. The intraband contribution can be described by a phenomenological Drude model [112]

$$\sigma_{intra}(\omega) = i\sigma_0\delta_D/(\omega + i\delta_D) \ , \tag{3.15}$$

with σ_0 being the DC conductivity and δ_D the inverse of the phenomenological relaxation time. The interband conductivity, on the other hand, can be calculated from first principles

[113], for instance using the expression derived by C. S. Wang and J. Callaway [114] from linear response theory

$$\sigma_{xx}(\omega) = \frac{ie^2}{m^2\hbar}\sum_{\boldsymbol{k}}\sum_{l,occ.}\sum_{n,unocc.}\frac{1}{\omega_{nl}(\boldsymbol{k})}\left(\frac{|\Pi^x_{ln}|^2}{\omega-\omega_{nl}(\boldsymbol{k})+i\delta}+\frac{|\Pi^x_{ln}|^2}{\omega+\omega_{nl}(\boldsymbol{k})+i\delta}\right) \tag{3.16}$$

$$\sigma_{xy}(\omega) = \frac{ie^2}{m^2\hbar}\sum_{\boldsymbol{k}}\sum_{l,occ.}\sum_{n,unocc.}\frac{1}{\omega_{nl}(\boldsymbol{k})}\left(\frac{\Pi^x_{ln}\Pi^y_{nl}}{\omega-\omega_{nl}(\boldsymbol{k})+i\delta}+\frac{(\Pi^x_{ln}\Pi^y_{nl})^*}{\omega+\omega_{nl}(\boldsymbol{k})+i\delta}\right) . \tag{3.17}$$

The summation has to be done over the Brillouin zone, the occupied states with the index l as well as the unoccupied states with the index n. Furthermore, $\hbar\omega_{nl}(\boldsymbol{k}) = E_n(\boldsymbol{k}) - E_l(\boldsymbol{k})$ is the energy difference of the optical transition between l and n and δ is the inverse of the phenomenological relaxation time, which accounts for finite lifetimes of the excited states. The transition matrix elements $\Pi^{x,y}_{nl}$ of the momentum operator $\boldsymbol{p}$ are defined by

$$\boldsymbol{\Pi}_{nl}(\boldsymbol{k}) = \int \psi^*_{n,\boldsymbol{k}}(\boldsymbol{r})\ \boldsymbol{p}\ \psi_{l,\boldsymbol{k}}(\boldsymbol{r})\ d\boldsymbol{r}\ , \tag{3.18}$$

with $\psi_{n,\boldsymbol{k}}$ being the Bloch electron wave functions.

The described formalism was employed by P. M. Oppeneer et al. in 1992 [113] to calculate the polar Kerr rotation for the valence bands of Fe, Co and Ni. In this work, only the intraband conductivity and the parameter δ were not derived from *ab initio* calculations. For Fe, the agreement between the theory and experiment is excellent, whereas for Ni and Co, it is still quite good. In addition, P. M. Oppeneer et al. exemplified on Ni, that Kerr rotation scales linearly with the spin-orbit coupling strength, but the dependence on the exchange splitting appears to be more complicated.

Magneto-optical effects are certainly not only limited to the visible spectral range and therefore, they have been predicted [115] and observed at the 3p core levels of Fe, Co and Ni [32–36, 116–121]. After the discovery, that magneto-optical sum rules can be applied to X-Ray Magnetic Circular Dichroism (XMCD) spectra to separate and determine the spin and orbital magnetic moments [122], many studies have been performed at the 2p absorption edges of Fe, Co and Ni [22], where the $2p_{1/2}$ and $2p_{3/2}$ core levels are well separated. But also other magneto-optical effects like T-MOKE and Faraday effect have been studied at the 2p [123–127] and even 1s [128, 129] core levels of transition metal ferromagnets. In particular, at the 1s core levels, the wavelength of the X-Rays becomes smaller than the lattice constant and Bragg peaks from atomic scattering are detected. In this case, the wave equation (Eq. 3.1), derived from the macroscopic Maxwell equations, is not valid any more and magneto-optical effects are treated in a scattering theory [106]. Since the spin-orbit (SO) splitting is necessary for the existence of magneto-optical effects,

it is not surprising, that due to the SO splitting of the 3p and even larger SO splitting of the 2p core levels, magneto-optical effects are significantly enhanced compared to the transitions between the valence bands. In particular, J. L. Erskine and E. A. Stern predicted in 1975 [115] a large magneto-optical absorption at the Ni 3p states, which can be attributed to the joined effect of the final state spin-polarization and large initial state spin-orbit coupling.

Surprisingly, the first experimental evidence for resonant magnetic scattering in the T-MOKE geometry was found at the Ni 1s absorption edge [128, 129] with no spin-orbit splitting. Similar to that, the first XMCD data were obtained at the Fe 1s absorption edge [131]. Furthermore, the allowed dipole transitions are to the 3p valence states with much less spin-polarization than the 3d states. According to that, the magnetic asymmetry reached 10^{-3} at most [128], which is two to three orders of magnitude lower than at the 2p and 3p absorption edges. The experimental findings were explained by superposition of resonant and non-resonant magnetic scattering. The magnetic asymmetry for elastic resonant magnetic scattering in the T-MOKE geometry (Fig. 3.1) can be derived from scattering theory [106] and reads

$$A(E,\theta) = \frac{3}{2\pi}\frac{\hbar c}{r_e}\frac{\tan(2\theta)}{E}\frac{F_m^z}{|F_c|^2}\left[F_c^{'}\Im(F_{-1}^1 - F_{+1}^1) - F_c^{''}\Re(F_{-1}^1 - F_{+1}^1)\right] , \tag{3.19}$$

with r_e being the classical electron radius, E the photon energy, θ the angle of incidence, F_m^z the z-component of the resonant magnetic structure factor, $F_c = F_c^{'} + iF_c^{''}$ the charge structure factor and $F_{\pm 1}^1(E)$ the dipole transition strength. Eq. 3.19 can be considered as the quantum-mechanical analogon to Eq. 3.8. Interestingly, if θ approaches the Brewster angle of about 45°, the magnetic asymmetry in Eq. 3.19 increases rapidly as observed in experiments.

At the 2p absorption edges of Fe, Co and Ni, the condition for the wavelength to be smaller than the lattice constant doesn't hold any more and therefore, no Bragg peaks are observed. Nevertheless, the magnetic asymmetry can be measured in specular reflection from a smooth surface, as it was accomplished by C. Kao et al. in 1990 [123] for an Fe thin film. The progress in X-ray optics enabled magneto-optical polarization spectroscopy in the soft X-ray region and the determination of $\epsilon_{xx}(E)$ and $\epsilon_{xy}(E)$ for Fe, Co and Ni at their respective 2p absorption edges [124–127].

In parallel, the research at the 3p absorption edges started in the 1990s. Among the first groups, T. Koide et al. [32] measured XMCD spectra at the 3p edges of Ni, which could be reproduced by calculations [132].

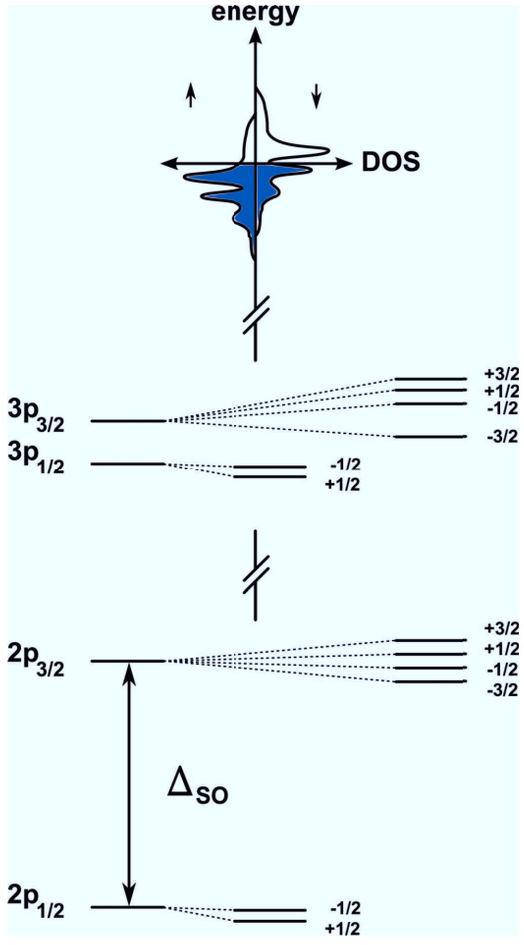

Figure 3.5.: Schematic view of spin-resolved valence bands as well as spin-orbit and exchange split 2p and 3p core levels of a 3d ferromagnet (after [22] and [130]). At the 2p core levels, the spin-orbit splitting energy Δ_{SO} is one order of magnitude larger than the exchange splitting, whereas at the 3p core levels, they have the same magnitude.

F. U. Hillebrecht at al. [117] showed dichroism effects with linearly p-polarized light in Co and Fe thin films, both in absorption (photocurrent) and reflection (T-MOKE), and employed the dichroism effects for domain imaging of Fe(100) single crystals using photoelectron microscopy.

In contrast to the 2p absorption edges, where the spin-orbit coupling for Ni is about 17 eV, at the 3p edges, it is a factor of ten smaller and therefore, it is comparable to the core level exchange splitting being present in ferromagnets (Fig. 3.5). Consequently, *ab initio* calculations of optical conductivity at the 3p absorption edges are challenging, because neither the spin-orbit nor the exchange splitting can be treated as a perturbation.

Coming back to the brief historical review, systematic studies of photon energy and angular dependence of T-MOKE [33, 34] as well as element-specific, magneto-optical hysteresis loops [120] followed later on. In the Ph.D. thesis of M. Pretorius from 1999 [105], $\epsilon_{xx}(E)$ and $\epsilon_{xy}(E)$ for Fe, Co and Ni at the 3p absorption edges are derived from T-MOKE measurements. On the other hand, S. Valencia et al. [35] obtained the diagonal as well as the non-diagonal components of the dielectric tensor for the same elements from the Faraday effect. These $\epsilon_{xx}(E)$ and $\epsilon_{xy}(E)$ from Ref. [35] have been used in this work for magneto-optical simulations of Ni/Ru/Fe layers (Chapter 4.1.1).

It is interesting to note, that, recently, the same group discovered a magneto-optical effect being quadratic in the magnetization [133] (in contrast to T-MOKE being linear in magnetization), which analogue in the visible spectral range is referred to as Schäfer-Hubert effect. Moreover, in the same work, the computational problems due to the before mentioned comparable size of the spin-orbit and exchange splitting were solved. *Ab initio* calculations of the magneto-optical spectrum show, that hybridization between the 3p states has to be taken into account [133].

T-MOKE studies have not only been carried out on single layers, but also on interlayer exchange coupled Co/Si/Ni/Fe- and $Ni_{80}Fe_{20}$/Cr/$Co_{40}Fe_{60}$ layers by P. Grychtol et al. [36, 121, 134], where layer-selective magnetization rotation and magneto-optical crosstalk have been observed. Moreover, R. Adam et al. [135] performed time- and layer-resolved measurements of magnetization precession in $Ni_{80}Fe_{20}$/MgO/Co layers.

At the end of this chapter, the simulation of MOKE in magnetic layers will be briefly discussed. S. Višňovský [136] extended P. Yeh's formalism for optical simulations of layered structures [137] to absorbing, anisotropic, magnetic layers. This approach is based on the solution of Eq. 3.1, incorporating the boundary conditions for the electric and magnetic fields at every interface. The derived formalism was adopted by M. Buchmeier, who wrote a program, which, in particular, requires the values of $\epsilon_{xx}(E)$ and $\epsilon_{xy}(E)$ as input parameters

[138]. This program was used to calculate the magnetic asymmetry for Ni/Ru/Fe layers at the 3p absorption edges with $\epsilon_{xx}(E)$ and $\epsilon_{xy}(E)$ from [35] (Chapter 4.1.1). In general, for small enough wavelengths, the scattering from the rough surface has to be considered too [105], but for the wavelengths ($>$ 17 nm) and samples used in this work, this effect was neglected.

3.2. Laser High Harmonics in Noble Gases

The process of laser harmonic generation from crystals in the visible spectral range (e.g. second harmonic and third harmonic generation), being discovered in 1961 by P. A. Franken et al. [139], is well-known and broadly used in laser technology. Contrary to that, the field of laser- generated high harmonics in the gas phase, which nowadays can reach photon energies as high as 1.6 keV [31], is much younger. In the second half of 1980s, several groups observed a plateau of odd high harmonics of the laser frequency generated in noble gases with a distinct cut-off energy [25, 26]. Furthermore, the spatial [140] and temporal [141] coherence of the high harmonics radiation was demonstrated. A feature, that was not immediately understood, was a constant intensity of the harmonics in a broad spectral range, which cannot be explained in a perturbation theory of non-linear optics. The latter predicts an exponential intensity decrease with increasing order of high harmonics [142].

The laser intensities required for high harmonic generation are typically in the order of $10^{14} - 10^{15}$ W/cm^2 with corresponding electric fields of $10^{10} - 10^{11}$ V/m (for comparison, the electric fields generated in a flash of lightning are about 10^4 V/m [143]), which compare to or even exceed the intra-atomic electric fields. Consequently, the potential of the laser electric field, which is superimposed on the Coulomb barrier, can reduce the overall potential within a certain time. The initially bound electron can tunnel from the highest energy level through the potential into the continuum states 3.6. This process is called tunnel ionization and is important for high harmonic generation. On the other hand, if the electric field does not reduce the Coulomb barrier, the ionization can occur through multiphoton absorption.

Once the atom is ionized by an electric field $E(t) = E_0 \cos(\omega t + \phi)$ at any arbitrary phase ϕ, the strength of the Coulomb potential at the electron position is strongly reduced, and thus, the motion of the electron wave packet can be classically described by Newton's equation of motion [142, 144]

$$m\frac{d^2x(t)}{dt^2} = -eE(t) \ , \tag{3.20}$$

with the general solution

$$x(t) = \frac{eE_0}{m\omega^2}\left[\cos(\omega t + \phi) - \cos(\phi)\right] + \frac{eE_0}{m\omega}\sin(\phi)\cdot t \ . \tag{3.21}$$

The phase ϕ is important, because, first, it determines, whether, at all, the electron will return back to the position of the atom at $x = 0$ and, second, the velocity of the electron at $x = 0$ depends strictly on ϕ. The highest velocity and thus the kinetic energy is

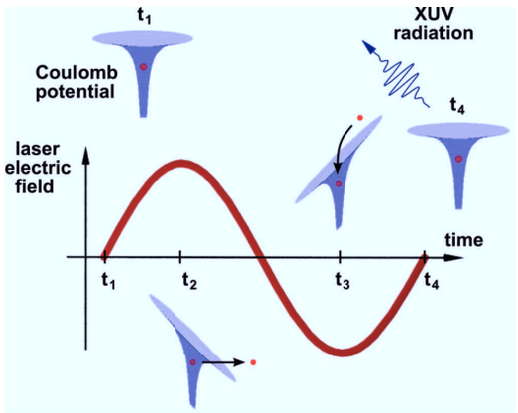

Figure 3.6.: Schematic presentation of the process of high harmonic generation [142]. The red line represents the electric field of the laser at the position of the gas atom, which Coulomb potential is plotted in blue. At time t_1, the electric field $E(t)$ is zero. Between t_1 and t_2, $E(t)$ continuously grows and the corresponding potential $eE(t) \cdot r$, where r denotes the distance from the atom and e the elementary charge, superimposes on the Coulomb potential. Consequently, a tunnel barrier is formed, through which the bound electron occupying the highest energy level (red sphere) is able to tunnel to the continuum states and therefore, escape the gas atom. Between t_2 and t_3, $E(t)$ reverses sign, which results in back acceleration of the electron towards the atom. At time t_4, the electron recombines with the atom, which leads to emission of extreme ultraviolet (XUV) and soft X-ray radiation.

about $3.17 \cdot U_p$ for $\phi \approx 18°, 198°$, etc., where we introduced the ponderomotive potential $U_p = e^2 {E_0}^2/(4m\omega^2)$.
Once the electron returns back to the atom, it can either scatter from the atom or recombine and emit the excess energy as a photon. In the latter case, the photon energy will be the sum of the kinetic energy and the ionization potential I, which can be at most $3.17 \cdot U_p + I$. Here, we heuristically showed the existence of the so-called cut-off law, which is indeed observed in experiments. In fact, this law was first derived from calculations [145] and, shortly after that, explained in the presented semi-classical [144] as well as a quantum mechanical model [27], where it is slightly modified due to quantum effects. For the typical experimental parameters in this work, the calculated cut-off energies are in the

range between 70 eV and 150 eV for noble gases. Nevertheless, in practical applications, they are reduced due to propagation effects, which will be discussed later in this chapter. It is interesting to note, that the spectrum of high harmonics from noble gases comprises *odd* harmonics. Noble gases are isotropic and therefore, high harmonics are emitted once in half a period of the electric field oscillation. This, in turn, translates into the spectrum via the Fourier transform, where the harmonics are separated by twice the laser frequency. The above described model, being also called the Three-Step-Model of tunnel ionization, propagation and recombination, was published by P. B. Corkum in 1993 [144] and is capable of explaining two other experimental findings, which are non-sequential double ionization [146] and above-threshold ionization [147]. In the former case, a coupling between the ion yield of single and double charged ions is observed. This can be explained by the Three-Step-Model as inelastic scattering of the returning electron, which ionizes the parent atom. In the above-threshold ionization experiments, electrons with high kinetic energies being multiple integers of the laser frequency are detected. In the picture of the Three-Step-Model, the returning electron scatters elastically from its parent atom and is further accelerated in the electric field of the laser. Therefore, albeit simple, the model nicely describes the experimental findings. On the other hand, it mixes the classical and quantum mechanics, which is resolved in a fully quantum theory by M. Lewenstein et al. [27].

So far, a single atom response was considered. But since the harmonics from a large number of atoms are superimposed, the effects of propagation and phase matching need to be taken into account. The phase matching condition for co-propagating radiation reads $\Delta k = qk(\omega) - k(q\omega) = 0$, where q is the harmonic order, k the wave number and ω the laser angular frequency [142]. The most important dispersion contributions arise from the neutral gas atoms, the free electrons and the particular experimental geometry, which, in the simplest case, can either be free focusing or waveguiding [142]. The wavevector mismatch between the laser light and the qth harmonic due to the neutral gas dispersion, Δk_{ng}, and due to the free electrons, Δk_{el}, are [142]

$$\Delta k_{ng} = [n(\omega) - n(q\omega)]\,\frac{q\omega}{c} \tag{3.22}$$

$$\Delta k_{el} = \frac{\omega_p^2(1-q^2)}{2c\omega q}\ , \tag{3.23}$$

with n being the real part of the refractive index and ω_p the plasma frequency. In general, due to $\Delta k_{ng} > 0$ and, clearly, $\Delta k_{el} < 0$, both contributions can cancel each other.

Experimentaly, the laser light is either focused into the gas emitted from a nozzle [148–

152] or it is focused inside a hollow, gas-filled capillary to guide the fundamental frequency [153–156]. It is known, that a focused Gaussian beam acquires a Guoy phase shift while passing the focal point, which approximately scales with the inverse Rayleigh length z_R [157]. Thus, the wavevector mismatch between the laser light and the qth harmonic is $\Delta k_f = (q-1)/z_R > 0$. Consequently, to achieve phase matching in the free focusing geometry, the free electron contribution must balance the neutral gas and Guoy phase contributions. This is different for the waveguide situation, where a step-index waveguide of radius a reduces the free space wave number by $k_w = -u_{nl}^2 c/(2a^2\omega)$, with u_{nl} being the lth zero of the Bessel function J_{n-1}. Therefore, the phase difference is [142]

$$\Delta k_w = \frac{u_{nl}^2 c(1-q^2)}{2qa^2\omega} < 0. \tag{3.24}$$

In the waveguide geometry, the neutral atom dispersion has to balance the free electron and waveguide dispersion. It was shown, that partial phase-matching can be achieved in both geometries [149, 153].

Furthermore, for few cycle pulses, an additional effect called the non-adiabatic self-phase matching becomes important [158] and enables the generation of photon energies up to 1.3 keV [159]. Different from the non-linear optics in the visible range, reabsorption of high harmonics by the gas limits the efficiency of phase matching [160].

At the end of this chapter, some optimization methods for high harmonics generation will be discussed. There are several optimization goals such as the photon flux, spectral shape and extension of the cut-off energy. The photon flux can be increased by appropriate temporal and spatial shaping of the driving laser pulses either using deformable mirrors or liquid crystal-based spatial modulators [161]. The closed-loop optimization procedure usually uses a genetic algorithm due to the large number of parameter combinations. In the same way it is possible to select harmonics with a high contrast ratio [161]. Additionally, in the waveguide geometry, a careful excitation of well-defined laser modes using a spatial light modulation increases the photon flux of high harmonics [162]. But also a tuning of the laser wavelength towards the blue part of the visible spectrum is predicted to increase the conversion efficiency due to a λ^{-x}, $x = 5-6$, scaling of the high harmonics yield [163]. Clearly, the wave packet of the free electron is less spread for a rapidly oscillating electric field and therefore, the recombination probability is higher than for a slowly oscillating field [31].

Turning towards the last point of the cut-off extension, three strategies are pursued, which are quasi-phase matching [164], few-cycle laser pulses [159, 165] and mid-infrared lasers [31]. Quasi-phase matching is applied in the waveguide geometry, where the diameter

of the hollow fiber is periodically modulated and thus, can compensate for any phase-mismatch, if the period length is chosen properly. For few-cycle laser pulses, the change of the electron density within one cycle is not negligible any more (non-adiabatic regime) and the mechanism called non-adiabatic self-phase matching is activated [158], which significantly improves the photon flux above 120 eV photon energy. The last approach of using mid-infrared laser wavelengths is motivated by the above mentioned cut-off law $E_{cut-off} = 3.17 \cdot U_p + I$, with $U_p \sim E_0^2 \lambda^2$ and λ being the wavelength. The present cut-off record achieved with this approach is about 1.6 keV photon energy [31].

3.3. Experimental Setup

This work employed two similar experimental setups, one located at the Research Centre Jülich in Germany and one at JILA, Boulder in the USA. Here, only the Jülich setup will be described, whereas the Boulder setup is presented in the Ph.D. thesis of C. La-o-vorakiat [166].

To start with the laser system, an oscillator (Griffin-3) and multipass amplifier system (Dragon) from KMLabs, Inc. was used to generate ultrashort, mJ pulses. The Ti:Sapphire oscillator produces 20-30 fs pulses with about 1 nJ per pulse at 80 MHz repetition rate. The pulses are then amplified to about 2 mJ per pulse, 30 fs at 2 kHz using the chirped pulse amplification technique [167]. The pulse duration is measured by means of Frequency Resolved Optical Gating using a custom-made device [168]. To minimize the thermal lens, the Ti:Sapphire crystal of the amplifier is cooled to 30-40 K in a closed-loop He cryorefrigerator (PT90, Cryomech). The amplifier is pumped at 30-40 W by an intra-cavity frequency doubled, nanosecond pulsed Nd:YLF laser (DM50, Photonics Industries, Inc.). The output photon energy is within the bandwidth between 1.55 and 1.63 eV with the central photon energy at 1.59 eV.

For high harmonics generation, a dedicated setup was build, comprising both commercial and custom-made parts. The commercial part (XUUS, KMLabs) included the glass capillary holder with gas inlets, a gas pressure control box with a Cole Parmer flow controller, two XY translation stages for the capillary alignment and one linear translation stage with a focusing lens (f=500 mm).

The schematic arrangement of the experiment is shown in Fig. 3.7. For pump-probe measurements, the laser beam was split into two parts. 90 % of the power was reflected from the beamsplitter and focused into a hollow glass capillary (150 μm inner diameter) for high harmonics generation. The second beam with 10 % of the input power was used to optically excite the sample. Two holes are drilled at the sides of the glass capillary to serve as gas inlet. Laser high harmonics were generated either in Ar (phase matching limited cut-off at about 52 eV) or Ne (cut-off higher than 72 eV) gas tuning the gas pressure inside the glass capillary to achieve phase matching. The residual infrared light was blocked by 150-200 nm thick Al filters (Lebow Company) with and without Ni mesh, placed after the capillary and after the sample.

Due to the high absorption of the extreme ultraviolet (XUV) radiation in air, the setup was placed in high vacuum.

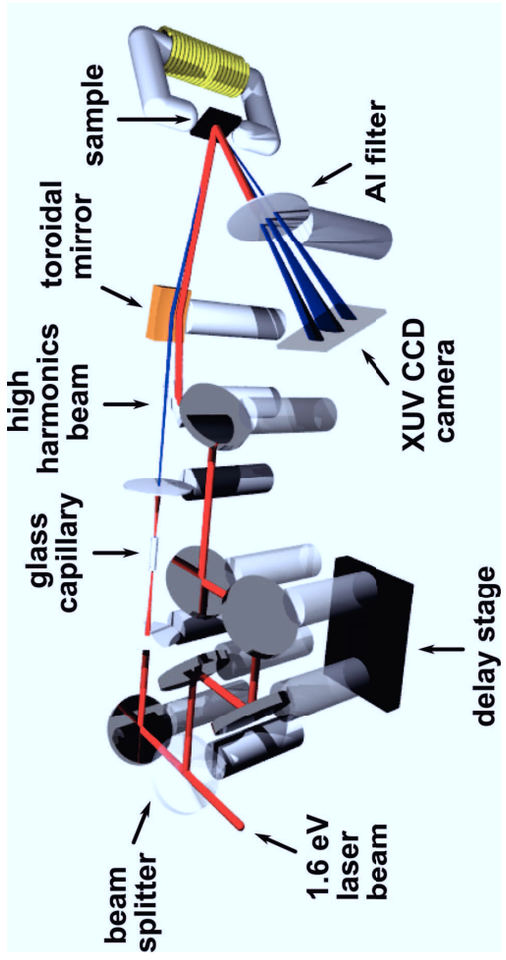

Figure 3.7.: Transversal magneto-optical Kerr effect (T-MOKE) setup for pump-probe spectroscopy with infrared light pump and high harmonics probe.

A gold-coated toroidal mirror (R_1=8605 mm, R_2=64 mm, ARW Optical) placed before the sample was used to focus the divergent XUV radiation onto the detector. To achieve a high reflectivity from the toroidal mirror (50-75 % depending on the polarization and photon energy), the angle of incidence was set to about 10° grazing incidence. After the reflection from the toroidal mirror, high harmonics beam was focused to a vertical line on the CCD detector due to aberration (astigmatism). The signal from the CCD detector was obtained by full vertical binning.

The laser pump pulses were temporally delayed with respect to the high harmonics probe pulses by a motorized, linear stage (IMS-Series, Newport). The zero-delay position on the linear stage, where the optical path lengths of the pump and probe pulses are identical on the micrometer scale, was found by overlapping the pump and the fundamental light transmitted through the capillary on a β-BaB_2O_4 crystal in a non-collinear frequency doubling geometry.

A special sample holder was constructed by B. Küpper (PGI-6, Research Centre Jülich) to meet several experimental requirements. The sample is located between two pole shoe pieces of a ferromagnetic yoke and can be tilted for optical alignment. Moreover, the sample is mounted on a heater for temperature-dependent measurements (Chapter 4.1.1) and, at the same time, to avoid heating of the yoke, a water-cooling is implemented. In addition, a linear stage for vertical movement allows to change between the sample and the β-BaB_2O_4 crystal, which is fixed under the sample.

In our experiment, the magneto-optical signal was measured in the transversal magneto-optical Kerr effect (T-MOKE) geometry (Chapter 3.1). For that purpose, the static magnetic field, created by a coil current and guided through the ferromagnetic yoke, was applied perpendicular to the plane of incidence of XUV radiation and, at the same time, in the plane of the sample, whereas the polarization of XUV radiation was set to p-polarization. The angle of incidence was adjusted close to 45° to achieve the highest magnetic asymmetry (Eq. 3.8). In this geometry, the reflectivity drops to about $5 \cdot 10^{-5}$ at the Ni 3p absorption edge (66 eV), due to the high absorption of p-polarized light close to the Brewster angle. The photon flux of the high harmonics source did not allow to use an additional grating for spectroscopic measurements. To solve this problem, the sample and grating were merged to one optical element by depositing 1 μm wide stripes of polymethylmethacrylate (PMMA) (200-300 nm thickness) or Si_3N_4 (17.5 nm thickness) with 1 μm separation on top of the magnetic layers. The spectrum of the XUV radiation was recorded for all harmonics simultaneously by a back-illuminated X-ray CCD camera (Andor iKon-L [169]) in the full vertical binning mode.

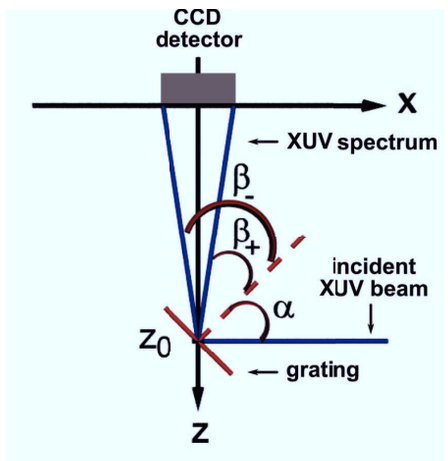

Figure 3.8.: Geometry of the XUV spectrometer used to derive Eq. 3.29. The grating is located at $z = z_0$ and the detector is placed on the x axis.

A LabView software to control the camera, magnetic field and the delay stage position for automated performance of the experiment was written by J. Lauer (PGI-6, Research Centre Jülich).

The photon energy calibration, i.e. the assignment of high harmonics wavelengths to the CCD pixel numbers, was done based on the knowledge of the $2p_{1/2}$ and $2p_{3/2}$ absorption edges of the Al filter (72.95 eV and 72.55 eV, respectively [170]) and the spectral structure of the harmonics. A similar procedure has also been described in [166]. The sharp 2p absorption edge of the Al filter determines the last harmonic being transmitted through the Al filter. In addition, the harmonic spectrum is known to comprise the peak wavelengths $\lambda = \lambda_0/q$ with λ_0 being the laser wavelength and $q = 1, 3, 5, 7, ...$ being the harmonic order, which allows one to determine λ of every harmonic. It has to be noted, that λ_0 can differ from the free space wavelength due to the so-called blue shift $\Delta\lambda_0$ [171]. Blue shift of the fundamental wavelength occurs, because free electrons from ionized gas atoms generated by the laser change the phase of the electric field of the fundamental in a time-dependent way. The blue shift of the qth harmonic roughly equals q times the blue

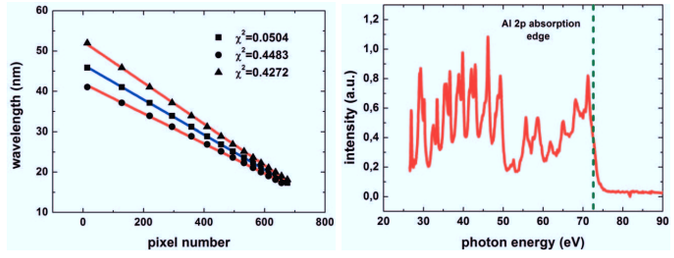

Figure 3.9.: Photon energy calibration curves for high harmonics with measured points and corresponding linear fits (left). The correct calibration (squares) is compared to the case, where the smallest harmonics wavelength is either shifted towards lower (circles) or higher (triangles) pixel numbers by one harmonic. The residual sum of squares, χ^2, is lowest for the correct calibration. A typical high harmonics spectrum from Ne gas after reflection from a Si_3N_4 grating in the -1 diffraction order is shown on the right. The sharp cut-off of the spectrum around 73 eV is due to the absorption of the Al filter (2p absorption edge) used to block the residual laser light.

shift of the fundamental [171]. Since, experimentally, the number of free electrons can be controlled by the laser intensity, the photon energies of high order harmonics can be shifted by few eV changing the laser intensity [166].
Given, x is the distance on the CCD chip (Fig. 3.8), the calibration $\lambda(x)$ is obtained by fitting $\lambda(x) = a \cdot x + b$ with a and b being constants. The validity of this expression will be shown now, starting from the grating equation

$$d(\sin|\alpha| - \sin|\beta|) = m\lambda \ , \tag{3.25}$$

with the grating constant d, the angle of incidence α measured with respect to the normal, the diffraction angle β and the diffraction order $m = 0, \pm1, \pm2, ...$ For the chosen coordinates (Fig. 3.8), β_+ for the $+m$th and β_- for the $-m$th order can be expressed as

$$\begin{aligned} |\beta_+| &= |\alpha| - \arctan\frac{x}{z_0} \ , \ x > 0 \\ |\beta_-| &= |\alpha| + \arctan\frac{x}{z_0} \ , \ x < 0 \ , \end{aligned} \tag{3.26}$$

or combining both equations

$$|\beta| = |\alpha| - \arctan\frac{x}{z_0} \approx |\alpha| - \frac{x}{z_0} \ , \tag{3.27}$$

harmonic order	photon energy (eV)	10^3 photons/s after the sample	10^7 photons/s after the source
19	30.2	7	0.1
21	33.4	7	0.2
23	36.6	9	0.4
25	39.7	10	0.8
27	42.9	9	1.5
29	46.1	12	3.9
31	49.3	9	6.9
33	52.5	2	8.5
35	55.6	6	1.5
37	58.8	6	0.8
39	62.0	4	0.6
41	65.2	5	1.1
43	68.4	7	2.3
45	71.5	9	4.2

Table 3.1.: High harmonics photon flux from Ne gas measured on the X-ray CCD camera after the $Si/SiO_2/Ta(3\ nm)/Fe(4\ nm)/Al(3\ nm)$ sample with a Si_3N_4 grating of 17.5 nm thickness. The photon flux after the source was calculated based on the reflectivity of the sample and the toroidal mirror as well as the transmission of the Al filter [172].

because $x/z_0 << 1$ in the experiment. Inserting Eq. 3.27 in Eq. 3.25, we obtain

$$\frac{x}{z_0} = |\alpha| - \arcsin\left[\sin|\alpha| - \frac{m\lambda}{d}\right] \approx \frac{m\lambda}{d\cos|\alpha|} \ , \tag{3.28}$$

using the approximation $\lambda/d \approx 25\ nm/2000\ nm << 1$. Finally, the expression for the photon energy calibration reads

$$\lambda(x) = \frac{d\cos|\alpha|}{mz_0} \cdot x \ . \tag{3.29}$$

Calibration curves obtained with the above described method as well as a typical high harmonics spectrum from Ne gas are shown in Fig. 3.9. Reduced χ^2, defined as residual sum of squares divided by the number of degrees of freedom (see, e.g. [173]), is used here to compare, how well the linear equation 3.29 describes the wavelength dependence on the pixel number for the case, where the smallest harmonic wavelength is either shifted

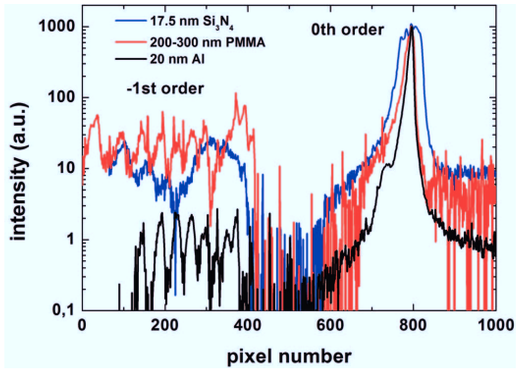

Figure 3.10.: High harmonics spectrum from Ne gas for $Si/SiO_2/Fe/Ru/Ni/Al$ layers with three different grating materials and a constant grating period of 2 μm. Note the logarithmic intensity scale.

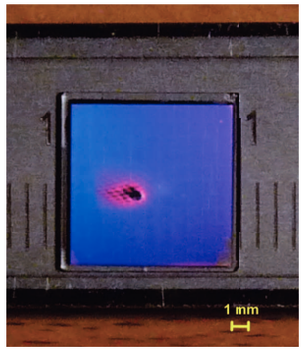

Figure 3.11.: Photograph of a glass/Ni/Ru/Fe/Al sample with a PMMA grating on top. The colors originate from lamp light diffraction from the grating. Note, that during the photography the laser is turned off. The figure illustrates the effect of XUV radiation on the PMMA refractive index for visible light. High dosis of XUV radiation from Ar gas can even result in damage of PMMA. The mesh structure is due to the Ni mesh supporting the Al filters.

towards lower or higher pixel numbers by one harmonic. Only for the correct photon energy calibration, χ^2 reaches the lowest value (squares in Fig. 3.9).

From the measured number of counts on the CCD sensor as well as from the literature values for the photon energy-resolved reflectivity of the sample, the toroidal mirror and the transmission of the Al filter [172], it is possible to estimate the photon flux per harmonic from Ne (Tab. 3.1). These values were estimated under the assumption of spectrally constant grating efficiency, i.e. the spectral weight of each harmonic in the -1st diffraction order is the same in the 0th order. The obtained harmonic-resolved photon flux has rather to be considered as an order of magnitude estimation than exact value due to the uncertain parameters such as grating efficiency, sample reflectivity, etc. Nevertheless, the photon flux compares well to the available data from a similar light source [174]. The overall photon flux from Ne gas for the harmonic orders $n = 19$ to $n = 45$ is estimated to be $3 \cdot 10^8$ photons/s. On the other hand, the photon flux from Ar gas was measured with a calibrated Si p-n junction photodiode (AXUV 100, IRD, Inc.) to be $2 \cdot 10^{10}$ photons/s, two orders of magnitude lower than reported in [174].

Since a stable intensity of the XUV light source is important for many experiments, we characterized the pulse-to-pulse stability of the laser harmonics from Ar gas using a gated microchannel plate detector. Due to the detector time resolution of 2 ns, the harmonics pulse duration below 10 fs [175] and the laser repetition rate of 2 kHz, it was possible to record frames from single high harmonic pulses. The integrated frame-to-frame intensity variation was measured to be 10% [176, 177]. The reason for such a relatively high variation could be either intensity fluctuations of the laser light, which are amplified in the nonlinear frequency upconversion process or, possibly, fluctuations of the gas density, or both.

To further optimize the photon flux in the $\pm$1st diffraction order, we tuned the efficiency of the grating fabricated on top of the sample by changing the grating material (Al, Si_3N_4, polymethylmethacrylate (PMMA)) and the layer thickness (Fig. 3.10). The ratio between the 0th and -1st order intensity is < 0.3 % for 10 nm and 15 nm Al, 0.3 % for 20 nm Al, 2 % for 17.5 nm Si_3N_4 and about 12 % for 200-300 nm PMMA gratings. To understand the measured efficiencies, simulations are required, which are beyond the scope of this work.

It has to be noted, that PMMA can be modified or even damaged by the action of combined XUV and intense, infrared (1.5 eV) laser radiation [178]. By excitations above the band gap, XUV pulses generate free electrons in the dielectric material, which increase the absorption of the intense 1.5 eV light and, consequently, PMMA is heated by the laser. In addition, XUV radiation can create permanent defects, e.g. color centers, in the material. Taking these effects into account, PMMA grating deposited on top of the sample is not

suitable for measurements with infrared laser pump and high harmonics probe. The advantage of PMMA gratings is a relatively short fabrication process compared to Si_3N_4 gratings and, without the infrared laser pump, they are suitable for static reflectivity measurements.
On the other hand, the permanent modification of the PMMA refractive index for visible light by a high dosis of XUV radiation was used to determine the beam size of high harmonics on the sample, which is (3.19 ± 0.09) mm^2 (Fig. 3.11).

4. Experimental Results and Discussion

This chapter is divided in two parts. In the first part, studies of photon energy-resolved and thus layer-selective, magneto-optical asymmetry of interlayer exchange coupled Fe/Ru/Ni -based layers is presented. Moreover, the layer-selective and temperature-dependent magnetization reversal of antiferromagnetically coupled Fe and Ni layers is traced. The second part is concerned with time- and layer-resolved measurements on the femtosecond timescale. First, we focus on laser-induced dynamics of interlayer exchange coupling energy J_1 in Fe/Ru/Ni -based layers using the pump-probe technique with 1.5 eV pump and either 3.0 eV or high harmonics probe. Subsequently, we analyze layer-selective spin dynamics in Fe/Ru/Ni -based layers for parallel and antiparallel magnetization orientation of the Fe and Ni layers and for various optical pump fluences. The magnetization orientation-dependent spin dynamics in the Fe layer (transient magnetization enhancement for parallel, transient demagnetization for antiparallel orientation) is interpreted as a consequence of superdiffusive spin transport from the Ni to the Fe layer and corroborated by calculations, which agree well with experimental data within a defined fluence range.

4.1. Static Results

4.1.1. Layer-Selective Magnetization of Interlayer Exchange Coupled Fe/Ru/Ni -Layers

We studied the layer- and element-selective magnetization employing the transversal magneto-optical Kerr effect (T-MOKE) with laser high harmonics radiation generated in Neon gas. The measurements presented in this chapter were carried out at PGI-6, Research Centre Jülich in Germany, whereas the samples were prepared by J. M. Shaw at NIST, Boulder in the USA. Although the high harmonics spectrum exhibits intensity peaks at quasi-discrete photon energies [179] separated by about 3 eV (Fig. 4.1, 4.3, 4.5, 4.7), it is possible to extract a smooth, photon energy-dependent magnetic asymmetry, since the spectrum is quasi-continuous between the harmonics.

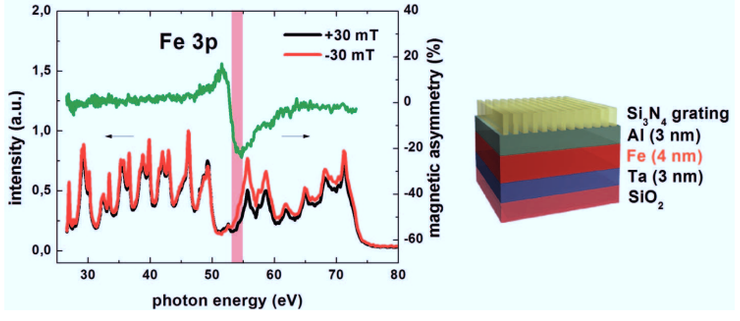

Figure 4.1.: Magnetic field-dependent high harmonics spectra after reflection from the $Si/SiO_2/Ta(3\ nm)/Fe(4\ nm)/Al(3\ nm)$ sample for $\pm$ 30 mT (red and black curves) and magnetic asymmetry around the Fe 3p absorption edge (green curve). The Fe 3p absorption edge is marked by the pink box. The sample, which was illuminated at 45° angle of incidence, is depicted on the right side. The Si_3N_4 grating is used for spectral separation of high harmonics radiation.

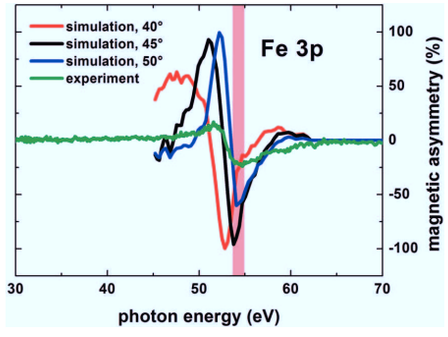

Figure 4.2.: Comparison between the measured magnetic asymmetry for Fe at 45° angle of incidence (green curve) with a simulation for different angles of incidence for the $Si/SiO_2/Ta(3\ nm)/Fe(4\ nm)/Al(3\ nm)$ sample. The Fe 3p absorption edge is marked by the pink box. Note, that the peak positions in the double peak structure don't correspond to the $3p_{1/2}$ and $3p_{3/2}$ absorption edges of Fe, which cannot be separated in our experiment.

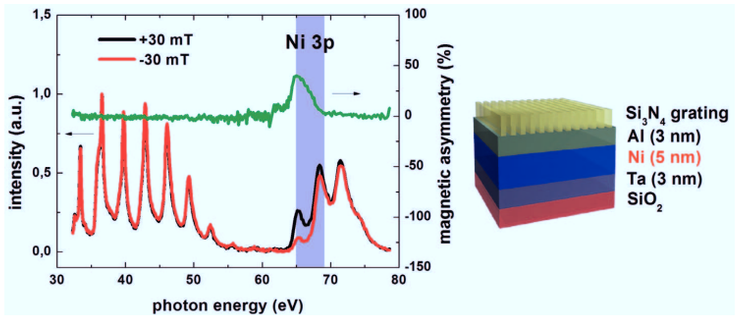

Figure 4.3.: Magnetic field-dependent high harmonics spectra after reflection from the $Si/SiO_2/Ta(3\ nm)/Ni(5\ nm)/Al(3\ nm)$ sample for ± 30 mT (red and black curves) and magnetic asymmetry around the Ni 3p absorption edge (green curve). The Ni 3p absorption edge is marked by the blue box. The sample, which was illuminated at 45° angle of incidence, is depicted on the right side. The Si_3N_4 grating is used for spectral separation of high harmonics radiation.

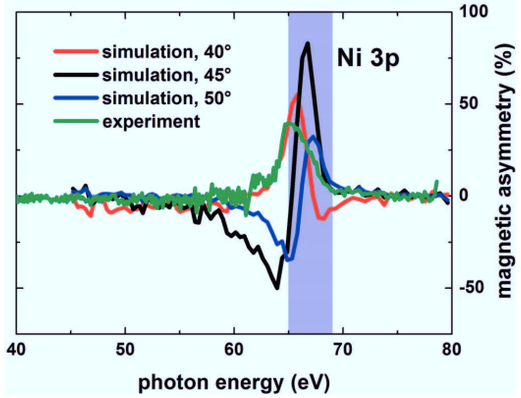

Figure 4.4.: Comparison between the measured magnetic asymmetry for Ni at 45° angle of incidence (green curve) with a simulation for different angles of incidence for the $Si/SiO_2/Ta(3\ nm)/Ni(5\ nm)/Al(3\ nm)$ sample. The Ni 3p absorption edge is marked by the blue box.

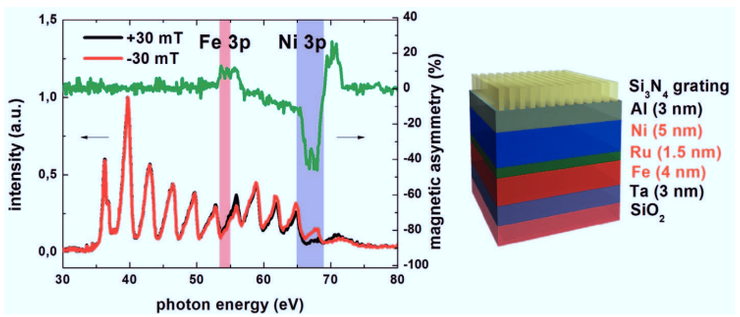

Figure 4.5.: High harmonics spectra (red and black curves) and magnetic asymmetry (green curve) for parallel alignment of the Ni and Fe magnetization for the $Si/SiO_2/Ta(3\ nm)/Fe(4\ nm)/Ru(1.5\ nm)/Ni(5\ nm)/Al(3\ nm)$ sample. Pink- and blue-coloured boxes indicate the 3p absorption edges of Fe and Ni, respectively. The sample, which was illuminated at 45° angle of incidence, is depicted on the right side. The Si_3N_4 grating is used for spectral separation of high harmonics radiation.

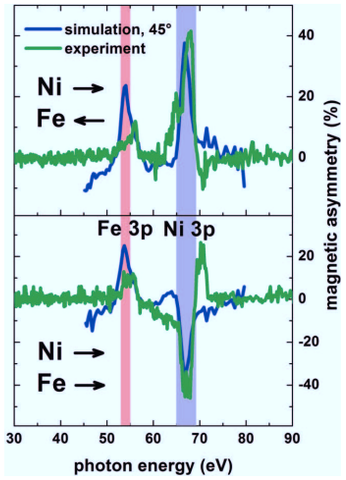

Figure 4.6.: Measured (green curves) and simulated (blue curves) magnetic asymmetry for antiparallel (top) and parallel (bottom) magnetization alignment of the Fe and Ni layers for the $Si/SiO_2/Ta(3\ nm)/Fe(4\ nm)/Ru(1.5\ nm)/Ni(5\ nm)/Al(3\ nm)$ sample. Pink- and blue-coloured boxes indicate the 3p absorption edges of Fe and Ni, respectively.

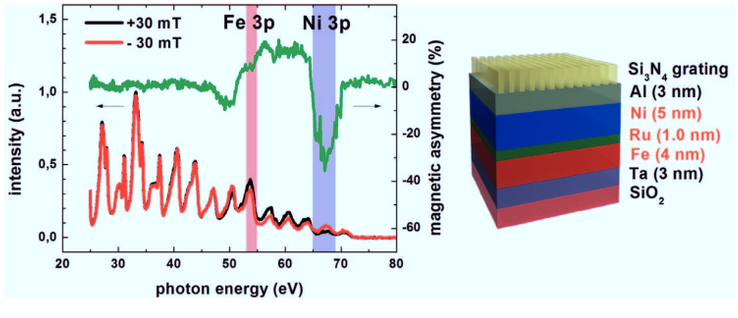

Figure 4.7.: Magnetic field-dependent high harmonics spectra (red and black curves) after reflection from the Si/SiO_2/Ta(3 nm)/Fe(4 nm)/Ru(1 nm)/Ni(5 nm)/Al(3 nm) sample and magnetic asymmetry (green curve) at the Ni (blue box) and Fe (pink box) 3p absorption edges. The difference between data from Fig. 4.5 and Fig. 4.7 is the thickness of the Ru interlayer, which is 1.5 nm in Fig. 4.5 and 1.0 nm in Fig. 4.7. The sample, which was illuminated at 45° angle of incidence, is depicted on the right side. The Si_3N_4 grating is used for spectral separation of high harmonics radiation.

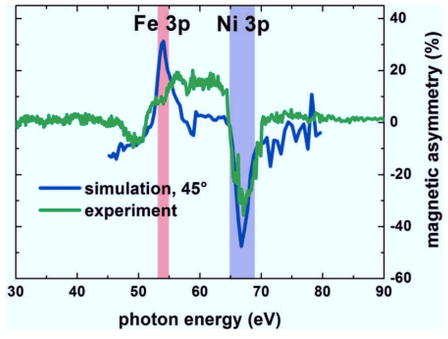

Figure 4.8.: Measured (green curve) and simulated (blue curve) magnetic asymmetry at the Ni (blue box) and Fe (pink box) 3p absorption edges for the Si/SiO_2/Ta(3 nm)/Fe(4 nm)/Ru(1 nm)/Ni(5 nm)/Al(3 nm) sample. The magnetization of Fe and Ni layers is aligned parallel.

To test our experimental technique, we first prepared Si/SiO_2/Ta(3 nm)/Fe(4 nm)/Al(3 nm) and Si/SiO_2/Ta(3 nm)/Ni(5 nm)/Al(3 nm) layers on Si substrate with only one ferromagnetic layer and a 17.5 nm thick Si_3N_4 grating on top of the layer stack [180] by use of ion beam sputtering. The Si_3N_4 grating was used for spectral separation of high harmonics radiation.

To prevent oxidation, the ferromagnetic layers were protected by an Al capping layer, being transparent for photon energies between 20 and 72 eV [181]. The Ta layer was used for a proper crystal texture of the layers.

We recorded the magnetic asymmetry for single Fe and Ni layers as well as for Fe/Ru/Ni layers. The magnetic asymmetry of the single Fe film shows a double peak structure with a change of sign (Fig. 4.1) at the Fe 3p absorption edge (53-55 eV [181]). The magnetic asymmetry reaches from 20 % to -20 %. Note, that the peak positions don't correspond to the $3p_{1/2}$ and $3p_{3/2}$ absorption edges of Fe, which cannot be separated in our experiment. We performed simulations of magnetic asymmetry for different angles of incidence using Maxwell equations with boundary conditions for a multilayer structure (Fig. 4.2). The details of the method are described at the end of chapter 3.1. The magnitude of the asymmetry obtained from measurements is significantly lower than predicted by simulations, which we attribute to a partial oxidation of the Fe layer despite of the capping layer. The experimental data were recorded at 45° angle of incidence and therefore, only simulated magnetic asymmetry for 45° (Fig. 4.2, black curve) reproduces the spectral shape observed experimentally.

Repeating the experiment for the Ni layer instead of the Fe layer, we observed one peak in the magnetic asymmetry at the Ni 3p absorption edge (65-69 eV [181]) with a magnitude of about 40% (Fig. 4.3). Compared to simulations of magnetic asymmetry for 45° angle of incidence (Fig. 4.4), the peak is slightly shifted towards lower photon energies. In addition, the magnitude of the peak is lower than predicted, possibly, due to partial oxidation of the Ni layer.

In the next step, we prepared a series of Si/SiO_2/Ta(3 nm)/Fe(4 nm)/Ru/Ni(5 nm)/Al(3 nm) samples containing two ferromagnetic layers and a Ru spacer layer with varying thickness (0.5, 1.0 and 1.5 nm), mediating the interlayer exchange coupling between the Ni and Fe magnetization. Ru is known to be a favourable material to achieve a strong interlayer exchange coupling [182]. Indeed, static hysteresis curves presented later in this chapter show antiferromagnetic coupling between the Ni and Fe magnetization for the 0.5 nm and 1.5 nm thick Ru layers, whereas, for the 1.0 nm Ru thickness, the coupling was ferromagnetic.

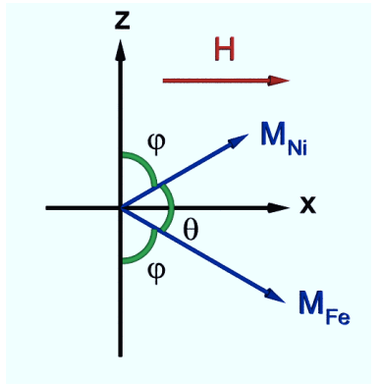

Figure 4.9.: Simple model for the interlayer exchange coupled magnetization of Ni and Fe layers in the external magnetic field H (Eq. 4.2-4.5).

Resonant T-MOKE enables one to obtain magneto-optical signals from the Fe and Ni layer separately (Fig. 4.5-4.8). The magnetic signal around 55 eV can be attributed to the Fe and around 67 eV to the Ni layer. Compared to a single Fe layer, the magnetic asymmetry is reduced for the buried Fe layer from about 20 % to 10 %. In addition, the shape of the Fe peak changes from a double peak in a single Fe layer to a single peak in the multilayer (Fig. 4.6). For the Ni layer located above the Fe layer in the layer stack, the magnetic asymmetry amounts to about 40 % like in a single Ni layer.
By changing the relative magnetization alignment from parallel to antiparallel applying an external magnetic field, the relative sign of the Fe and Ni asymmetry is reversed (Fig. 4.6). The observed behaviour can be reproduced by simulations assuming, that the non-diagonal elements of the dielectric tensor reverse their sign, if the magnetization is reversed, too.
We studied the interlayer exchange coupling (IEC) in our Fe/Ru/Ni layers using the combination of a SQUID magnetometer and magneto-optical measurements, including layer-selective, resonant T-MOKE.
In general, the energy term due to the IEC for two ferromagnetic layers, whose magnetization is aligned under the angle Θ with respect to each other, can be written as [46]

$$E = -J_1 \cos\Theta - J_2 \cos^2\Theta + ... \,, \tag{4.1}$$

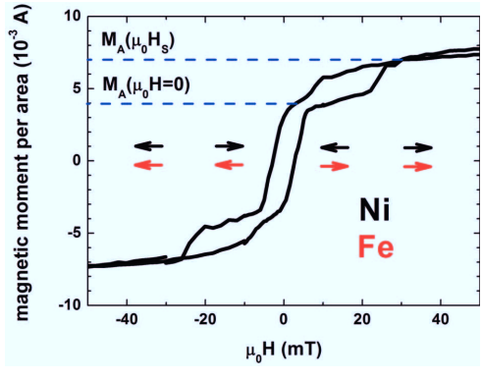

Figure 4.10.: Magnetic moment per area M_A for the antiferromagnetically coupled Si/SiO_2/Ta(3 nm)/Fe(4 nm)/Ru(1.5 nm)/Ni(5 nm)/Al(3 nm) sample. $M_A(\mu_0 H_S)$ and $M_A(\mu_0 H = 0)$ denote the magnetic moment per area for the Ni and Fe magnetization, being either parallel ($H = H_S$) or antiparallel ($H = 0$).

where J_1 describes the parallel or antiparallel coupling, J_2 the 90°-coupling, etc. (see chapter 2.2) . In a simple model, the total energy E per area unit for the two parallel or antiparallel coupled ferromagnetic layers in external magnetic field H, neglecting the magneto-crystalline anisotropy and higher order terms J_i, $i \geq 2$, can be written as [183, 184]

$$E = -J_1 \cos\Theta - \mu_0 \left(M_{Ni} d_{Ni} + M_{Fe} d_{Fe}\right) H \sin\varphi. \tag{4.2}$$

Here, M denotes the magnetization of the respective layer, d its thickness and $M \cdot \sin\varphi$ the projection of M on the direction of H (Fig. 4.9). The procedure of the total energy minimization with respect to φ is useful to derive an expression for J_1. The first derivative of $E(\varphi)$ reads

$$\frac{\partial E}{\partial \varphi} = \cos\varphi \left[-4J_1 \sin\varphi - \mu_0 (M_{Ni} d_{Ni} + M_{Fe} d_{Fe}) H\right] \ . \tag{4.3}$$

The energy minimization requires

$$J_1 = -\frac{\mu_0 (M_{Ni} d_{Ni} + M_{Fe} d_{Fe}) H}{4 \sin\varphi}. \tag{4.4}$$

Eq. 4.4 can be evaluated for the saturation field H_S, saturation magnetization M_S, $\sin(\varphi) = 1$ and reads

$$J_1 = -\frac{\mu_0(M_{S,Ni}d_{Ni} + M_{S,Fe}d_{Fe})H_S}{4}. \tag{4.5}$$

It has to be noted, that a magnetometer measures the total magnetic moment, being equal to $A(M_{Ni}d_{Ni}+M_{Fe}d_{Fe})$, where A denotes the surface area of the sample. Nevertheless, if the layer thickness and the total surface area are known, it is possible to determine $M_{S,Ni}$ and $M_{S,Fe}$ separately by solving a system of two linear equations

$$M_{S,Fe} \cdot d_{Fe} - M_{S,Ni} \cdot d_{Ni} = M_A(\mu_0 H = 0) \tag{4.6}$$

$$M_{S,Fe} \cdot d_{Fe} + M_{S,Ni} \cdot d_{Ni} = M_A(\mu_0 H_S) \ , \tag{4.7}$$

where M_A denotes the measured total magnetic moment divided by the surface area.
Here, it is assumed, that the Fe and Ni magnetization is parallel for $M_A(\mu_0 H_S)$ and antiparallel for $M_A(\mu_0 H = 0)$ (Fig. 4.10). For the sample with 1.5 nm Ru thickness, $M_{S,Fe} = (1.33 \pm 0.07) \cdot 10^6$ A/m and $M_{S,Ni} = (0.42 \pm 0.05) \cdot 10^6$ A/m at 290 K, which are slightly lower than the values for crystalline bulk materials [185].
As mentioned above, we found an antiferromagnetic (AF) coupling for the 1.5 nm Ru thickness (Fig. 4.10) with $J_1 = -(0.48 \pm 0.03)10^{-4}\mathrm{J/m}^2$ and, for the 0.5 nm Ru thickness, $J_1 = -(1.10 \pm 0.04)10^{-4}\mathrm{J/m}^2$. It is known, that the coupling strength exhibits an oscillatory behaviour depending on the thickness of the spacer layer [47, 182]. Therefore, we note, that this value is not the peak value of the AF-IEC strength, which is expected to be higher. For instance, Co/Ru multilayers show a peak AF-IEC strength of $-5 \cdot 10^{-3}\mathrm{J/m}^2$ [186]. Between the 0.5 nm and 1.5 nm Ru thickness, we found a ferromagnetic coupling for 1.0 nm Ru (Fig. 4.11), but its magnitude could not be determined using the described method. To determine the strength of ferromagnetic coupling between the Ni and Fe magnetization, an additional layer with a strong AF coupling to either the Ni or Fe layer is required [182].
Similar to the magnetometer measurements, it is possible to record M-H-curves, resolved for the Ni and Fe layers, using a slight redefinition of the magnetic asymmetry (Eq. 3.8) to

$$A_{ref}(H) = \frac{I(H) - I(H_{ref})}{I(H) + I(H_{ref})}, \tag{4.8}$$

where I denotes the reflected intensity of the p-polarized light and $H_{ref} = 32\ \mathrm{mT}/\mu_0$ the reference magnetic field, which is held constant during the measurements, whereas H is sweeped, i.e. after each field value H we applied H_{ref} to measure the asymmetry amplitude. For the 1.5 nm Ru sample, we observed three magnetization reversal or switching

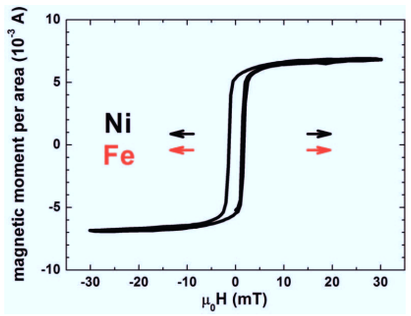

Figure 4.11.: Magnetic moment per area M_A for the ferromagnetically coupled Si/SiO_2/Ta(3 nm)/Fe(4 nm)/Ru(1 nm)/Ni(5 nm)/Al(3 nm) sample.

events for the Ni and one switching event for the Fe magnetization, while sweeping $\mu_0 H$ from positive to negative values (Fig. 4.12). Beginning with a positive magnetic field higher than 10 mT, the magnetization of Fe and Ni is parallel and oriented in the field direction and therefore, $A_{ref}^{Ni,Fe} = 0$ for $\mu_0 H = +32$ mT. Reducing the field to about +10 mT, the Ni magnetization rotates towards the antiparallel orientation with respect to Fe, which results in a decrease of A_{ref}^{Ni} to about -40 %. At few mT below zero field, the Fe magnetization reverses (jump in A_{ref}^{Fe} from 0 to 10 %) with the consequence, that the Ni magnetization reverses, too, due to the AF-IEC. Therefore, like at the beginning, $A_{ref}^{Ni} = 0$. When the external field reaches -20 mT, it is strong enough to overcome the AF-IEC and to rotate the Ni magnetization into the field direction, which results in $A_{ref}^{Ni} \approx -35\%$, comparable with A_{ref}^{Ni} around zero field. We attribute the fact, that the Fe layer reverses first, to its lower coercitive field compared to the Ni layer.

We measured $A_{ref}(H)$ for three different temperatures (290 K, 420 K and 570 K) and found, that the IEC strength, being proportional to the saturation field (Eq. 4.5), decreases at 420 K and vanishes completely at 570 K (Fig. 4.13-4.14). The effects contributing to the temperature dependence of the IEC, being discussed in the literature, include the spacer layer [48, 187], interface [188] and magnetic layer [189] contributions. In the model of P. Bruno [48], explaining the IEC due to quantum interferences in the spacer layer, the most important contribution to the IEC comes from the electrons with energies around E_F. Because of the thermal smearing, electrons are removed from the Fermi edge

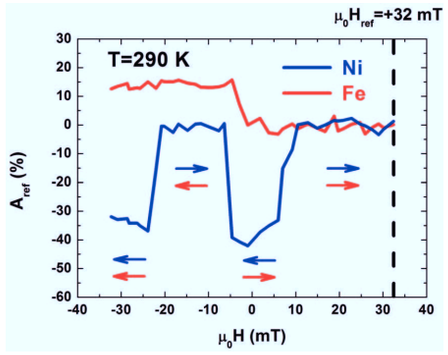

Figure 4.12.: Fe and Ni layer-selective parameter A_{ref} (definition see Eq. 4.8) for the Si/SiO_2/Ta(3 nm)/Fe(4 nm)/Ru(1.5 nm)/Ni(5 nm)/Al(3 nm) sample for $\mu_0 H_{ref} = +32$ mT measured at 290 K, which corresponds to the sweep direction from positive to negative magnetic fields. While the Fe magnetization reverses once at about -5 mT, the Ni magnetization reverses three times at -25, -5 and +5 mT as a consequence of the antiferromagnetic interlayer exchange coupling.

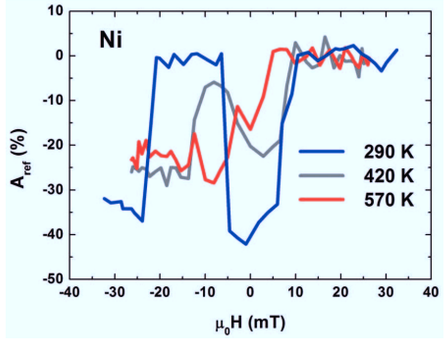

Figure 4.13.: Temperature-dependent parameter A_{ref} at the Ni 3p absorption edge for the same sample as in Fig. 4.12. The sweep direction of the magnetic field is from positive to negative values. The antiferromagnetic coupling strength between the Ni and Fe layers decreases with increasing temperature and vanishes at 570 K.

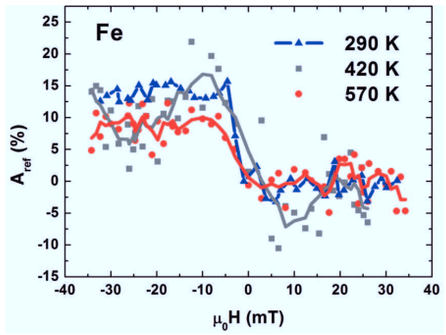

Figure 4.14.: Temperature-dependent parameter A_{ref} at the Fe 3p absorption edge for the same sample as in Fig. 4.12. The sweep direction is from positive to negative magnetic fields. To improve the signal-to-noise-ratio from the (bottom) Fe layer, adjacent averaging have been performed for the data at 420 K and 570 K (lines), whereas the original data are also displayed (points).

and occupy higher energy states, thus decreasing the magnitude of the IEC with increasing temperature in the case of a metallic spacer layer. The interface contribution originates from the temperature dependence of the electronic reflection coefficients at the ferromagnet/spacer interface. The last proposed mechanism involves the magnonic contribution to the free energy of the ferromagnetic layers [189]. For the sample studied here, all three proposed effects may contribute to the temperature dependence of the IEC.

4.2. Femtosecond Dynamics

4.2.1. Laser-Induced Femtosecond Dynamics of Interlayer Exchange Coupling in Fe/Ru/Ni -Layers

We studied the temporal response of the IEC energy J_1 (Eq. 4.1) after the femtosecond laser excitation, probing either with high harmonics or visible light. For a description of the pump-probe setup using 1.5 eV pump and 3.0 eV probe, the reader is referred to the master theses of M. Plötzing [190] and B. Heller [191]. Here, two different sets of samples with antiferromagnetic interlayer exchange coupling between the Ni and Fe layers were studied, namely, Si/SiO_2/Ta(3 nm)/Fe(4 nm)/Ru(1.5 nm)/Ni(5 nm)/Al(3 nm) fabricated at NIST, Boulder and Si/SiO_2/Fe(4 nm)/Ru(1 nm)/Ni(5 nm) from PGI-6, Research Centre Jülich.
Generally, the time-dependence of $J_1(t)$ can be expressed as

$$\frac{\partial J_1(t)}{\partial t} = -\frac{\mu_0}{4}\left[\left(\frac{\partial M_{S,Ni}}{\partial t}d_{Ni} + \frac{\partial M_{S,Fe}}{\partial t}d_{Fe}\right)H_S + \left(M_{S,Ni}d_{Ni} + M_{S,Fe}d_{Fe}\right)\frac{\partial H_S}{\partial t}\right] , \tag{4.9}$$

where t denotes the time and $d_{Fe,Ni}$ is the layer thickness. Although H_S is not an intrinsic quantity of the sample, like e.g. the magnetization, it is easily accessible in the experiment. From measurements of two different AF-coupled Fe/Ru/Ni samples and employing two different techniques, namely, probing with high harmonics (Fig. 4.15-4.16) and visible light (Fig. 4.17-4.19), the time-dependence of H_S appears to be negligible and the only contribution is due to the time-dependence of M_S, in particular of $M_{S,Ni}$.
Thus, experimentally, one finds (see also Eq. 4.5)

$$\mu_0 H_S(t) = \frac{-4J_1(t)}{M_{S,Ni}(t)d_{Ni} + M_{S,Fe}(t)d_{Fe}} = \text{const.} , \tag{4.10}$$

and hence

$$J_1(t) \sim -(M_{S,Ni}(t)d_{Ni} + M_{S,Fe}(t)d_{Fe}) . \tag{4.11}$$

In the layer- and time-resolved experiment using high harmonics probe, the saturation magnetization $M_{S,Ni}$ of the Ni layer is reduced by about 30% after the laser pulse excitation (Fig. 4.15), whereas $M_{S,Fe}$ is almost unaffected (Fig. 4.16), which in total results in transient reduction of $J_1(t)$, since H_S remains constant. The normalized, transient decrease of J_1 at $t = 0.5$ ps after the laser excitation, $[J_1(t<0) - J_1(t=0.5\text{ ps})]\,/J_1(t<0)$, is measured to be (8 ± 6) %.

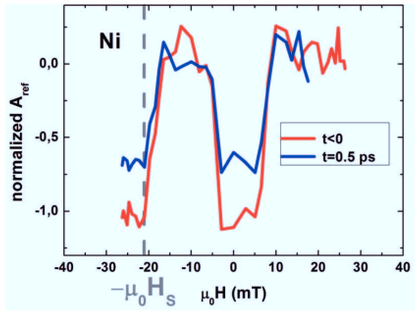

Figure 4.15.: Normalized parameter A_{ref} at the Ni 3p absorption edge (A_{ref} between 0 and -1 for $t < 0$) for the Si/SiO_2/Ta(3 nm)/Fe(4 nm)/Ru(1.5 nm)/Ni(5 nm)/Al(3 nm) sample before and 0.5 ps after the excitation laser pulse. The sweep direction is from positive to negative magnetic fields. While the magnetization of the Ni layer is quenched at $t = 0.5$ ps, the saturation magnetic field H_S (grey dashed line) doesn't change.

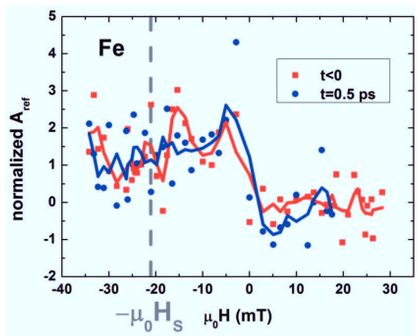

Figure 4.16.: Normalized parameter A_{ref} at the Fe 3p absorption edge (A_{ref} between 0 and 1 for $t < 0$) for the Si/SiO_2/Ta(3 nm)/Fe(4 nm)/Ru(1.5 nm)/Ni(5 nm)/Al(3 nm) sample before and 0.5 ps after the excitation laser pulse. The sweep direction is from positive to negative magnetic fields. For $H = -H_S$, the magnetization of Ni and Fe layers is saturated (see Fig. 4.15). To improve the signal-to-noise-ratio from the (bottom) Fe layer, adjacent averaging have been performed for the data (lines), whereas the original data are also displayed (points).

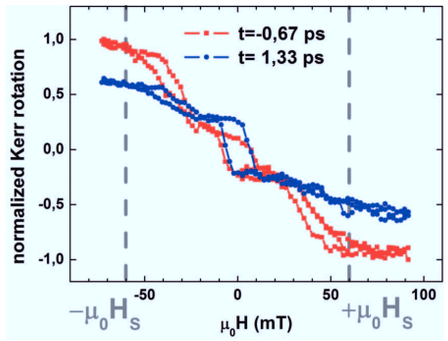

Figure 4.17.: Magnetic hysteresis for the Si/SiO_2/Fe(4 nm)/Ru(1 nm)/Ni(5 nm) sample, measured with visible light (1.5 eV pump and 3.0 eV probe) for $t < 0$ and $t = 1.33$ ps. The saturation magnetic field H_S is marked by the grey, dashed line. The laser pump pulse affects only the magnitude of the Kerr rotation and not H_S.

Under certain conditions, it is possible to extract layer-selective, magneto-optical signals with visible light from magnetic hysteresis loops. In this case, the idea is to compare the Kerr rotation Θ_K at two points in the hysteresis loop, where the magnetization of Fe and Ni is either aligned antiparallel ($H = 0$) or parallel ($H = H_S$). The system of two linear equations is given by

$$b \cdot M_{S,Fe} - a \cdot M_{S,Ni} = \Theta_K(H = 0) \tag{4.12}$$

$$b \cdot M_{S,Fe} + a \cdot M_{S,Ni} = \Theta_K(H = H_S)\ . \tag{4.13}$$

For the antiferromagnetically coupled Si/SiO_2/Fe(4 nm)/Ru(1 nm)/Ni(5 nm) sample, the saturation magnetization for Fe and Ni was measured with a SQUID magnetometer to be $M_{S,Fe} = (1.67 \pm 0.01) \cdot 10^6$ A/m and $M_{S,Ni} = (0.427 \pm 0.007) \cdot 10^6$ A/m at 290 K. $\Theta_K(H = 0)$ and $\Theta_K(H = H_S)$ were extracted from L-MOKE measurements and the coefficients a and b were determined from Eq. 4.12-4.13.
Recording the magnetic hysteresis curves for different delay times between the optical pump (1.5 eV) and probe (3.0 eV), we assume a and b to be time-independent. This assumption might be questioned, since several groups showed, that a and b indeed change with pump-probe delay time [80, 192]. Nevertheless, it is reasonable to consider, that these changes are small compared to the magnetization changes and therefore, it is sufficient to

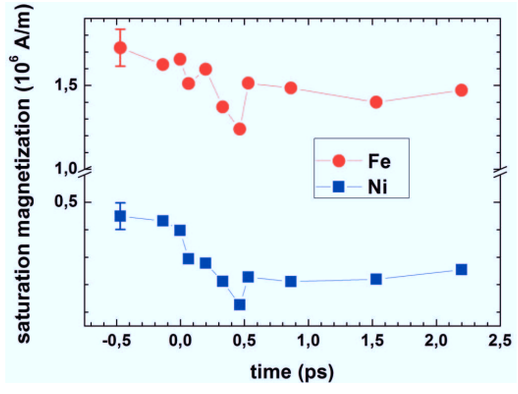

Figure 4.18.: Saturation magnetization M_S for the Fe and Ni layer, derived from magnetometer measurements and time-resolved magnetic hysteresis for different pump-probe delay times (Fig. 4.17).

determine the coefficients for $t < 0$. Moreover, in Chapter 4.2.2, we show, that the spin dynamics in the Fe layer depend on the relative magnetization alignment between the Ni and Fe layers. Therefore, Eq. 4.12-4.13 have to be considered as an approximation.
Knowing a and b and measuring $\Theta_K(H = 0)$ and $\Theta_K(H = H_S)$ in time-dependent magnetic hysteresis loops (Fig. 4.17), the time-resolved magnetization of Fe and Ni was determined (Fig. 4.18) from Eq. 4.12-4.13. On the other hand, the temporal behaviour of H_S itself was traced and found to be constant within the standard deviation (Fig. 4.19). From this finding, and the fact, that the saturation magnetization of both Fe and Ni is transiently quenched, follows, that J_1 changes on the femtosecond timescale (Fig. 4.19). Due to the demagnetization of the Fe and Ni layers, J_1 is reduced by (24 ± 9) %. The transient quenching of J_1 is higher compared to the measurements with high harmonics probe due to the higher pump fluence.
Both experiments show, that the important time-dependent quantity in Eq. 4.9, which dominates the femtosecond dynamics of $J_1(t)$, is $M_{S,Ni}(t)$. At this timescale, the reduction of $M_{S,Ni}$ can be interpreted as a reduction of exchange splitting energy E_{ex} in the Ni layer. In fact, there is experimental evidence for a transient decrease of E_{ex} in thin Ni [193] and Gd [65] films on femtosecond timescale from time-resolved photoemission experiments.

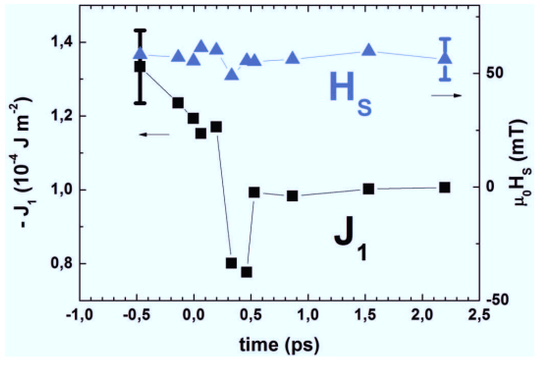

Figure 4.19.: Time-resolved interlayer exchange coupling energy J_1 (black curve) and saturation magnetic field H_S (blue curve) for the Si/SiO_2/Fe(4 nm)/Ru(1 nm)/Ni(5 nm) sample. For convenience, the error bar is displayed for one data point of J_1 and H_S, respectively, but is the same for every data point. Note, that according to the sign convention of Eq. 2.5, $J_1 < 0$ for antiferromagnetic coupling.

In the static case, the connection between the saturation magnetization M_S, and thus E_{ex}, and J_1 was demonstrated by H. Kubota et al. [194], who studied magneto-resistance and interlayer exchange coupling in Ni_xCo_{1-x}/Cu multilayers, and found a $J_1 \sim M_S^2$ scaling. Within the Bruno model of interlayer exchange coupling [48], the spin-dependent reflection coefficient $r_{A,B}^{\uparrow,\downarrow}$ from the layer A or B, for electrons within the spacer layer, also depends on E_{ex}. Thus, a transient decrease of E_{ex} means a decrease of the difference $\Re\left(r_{Ni}^{\uparrow} - r_{Ni}^{\downarrow}\right)$ and, consequently, of J_1.

To the best of our knowledge, laser-induced, femtosecond dynamics of J_1 have not been previously reported in the literature. However, G. Ju et al. observed a transient decrease of the unidirectional exchange bias field H_{EB} in $Ni_{81}Fe_{19}$/NiO bilayers on the femtosecond timescale [195]. Later, F. Dalla Longa et al. reproduced the transient decrease of H_{EB} in Co/IrMn bilayers and measured the characteristic decay time $\tau_{EB} = (0.7 \pm 0.5)$ ps [196]. Both works explain the transient quenching of the exchange bias field due to the ultrafast loss of the spin order in the antiferromagnetic NiO and IrMn after optical pumping.

Finally, one might argue, that all electron spin-dependent interactions like the exchange

interaction, interlayer exchange coupling between ferromagnetic layers and exchange bias can be optically manipulated on the femtosecond timescale.

4.2.2. Laser-Induced Femtosecond Spin Dynamics in Fe/Ru/Ni -Layers

The microscopic picture describing the magnetization dynamics in thin ferromagnetic films is currently under intense debate (Chapter 2.4). Therefore, studies of bi-, tri- and multilayers, comprising ferro- and paramagnetic metals can help to uncover the underlying mechanisms. In particular, the effects of hot electron and spin transport on the femtosecond timescale can be studied in these systems [40, 100, 197–201].
At the end of the 1980s, S. D. Brorson et al. carried out hot electron transport measurements in thin Au films on the femtosecond timescale in a time-of-flight-like experiment. The sample was optically excited through the transparent substrate and probed from the front side of the sample [99]. The time-of-flight is the delay time between the optical excitation at one surface of the sample and the transient change of reflectivity at the opposite side due to hot electron transport. For thin Au films, the time-of-flight amounts to a few hundred femtoseconds and depends linearly on the film thickness [99].
In such a time-of-flight experiment, spin-polarized hot electron transport can be studied by placing a thin ferromagnetic film between the substrate and the Au layer. Recently, A. Melnikov et al. showed by means of time-resolved, optical second harmonic generation, that in epitaxial MgO(001)/Fe(15 nm)/Au(50 nm) samples, the Au surface is transiently magnetized [100]. This finding can be explained by spin-polarized hot electron transport from the Fe to the Au layer.
An other experiment suggesting femtosecond spin transport in laser pump-probe experiments was reported by G. Malinowski et al. [197], showing, that the demagnetization time and amplitude depend on the relative magnetization alignment of Co-Pt-multilayers, being antiferromagnetically coupled through a Ru spacer layer. In the case of electrically insulating NiO spacer, no relative orientation-dependent effects were observed.
In this work, we studied femtosecond magnetization dynamics in metallic layers, namely SiO_2/Ta/Fe/Ru/Ni/Al on Si substrate (Fig. 4.21). The samples were fabricated by J. M. Shaw at NIST in Boulder, USA, by ion beam sputtering, except for the SiO_2/Fe/Ru/Ni samples for time-resolved measurements with visible light (Chapter 4.2.1 and Fig. 4.20), which were prepared at PGI-6, Research Centre Jülich. Time-resolved measurements using high harmonics probe were carried out at JILA, University of Colorado (Boulder), in the group of M. M. Murnane and H. C. Kapteyn. The static magnetic properties are described in Chapter 4.1.1.
Conventional pump-probe measurements with femtosecond lasers employ photon energies below 5 eV, which enable excitations from the valence bands of solids [202]. Being a useful

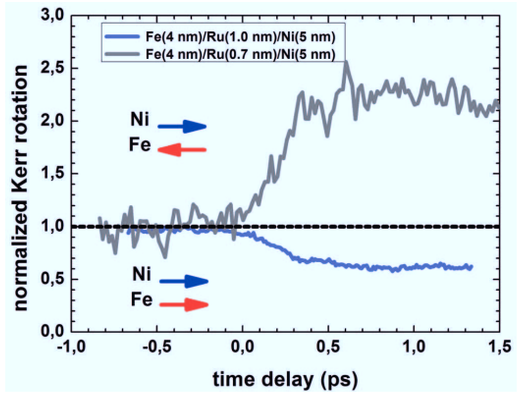

Figure 4.20.: Time-resolved, normalized Kerr rotation (L-MOKE) probed with 3.0 eV light for parallel and antiparallel magnetization alignment of Fe and Ni layers for a Si/SiO_2/Fe(4 nm)/Ru(x)/Ni(5 nm) sample (x=0.7 and 1.0 nm) (after [191]). Note, that the optical pump fluence is different in both cases. The total Kerr rotation comprises the sum of the Kerr rotations for Fe and Ni layers, respectively. Regardless of the relative magnetic orientation, the Ni top layer demagnetizes in both cases, but, for the antiparallel alignment, the total Kerr signal increases due to the reduced screening of the Fe magnetization.

tool for, e.g. probing the band structure effects in spin dynamics [203], the limitations of the technique come to light for samples comprising several layers of different materials. We measured the dynamical response of Si/SiO_2/Fe(4 nm)/Ru(x)/Ni(5 nm) layers (x=0.7 and 1.0 nm) using 1.5 eV pump and 3.0 eV probe pulses in the L-MOKE geometry [191] (Fig. 4.20). Note, that the optical pump fluence is different in both cases. The response for parallel and antiparallel magnetization alignment of the Fe and Ni layers is very different: in the parallel case, the total Kerr rotation transiently decreases to about 60 % of its value before time zero, but, in the antiparallel case, the total Kerr rotation actually increases by a factor of about 2.3. The total, time-dependent Kerr rotation for parallel alignment

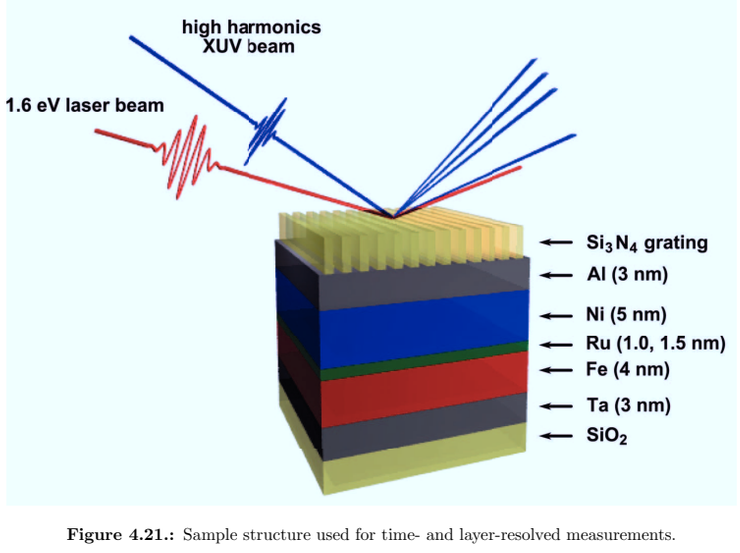

Figure 4.21.: Sample structure used for time- and layer-resolved measurements.

$\theta_{\uparrow\uparrow}(t)$ and antiparallel alignment $\theta_{\uparrow\downarrow}(t)$ can be decomposed into the Kerr rotation $\theta_{Ni}(t)$ from the Ni and $\theta_{Fe}(t)$ from the Fe layer, respectively, and can be written as

$$\theta_{\uparrow\uparrow}(t) = \theta_{Fe}(t) + \theta_{Ni}(t) \tag{4.14}$$

$$\theta_{\uparrow\downarrow}(t) = \theta_{Fe}(t) - \theta_{Ni}(t)\ . \tag{4.15}$$

From Eq. 4.14-4.15 and magneto-optical hysteresis loops similar to the ones displayed in Fig. 4.17 we estimate, that $\theta_{Fe}(t)$ contributes 60 % and $\theta_{Ni}(t)$ contributes 40 % to the total Kerr rotation.

Based on layer-selective measurements with high harmonics probe, which are presented later in this chapter, we assume, first, that the Ni layer is demagnetized for parallel and antiparallel orientation. Second, we assume, that the transient decrease of θ_{Ni} is higher than the transient change of θ_{Fe}. From these assumptions follows, that, for parallel alignment, $\theta_{\uparrow\uparrow}(t)$ decreases after optical excitation, whereas $\theta_{\uparrow\downarrow}(t)$ increases due the reduced screening of the Fe magnetization by the Ni magnetization. If we assume, that $\theta_{Fe}(t < 0) = \theta_{Fe}(t) = \text{const.}$, the experimentally observed increase of $\theta_{\uparrow\downarrow}$ by a factor of

2.3 (Fig. 4.20) means, that the Ni layer is demagnetized by 65 %.
The above described experiment demonstrates the problem of signal superposition from different layers in optical pump-probe measurements, when the net magnetization is probed. Therefore, to gain a deeper insight, it is desirable to probe the magnetization in a layer-selective way.
A solution presented in this work is based on the upconversion of the probe photon energy to more than 72 eV by means of high harmonic generation (Chapter 3.2). The spectral region accessible in our experiments (20 eV-72 eV) covers the 3p shallow core levels of Fe, Co and Ni, fulfilling the resonance condition for a layer-selective magnetic signal (Chapter 4.1.1).
Throughout this chapter, we assume, that the layer-selective T-MOKE asymmetry is proportional to the magnetization of the Fe and Ni layers, respectively, which is a good approximation for the static case (Chapter 3.1). The validity of this assumption has been questioned for optical pump-probe experiments with femtosecond lasers due to effects of state-blocking and non-equilibrium electron distribution [80, 81, 204], which appear as time-dependent, non-magnetic contributions [192]. Non-magnetic artifacts can be addressed experimentally by measuring the reflectivity for two antiparallel magnetization directions and, subsequently, subtracting the signals, as it is usually done in T-MOKE asymmetry measurements. This approach partly removes time-dependent, non-magnetic contributions. Effects of the pump-induced saturation of the final states (state-blocking) and non-equilibrium electron distribution are intrinsic for pump-probe measurements, but they can be reduced, if the pump and probe photon energies differ from each other. For Fe and Ni thin films and the spectral region of interest (20 eV-72 eV), C. La-O-Vorakiat et al. [205] showed, that a pump-induced change of the refractive index would transiently affect the T-MOKE asymmetry by no more than 0.2 %, given, that the non-diagonal element of the dielectric tensor, ϵ_{xy}, is hold constant. Therefore, compared to the measured asymmetry quenching of up to 50 % due to optical pumping, the non-magnetic contribution is negligible. Nevertheless, ϵ_{xy} itself might exhibit pump-induced, non-magnetic contributions.
From the point of view of data treatment, the most reliable analysis of element-selective data can be achieved by integration over the entire absorption edge [204] and we follow this way of data analysis throughout the presented work.
Coming to the results, this chapter focuses on the laser-induced spin transport, being aware, however, that coherent spin-photon interaction and local spin-flip scattering effects might contribute to the magnetization dynamics. For time- and layer-resolved experiments

pump energy density (mJ cm^{-2})	τ_m **(fs)**		τ_r **(ps)**	
	↑↑	↑↓	↑↑	↑↓
1.3	186 ± 45	281 ± 166	4.4 ± 1.4	0.9 ± 0.3
2.0	225 ± 25	208 ± 42	> 100	11.3 ± 6.5
2.7	217 ± 14	146 ± 44	> 100	4.8 ± 2.2

Table 4.1.: De- and remagnetization times τ_m and τ_r, extracted from time-resolved T-MOKE asymmetry at the Ni 3p absorption edge for different energy densities of the pump, for parallel (↑↑) and antiparallel (↑↓) magnetization orientation of the Fe and Ni layers.

on Si/SiO_2/Ta(3 nm)/Fe(4 nm)/Ru(1.5 nm)/Ni(5 nm)/Al(3 nm) layers, we first simulated the absorption of 1.5 eV pump light for every single layer by a self-consistent 2×2 matrix calculation [206]. While the total absorption is 55 %, the Ni and Fe layers absorb each about the same amount of light intensity (29 % of the total absorption in Ni and 24% in Fe), whereas the Al, Ru und Ta layers absorb 27%, 15% and 6% of the total absorption, respectively [207].

For spectroscopic measurements, a Si_3N_4 grating (17.5 nm thickness [180]), which consists of 1 μm thick lines separated by 1 μm distance, is patterned on top of the sample (Chapter 3.3). At first glance, one might expect an inhomogeneous laser excitation through the grating in pump-probe measurements. Si_3N_4 is a wide band-gap dielectric with substantial absorption only above 6 eV [209] and therefore, it is transparent for 1.5 eV pump light. However, at high intensities, which are within reach with femtosecond laser pulses, dielectrics become absorptive by means of multiphoton absorption [210]. To observe multiphoton effects, threshold intensities in the order of 10^{13} W cm^{-2} are required [210], whereas, in our experiment, the pump intensity is two orders of magnitude smaller. Hence, the pump excitation through the Si_3N_4 grating can be safely assumed to be homogeneous.

We fitted the time-resolved magnetic asymmetry $A(t)$ to a double-exponential function

$$A(t) = 1 - \Delta A \left[1 - e^{-(t-t_0)/\tau_m}\right] e^{-(t-t_0)/\tau_r}, \tag{4.16}$$

adopted from [211], where ΔA denotes the quenching amplitude of the magnetic asymmetry, t_0 the offset from the time zero and τ_m and τ_r the de- and remagnetization times. The obtained results are presented in Tab. 4.1. The temporal resolution is estimated to about 25 fs [175], which is limited by the pump laser pulse duration of about 25 fs. Other parameters, which have a significant impact on the temporal resolution, are the

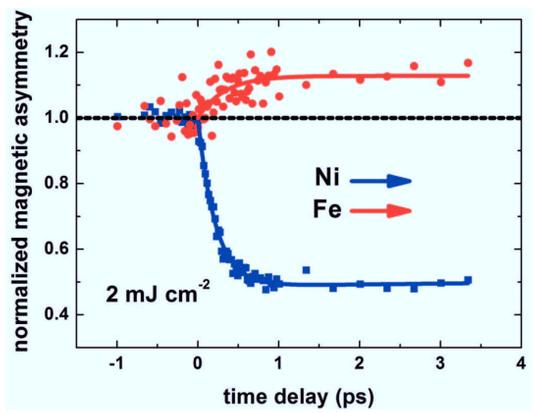

Figure 4.22.: Time- and layer-resolved, normalized magnetic asymmetry for the $Si/SiO_2/Ta(3\ nm)/Fe(4\ nm)/Ru(1.5\ nm)/Ni(5\ nm)/Al(3\ nm)$ sample integrated over the 3p absorption edges of Fe (around 55 eV) and Ni (around 67 eV) for *parallel* magnetization alignment [40]. The excitation energy density is about 2 mJ cm^{-2}. The blue and red curves are fits according to Eq. 4.16.

pulse duration of the probe as well as the angle between the pump and probe beams and thus, the temporal delay between their wavefronts, when they impinge on the sample. In our experiment, the duration of the high harmonics probe pulses is below 10 fs [175] and the angle between the pump and probe beams is close to zero due to their almost collinear propagation.

We analyzed the time-resolved magnetic asymmetry data by integrating over the 3p absorption edges of Ni and Fe and normalizing the magnetic asymmetry to values obtained prior to laser excitation. In our time- and layer-resolved experiments, we varied the energy density (in mJ cm^{-2}) of the pump as well as the relative magnetization alignment of the Ni and Fe layers, which we, for simplicity, call parallel and antiparallel orientation. The experimental findings (Fig. 4.22-4.28) can be summarized as follows.

1. The Ni (top layer) demagnetizes for parallel and antiparallel orientation for each of the optical pump fluences (1.3, 2.0, 2.7 mJ cm^{-2}) employed in the experiment.
2. For all fluences, the spin dynamics in the Fe (bottom layer) depends on the relative magnetization orientation. For 1.3 and 2.0 mJ cm^{-2}, the Fe magnetization is transiently

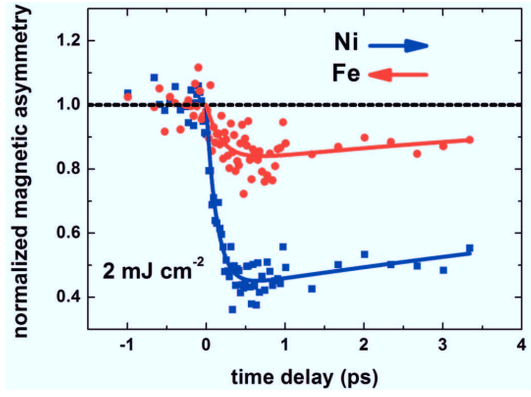

Figure 4.23.: Time- and layer-resolved, normalized magnetic asymmetry for the $Si/SiO_2/Ta(3\ nm)/Fe(4\ nm)/Ru(1.5\ nm)/Ni(5\ nm)/Al(3\ nm)$ sample integrated over the 3p absorption edges of Fe (around 55 eV) and Ni (around 67 eV) for *antiparallel* magnetization alignment [40]. The excitation energy density is about 2 mJ cm^{-2}. The blue and red curves are fits according to Eq. 4.16.

enhanced compared to $t < 0$ for parallel orientation (Fig. 4.22, 4.24, 4.27) and quenched for antiparallel orientation (Fig. 4.23, 4.28). The available data suggest, that the higher the pump fluence, the more pronounced is the enhancement and quenching.

3. For the highest fluence of 2.7 mJ cm^{-2} reached in the experiment, the Fe magnetization is quenched for both parallel and antiparallel orientation (Fig. 4.25, 4.26), albeit, for antiparallel orientation, the quenching is stronger.

4. For all fluences, the remagnetization of Ni is faster for the antiparallel than parallel orientation (Tab. 4.1, Fig. 4.29 for the lowest fluence).

We note, that the transition from 2. to 3. suggests a crossover point, where the Fe magnetization is constant in time. So far, this has not been observed experimentally.

We interpret the transient, orientation-dependent increase or decrease of the Fe magnetization in terms of ultrafast, spin-polarized electron transport [40] applying the superdiffusive spin transport (SST) theory [41, 102]. The calculations presented in this chapter were performed by M. Battiato, P. Maldonado and P. M. Oppeneer from the Uppsala University in Sweden.

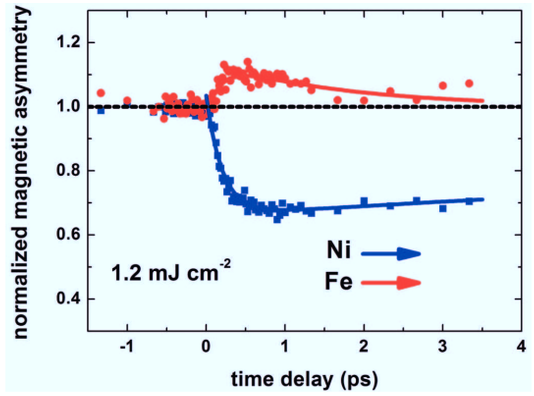

Figure 4.24.: Time- and layer-resolved, normalized magnetic asymmetry for *parallel* magnetization alignment of the Fe and Ni layers [40]. The excitation energy density is about 1.2 mJ cm^{-2}. In contrast to the results of Fig. 4.22 and Fig. 4.23, the thickness of the Ru layer is 1 nm. Only parallel magnetization alignment is possible for this sample due to ferromagnetic interlayer exchange coupling.

Spin- and energy-resolved Two-Photon-Photoemission [38, 212], Magnetic Tunnel Transistor measurements [213] and *ab initio* GW+T calculations [101] provide evidence, that the inelastic mean free path for electrons with energies between E_F and $E_F + 1.5$ eV (1.5 eV is the pump photon energy) is higher for majority electrons than for the minority electrons in both Ni and Fe. The inelastic mean free path is a product of the energy- and spin-dependent lifetime $\tau(\sigma, E)$ and velocity $v(\sigma, E)$, which are the relevant input parameters for the SST calculations (Chapter 2.4.3). If an external voltage was applied on our Fe/Ru/Ni layers, the charge current would be spin-polarized. In case there is no external voltage, like in our optical pump-probe experiments, dielectric screening in metals compensates for any measurable charge flow (e.g. [43, 97, 214]) but not for the spin flow. The majority spin transport out of the probed area is the key idea to understand the measured data. Nevertheless, local spin-flip effects may contribute to the spin dynamics as well.
Furthermore we assume, that the demagnetization due to SST is less efficient in Fe than in Ni [102]. Consequently, after the laser excitation, the net spin current will flow from the Ni to the adjacent Fe layer. For the parallel alignment, the majority spins from Ni are

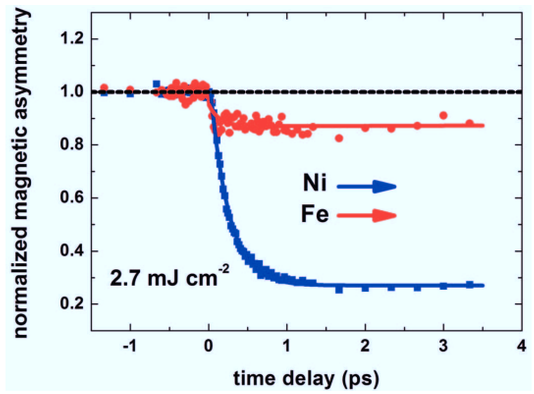

Figure 4.25.: The same sample as in Fig. 4.22 for *parallel* magnetization alignment, but higher excitation energy density of about 2.7 mJ cm^{-2} [40, 208].

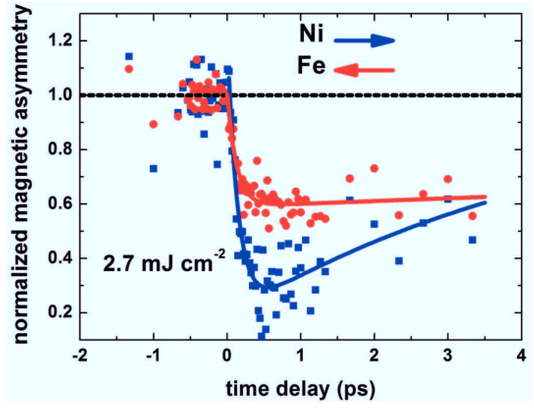

Figure 4.26.: The same sample as in Fig. 4.22 for *antiparallel* magnetization alignment, but higher excitation energy density of about 2.7 mJ cm^{-2} [208].

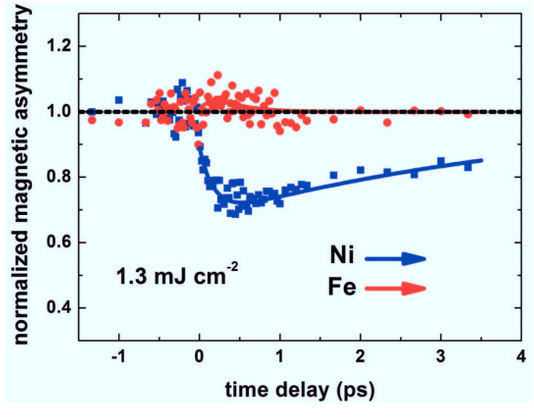

Figure 4.27.: The same sample as in Fig. 4.22 for *parallel* magnetization alignment, but lower excitation energy density of about 1.3 mJ cm^{-2} [40].

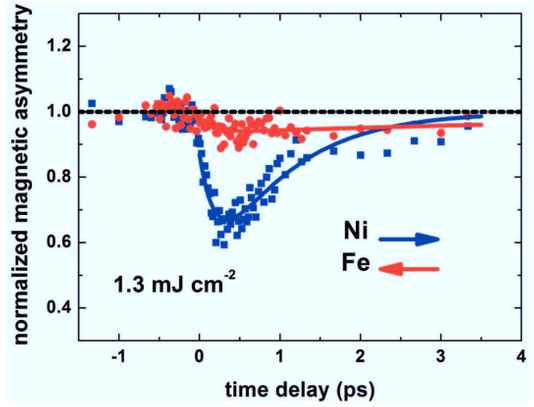

Figure 4.28.: The same sample as in Fig. 4.22 for *antiparallel* magnetization alignment, but lower excitation energy density of about 1.3 mJ cm^{-2}.

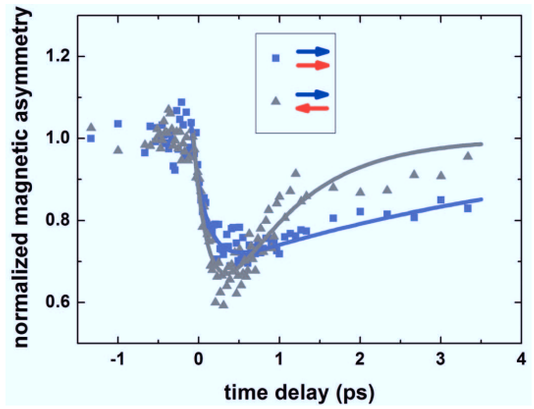

Figure 4.29.: Time-resolved, normalized magnetic asymmetry at the Ni 3p absorption edge for parallel and antiparallel magnetization alignment [40] (combination of data from Fig. 4.27 and 4.28). The blue and grey curves are fits according to Eq. 4.16. Clearly, the remagnetization time τ_r is faster for the antiparallel orientation (grey triangles).

penetrating the Fe layer and filling the empty majority states, thus transiently increasing the Fe magnetization (Fig. 4.30). Contrary to that, for the antiparallel alignment, the Ni majority spins become minority spins in Fe, as soon as they reach the Fe layer. In the latter case, the filling of the Fe minority states results in a transient decrease of the Fe magnetization (Fig. 4.31). The curves in Fig. 4.30 and 4.31 represent spatial averages from Fig. 4.32, where the evolution of the magnetization change ΔM in space and time is displayed. For parallel (a) and antiparallel (b) orientation, the magnetization of Ni is reduced at the interfaces, due to the majority spin transport into the Al and Fe layer. This leads to a transient magnetization of the Al layer, which, in principle, can be proved in the experiment. However, we used an Al filter to block the residual laser light, and therefore, didn't aquire data across the $2p_{1/2}$ and $2p_{3/2}$ absorption edges of Al. For parallel orientation (Fig. 4.32a), the Fe magnetization increases with time ($\Delta M > 0$ and the blue arrow points upwards), whereas in the antiparallel state (Fig. 4.32b), it decreases ($\Delta M > 0$ and the blue arrow points downwards). The majority spins from Ni become minority spins in Fe and thus, are trapped at the Ni-Fe interface. The quantitative agreement

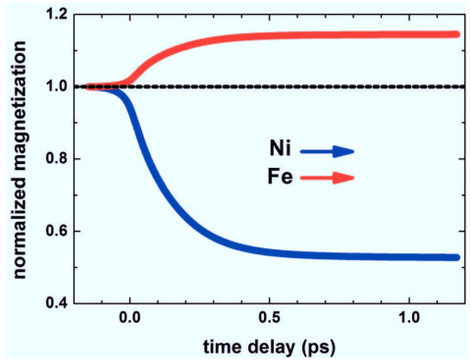

Figure 4.30.: Time- and layer-resolved magnetization, calculated for Fe(4 nm)/Ni(5 nm)/Al(3 nm) layers (Al on the top) from the superdiffusive spin transport theory [40, 215]. For the parallel magnetization alignment of the Ni and Fe layers, the Fe magnetization is transiently enhanced due to majority spin current from the Ni layer.

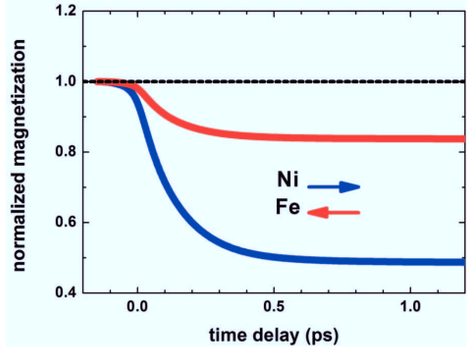

Figure 4.31.: Time- and layer-resolved magnetization, calculated for Fe(4 nm)/Ni(5 nm)/Al(3 nm) layers (Al on the top) from the superdiffusive spin transport theory [40, 215]. For the antiparallel magnetization alignment, the Ni majority spins become minority spins in Fe, as soon as they reach the Fe layer. Hence, the Fe magnetization is transiently decreased.

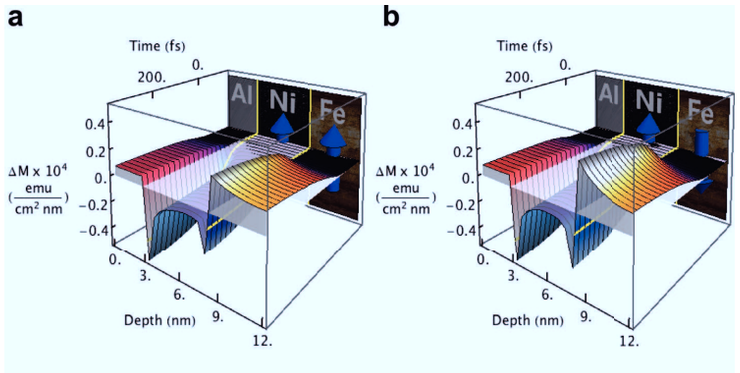

Figure 4.32.: Evolution of the Al/Ni/Fe magnetization in space and time [40, 215]. The magnetization change ΔM compared to the case of thermal equilibrium is displayed for the parallel (a) and antiparallel (b) orientation of the Ni and Fe magnetization within the first 500 fs after the laser excitation along the depth profile of the layers. The Ni spin-majority electrons move by superdiffusion, predominantly from the interface region, into the Fe and Al layers, thus decreasing the Ni magnetization.

between the experiment for 2 mJ cm^{-2} fluence (about 50 % demagnetization of Ni, 10-20 % magnetization decrease and increase in Fe) and the theory (45 % demagnetization of Ni, 15 % magnetization decrease and increase in Fe) is very good. However, the present version of the SST model doesn't account for the remagnetization process, which starts about 500 fs after the laser excitation. Moreover, in the calculations, the 1.5 nm Ru layer and 3 nm Ta layer are neglected, assuming, that they have no significant effect on the spin transport from the Ni to the Fe layer. Nevertheless, Ta and Ru have many d states for $E_F < E < E_F + 1.5$ eV and, consequently, rather poor transport properties for excited electrons [199]. Therefore, the spin current from the Ni to the Fe layer is expected to be reduced by the Ru layer. In addition, the spin diffusion length in Ta is known to be small [216], which can be attributed to the large spin-orbit coupling. Hence, Ta may act as a spin sink, trapping the spins emitted from other metallic layers.
On the other hand, the Al layer, which is included in the calculations, enhances the spin current for two reasons. First, the electrons excited in Al are spin-filtered in Ni as they pass the Ni layer and second, they can excite electrons in Ni by inelastic electron-electron

scattering.

We note, that the energy- and spin-dependent velocities $v(\sigma, E)$ and lifetimes $\tau(\sigma, E)$ for Al, Ni and Fe were taken from *ab initio* GW+T calculations [101], which predict a lifetime spin asymmetry $\tau^{\uparrow}/\tau^{\downarrow}$ of about 6 for $E = E_F + 1$ eV in Ni, whereas a spin asymmetry of 1.5 was measured with Two-Photon-Photoemission [38]. Nevertheless, the calculated electron inelastic mean free path from [101] agrees well with the data from Magnetic Tunnel Transistor measurements [213]. In addition, it is not completely clear yet, if and how the velocities and lifetimes can be changed in a highly excited electronic state compared to the case of thermal equilibrium.

The results from SST theory compare well with experimental data for a laser fluence of about 2 mJ cm^{-2} (Fig. 4.22, 4.23) and below (Fig. 4.27, 4.28). For a higher fluence, even a higher increase of the Fe magnetization above its thermal equilibrium value is expected for the parallel orientation assuming only superdiffusive spin transport. Contrary to that, a transient quenching of the Fe magnetization is observed for parallel as well as for antiparallel alignment. First, this implies a saturation of the SST, because the linear scaling with the pump fluence vanishes. Second, this is an evidence for the competition between SST and local demagnetization processes like electron-phonon or electron-magnon spin-flip scattering [200].

There are two different interpretations of transient, orientation-dependent increase or decrease of the Fe magnetization, which need to be addressed as well. First, one may argue, that the laser pulse increases the exchange energy in Fe, which leads to enhanced ferromagnetic ordering and increase in the T-MOKE signal. Indeed, such an effect was observed in semiconducting EuO [217] and GaMnAs [218]. In EuO, it was attributed to photoinjection of the 4f electrons into 5d bands and a subsequent reorganization of the 4f states. In GaMnAs, the authors proposed ferromagnetic ordering due to the p-d exchange interaction between photoexcited holes and Mn spins. However, a transient, laser-induced increase of the MOKE signal has never been observed in Fe films [94, 192]. Moreover, the magnetization orientation dependence cannot be explained in this picture.

Second, one can ask, what happens, if the laser pulse modifies the antiferromagnetic interlayer exchange coupling (AF-IEC). Given, the AF-IEC is transiently quenched, as indeed observed in experiments (Chapter 4.2.1), it would affect the measurements for the antiparallel orientation, for which the correct range of the external magnetic fields has to be chosen carefully. On the other hand, the measurements for parallel orientation, when the magnetization of Fe and Ni is saturated in the external field, will not be affected. For antiparallel orientation, a transient decrease of AF-IEC would change the amplitude

and direction of the effective magnetic field H_{eff}. Consequently, Fe and Ni magnetization would perform a damped oscillation around the new H_{eff} and, finally, align with it. The described dynamics predicted by the Landau-Lifshitz-Gilbert equation takes place on the pico- to nanosecond timescale. Hence, our experimental findings cannot be explained by the laser-induced change of AF-IEC. The role of AF-IEC in our experiments is to prepare a well-defined parallel or antiparallel orientation.

An other experimental result is the spin-dependence of the remagnetization time of Ni, being faster for the antiparallel than for the parallel alignment (Fig. 4.29, Tab. 4.1). In close analogy to the Giant Magneto-Resistance (GMR) effect, one possible explanation would be, that in the antiparallel case, the Ni majority electrons, reaching the Fe layer, undergo more scattering events than in the parallel case, forcing them to return back to the Ni layer faster. Again, not only transport but also local spin-flip dynamics contribute to the remagnetization. However, more theoretical investigations are required, which are beyond the scope of this work.

Lastly, we compare superdiffusive spin transport (SST) in Fe/Ru/Ni layers with the effect of spin-transfer torque (STT) [219], which was e.g. observed in lithografically patterned Co/Cu/Co layers [220]. In STT devices, one ferromagnetic layer is used to spin-polarize the applied current density, whereas the transversal component of the spin relative to the magnetization of the second ferromagnetic layer is transferred to the magnetization of the second ferromagnet. In our experiments, the optically generated spin current density moving from the Ni to the Fe layer is not accompanied by charge current. The magnetization of Fe is enhanced for the parallel alignment due to transient filling of available spin majority states above the Fermi energy in the Fe layer. Thus, the longitudinal component of the spin is absorbed in Fe. From about 10% transient enhancement of the Fe magnetization (Fig. 4.22) within few hundred femtoseconds and from the known beam diameter of the pump laser beam and the thickness of the Fe layer, a spin flux in the order of 10^{32} spins $\mathrm{m}^{-2}\ \mathrm{s}^{-1}$ was estimated. In the case of completely spin-polarized charge current, the order of magnitude of the spin flux, which is required to observe STT, can be estimated from the threshold current density of 10^7 A m^{-2} to be 10^7 A $\mathrm{m}^{-2}/e \approx 6 \cdot 10^{25}$ spins $\mathrm{m}^{-2}\ \mathrm{s}^{-1}$, where e denotes the elementary charge. Consequently, the spin current density observed in our experiment is 6 order of magnitude larger than the spin current density, which is required for STT. Thus, in properly designed samples, SST can be possibly used to optically reverse the magnetization. The enormous difference in the spin current density is due to the timescale of SST of few hundred femtoseconds. Contrary to that, the magnetization dynamics induced by STT evolves rather on the picosecond to nanosecond timescale [221].

To summarize this chapter, in Si/SiO_2/Ta(3 nm)/Fe(4 nm)/Ru(x)/Ni(5 nm)/Al(3 nm) samples, x=1.0 and 1.5 nm, we found evidence for spin transport on the femtosecond timescale, predominantly from the Ni to the Fe layer. Depending on the relative magnetization alignment, the spin transport from Ni can either transiently decrease (antiparallel alignment) or increase (parallel alignment) the Fe magnetization within a certain laser fluence window. The experimental data can be very well reproduced by calculations from the superdiffusive spin transport theory. For the highest fluence reached in the experiments, no transient magnetization enhancement in Fe is observed. Nevertheless, the quenching of the Fe magnetization is smaller for the parallel than for the antiparallel alignment. In addition, we found the remagnetization time of Ni to be magnetization orientation-dependent.

5. Summary and Outlook

In summary, we explored laser-induced, femtosecond spin dynamics in ferromagnetic layered structures. As a model system, we focused on interlayer exchange coupled Fe/Ru/Ni layers. We conducted time- and layer-resolved, magneto-optical measurements at the 3p absorption edges of Fe (54 eV) and Ni (67 eV) in the transversal magneto-optical Kerr effect (T-MOKE) geometry. We probed the magnetization using sub-10 fs pulses of laser high harmonics (15-72 eV) generated in Ne gas.

Initially, static, layer-selective and temperature-dependent magnetization reversal of the Fe and Ni layers was traced and the interlayer exchange coupling energy J_1 was derived for antiferromagnetically coupled Fe and Ni layers from magnetometer measurements. In the next step, we studied femtosecond dynamics of J_1 in pump-probe experiments with 1.5 eV optical pump and either 3.0 eV or high harmonics probe. In time-resolved measurements of magnetic hysteresis, we observed, that J_1 was transiently quenched on the femtosecond timescale due to optical pumping by the femtosecond laser, following the demagnetization of the Ni layer. To investigate the spin dynamics in more detail, we carried out time- and layer-resolved measurements for parallel and antiparallel magnetization orientation of the Fe and Ni layers and for various pump fluences. The central and surprising result of our studies is, that the (bottom) Fe layer is transiently magnetized *above* its equilibrium magnetization prior to laser excitation *for parallel orientation* and demagnetized *for antiparallel orientation* for a certain pump fluence range. For the highest fluence reached in the experiment, the Fe magnetization is quenched for both parallel and antiparallel orientation, albeit, for antiparallel orientation, the quenching is higher. Regardless of the relative orientation and pump fluence, the Ni layer is always demagnetized. The magnetization orientation-dependent spin dynamics in the Fe layer (magnetization for parallel, demagnetization for antiparallel orientation) is interpreted as a consequence of superdiffusive spin transport (SST) from the Ni to the Fe layer and corroborated by calculations based on SST, which agree well with experimental data within a certain fluence range.

Does a spin transport also occur from the Fe to the Ni layer if the position of the Fe and Ni layers are exchanged in the layer stack? This question was recently addressed by E.

Turgut et al. [200], who found magnetization orientation dependent spin dynamics in the buried Ni layer, i.e. higher demagnetization for antiparallel than for the parallel alignment. In this case, no enhancement of the Ni magnetization for the parallel orientation was observed.

Our work on the Fe/Ru/Ni layers provides evidence for laser-induced spin transport, but what are the remaining challenges to completely understand laser-induced, femtosecond spin dynamics in ferromagnets? First, a clear picture of the dynamics of the spin-orbit coupling and exchange interaction under non-equilibrium conditions as well as the consequences for the band structure is required. Transient changes of the band structure cannot be excluded a priori. To study the dynamics of exchange interaction is essential for multisublattice materials, e.g. NiFe or GdFeCo alloys. Second, in pump-probe experiments, the occurrence of magneto-optical artifacts due to non-equilibrium electron distribution right after the excitation has to be analyzed. Third, the relative importance and magnitude of different proposed microscopic mechanisms, which involve spin-flips, such as spin-photon, electron-electron, electron-phonon and electron-magnon interaction, needs to be critically addressed (see Chapter 2.4). Possibly, in different materials different mechanisms become more prominent than others.

Recently, some evidence for spin transport on the femtosecond timescale has been found by different research groups in multilayer samples [40, 100, 197–201]. Up to now, extended layers have been fabricated, where the spin transport occurs in all three spatial dimensions. In the next step, the spin current can be confined in one direction in specially designed nanostructures. Furthermore, the velocities and lifetimes of hot electrons between two ferromagnetic layers can be tuned by the choice of the spacer layer. Metals like Au and Cu with s states above the Fermi energy are expected to be good spin conductors, which is not the case for the early 3d metals like Ti or V. The metallic spacer layer can be also replaced by a thin insulator layer, e.g. MgO, to study spin tunneling effects.

Finally, the development of scientific instruments and techniques is expected to enable new exciting results. Time- and element-resolved magnetic imaging on the femtosecond timescale with nanometer lateral resolution is within reach due to the fast improvement of free electron lasers and high harmonic light sources. The progress in the attosecond physics will potentially enable studies of laser-induced spin dynamics on the attosecond timescale. The journey has just begun.

A. Appendix

In this appendix, a selection of different physical effects related to manipulation of magnetization of ferro-, ferri- and antiferromagnets with femtosecond laser pulses and their interpretation is given. The motivation is to provide an overview and collection of references for interested readers. In spite of the diversity of physical effects and materials, we made an attempt to order the table as far as possible (e.g. timescales of demagnetization, magnetic phase transitions, transport effects).

Physical Effect	**Interpretation**
subpicosecond demagnetization of metallic, ferromagnetic films of Fe [94, 192], Co [74, 93], Ni [39, 74, 222, 223], $Ni_{80}Fe_{20}$ [37, 175], $CoPt_3$ [211], etc.	**Phenomenological view** Three-Temperature-Model [39] **Multiscale approach** combining Spin Density Functional Theory, atomistic spin models, Landau-Lifshitz-Gilbert-, Landau-Lifshitz-Bloch-Equations and Two(Three)-Temperature-Model [20, 58, 64, 67, 72, 73] **Microscopic view** interplay between the laser electric field and spin-orbit-coupling [224], coherent spin-photon coupling [82, 83], electron-magnon interaction [94, 96], transfer of the spin angular momentum to the lattice in spin-flip electron-electron and electron-phonon scattering [66, 74, 225, 226], superdiffusive spin transport [41, 102]

Time scale of demagnetization: below 1 ps for 3d metals Fe, Co, Ni, several ps to tenths of ps for 4f metals Gd and Tb [227], hundreds of ps for ferromagnetic half-metals [228] and dielectrics [229, 230]	Microscopic Three-Temperature-Model (Type I and II dynamics) [74, 226] reduced spin-flip probability [228], lattice heating and subsequent magnon excitation via spin-lattice interaction [228, 229]
different dynamics of the Kerr rotation and ellipticity for $t < 500$ fs in Cu/Ni/Cu samples [80] and real and imaginary part of $\Delta\epsilon_{xy}/\epsilon_{xy}$ for $t < 150$ fs in $CoPt_3$ films [211]	laser-induced state-blocking of optical transitions [80] due to non-equilibrium electron distribution [81]
partial loss of exchange splitting in Ni [193] and Gd [65] films, immediate response of the valence bands minority electrons in Gd films to the laser excitation, delayed response of the majority electrons [65]	energy transfer between hot electrons, Stoner pairs, magnons and phonons [193] spin-flips of the valence bands majority electrons induce spin-flips of the 4f majority electrons via exchange interaction, magnon emission [65]
THz emission from Ni and Fe films [231, 232]	magnetic dipole radiation due to ultrafast demagnetization [231]
quenching of the orbital and spin angular momentum $L_z(t)$ and $S_z(t)$ in a CoPd alloy on the timescale of few hundreds fs, $L_z(t)$ quenches faster than $S_z(t)$ [233]	transient change of the spin-orbit coupling, which quenches the perpendicular magnetic anisotropy [233]
transient increase of spin-orbit interaction in Ni films [234]	accumulation of electrons in the regions of the Brillouin zone with strong spin-orbit coupling (hot spots) and subsequent spin-flips [234]
spin dynamics in Cu doped $Ni_{80}Fe_{20}$: initial demagnetization of the Fe sublattice 76 fs prior to the demagnetization of the Ni sublattice [175]	laser-induced demagnetization of the Fe sublattice, Ni sublattice is demagnetized indirectly by exchange interaction after the characteristic delay time [175]
laser-induced magnetization reversal in ferrimagnetic GdFeCo within about 700 fs in an external magnetic field [235]	subpicosecond timescale: laser-induced heating above the angular momentum compensation temperature T_A, at T_A, the spin precession frequency and domain wall velocity are highly accelerated [235]
optical magnetization reversal in ferrimagnetic GdFeCo [236] and TbCo [237] films with circulary polarized, fs and ps laser pulses	combined action of heating of the spin system and Inverse Faraday effect [236]

pump helicity-dependent excitation of spin oscillations in antiferromagnetic, dielectric $DyFeO_3$ [238] and ferrimagnetic, metallic GdFeCo [50]	generation of ultrashort magnetic field pulses via Inverse Faraday effect
quenching of the exchange bias magnetic field in ferromagnetic/antiferromagnetic NiFe/NiO [195] and Co/IrMn [196] films on the fs timescale	loss of spin order in the antiferromagnet by laser heating [195, 196]
transient enhancement of the magnetization in EuO films within few ps [217] and in GaMnAs films on the timescale of several hundreds of ps [218], highest, transient increase of the magnetization close to the Curie temperature of about 80 K [218]	spin polarization of the photoexcited 5d electrons and enhancement of the 4f-5d exchange interaction [217] photoexcited holes enhance the Mn-Mn exchange interaction [218]
optically induced spin precession in (Ga,Mn)As films on PZT piezostressor using circularly polarized light with photon energies above the band gap [239]	optical spin transfer torque [239]
Magnetic phase transitions: ferromagnetic to paramagnetic phase in $CoPt_3$ [240] antiferromagnetic to ferromagnetic phase in $Fe_{45}Rh_{55}$ [241–244] transient ferromagnetic state in ferrimagnetic GdFeCo [68] **Spin reorientation:** $TmFeO_3$ [245] (Ga,Mn)As [246]	ultrafast heating above the Curie temperature within the thermalization time of the electrons to the Fermi-Dirac distribution [240] non-equilibrium ferromagnetic state [241, 242] lattice expansion [243, 244] different dynamics of Gd and FeCo sublattices [68] sub-ps change of the anisotropy axis [245]

Transport of charge and spin carriers: spin dynamics in interlayer exchange coupled $[Co/Pt]_n/X/[Co/Pt]_n$ (X=Ru, NiO) layers: magnetization orientation-dependent demagnetization time for the Ru (faster for antiparallel than for parallel alignment), but not for the NiO interlayer, stronger demagnetization for the antiparallel state [197]	
transient spin-polarization of the Au surface in a Au/Fe/MgO(001) sample by excitation of spin-polarized, hot carriers in the Fe layer [100]	transfer of spin angular momentum by spin transport [197]
spin dynamics in interlayer exchange coupled Ni/Ru/Fe layers: enhancement of the Fe magnetization (bottom layer) for parallel magnetization alignment of the Ni and Fe layers, quenching for the antiparallel alignment, Ni demagnetizes in both cases [40]	competition between diffusive and ballistic spin transport [100]
magnetic small angle scattering on Co/Pt multilayers: transient decrease of the linear momentum transfer by 4%, quenching of the magnetization [198]	superdiffusive spin transport [40]
distinct THz emission from Au/Fe and Ru/Fe films [199]	softening of the domain wall boundaries due to spin transport [198]
spin dynamics in Ni/X/Fe (X=Ru, Ta, W, Si_3N_4) layers: for parallel magnetization alignment of Ni and Fe layers, transient increase (Ru interlayer) and decrease (Ta, W, Si_3N_4 interlayers) of the Fe magnetization [200]	generation of spin current pulses in the Fe layer, conversion into charge current pulses by Inverse Spin Hall effect, emission of THz radiation [199]
	interplay between local processes (spin-flip scattering) and non-local spin transport [200]

demagnetization of the buried Ni layer in a Au(30 nm)/Ni(15 nm) structure without a direct optical excitation of the Ni layer [201]	hot electron and spin transport [201]

Table A.1.: Selection of different physical effects related to manipulation of magnetization of ferro-, ferri- and antiferromagnets with femtosecond laser pulses and their interpretation.

Bibliography

[1] J. Bardeen and W. H. Brattain, "The Transistor, A Semi-Conductor Triode", *Phys. Rev.* **74**, 230 (1948). 1

[2] C. Chappert, A. Fert, and F. N. Van Dau, "The emergence of spin electronics in data storage", *Nat Mater* **6(11)**, 813 (2007). 1, 2

[3] G. Binasch, P. Grünberg, F. Saurenbach, and W. Zinn, "Enhanced magnetoresistance in layered magnetic structures with antiferromagnetic interlayer exchange", *Phys. Rev. B* **39**, 4828 (1989). 1

[4] M. N. Baibich, J. M. Broto, A. Fert, F. N. Van Dau, F. Petroff, P. Etienne, G. Creuzet, A. Friederich, and J. Chazelas, "Giant Magnetoresistance of (001)Fe/(001)Cr Magnetic Superlattices", *Phys. Rev. Lett.* **61**, 2472 (1988). 1

[5] S. Bader and S. Parkin, "Spintronics", *Annual Review of Condensed Matter Physics* **1(1)**, 71 (2010). 1

[6] J. Slonczewski, "Current-driven excitation of magnetic multilayers", *Journal of Magnetism and Magnetic Materials* **159**, L1 (1996). 1

[7] L. Berger, "Emission of spin waves by a magnetic multilayer traversed by a current", *Phys. Rev. B* **54**, 9353 (1996). 1

[8] F. J. Albert, J. A. Katine, R. A. Buhrman, and D. C. Ralph, "Spin-polarized current switching of a Co thin film nanomagnet", *Applied Physics Letters* **77(23)**, 3809 (2000). 1

[9] M. Dyakonov and V. Perel, "Current-induced spin orientation of electrons in semiconductors", *Physics Letters A* **35(6)**, 459 (1971). 1

[10] Y. K. Kato, R. C. Myers, A. C. Gossard, and D. D. Awschalom, "Observation of the Spin Hall Effect in Semiconductors", *Science* **306(5703)**, 1910 (2004). 1

[11] E. M. Hankiewicz, J. Li, T. Jungwirth, Q. Niu, S.-Q. Shen, and J. Sinova, "Charge Hall effect driven by spin-dependent chemical potential gradients and Onsager relations in mesoscopic systems", *Phys. Rev. B* **72**, 155305 (2005). 1

[12] E. Saitoh, M. Ueda, H. Miyajima, and G. Tatara, "Conversion of spin current into charge current at room temperature: Inverse spin-Hall effect", *Applied Physics Letters* **88(18)**, 182509 (2006). 1

[13] K. Uchida, S. Takahashi, K. Harii, J. Ieda, W. Koshibae, K. Ando, S. Maekawa, and E. Saitoh, "Observation of the spin Seebeck effect", *Nature* **455(7214)**, 778 (2008). 1

[14] http://www.nve.com/index.php (2013). 2

[15] R. Jansen, "The spin-valve transistor: a review and outlook", *Journal of Physics D: Applied Physics* **36(19)**, R289 (2003). 2

[16] W. C. Black and B. Das, "Programmable logic using giant-magnetoresistance and spin-dependent tunneling devices (invited)", *Journal of Applied Physics* **87(9)**, 6674 (2000). 2

[17] D. A. Allwood, G. Xiong, C. C. Faulkner, D. Atkinson, D. Petit, and R. P. Cowburn, "Magnetic Domain-Wall Logic", *Science* **309(5741)**, 1688 (2005). 2

[18] A. Moser, K. Takano, D. T. Margulies, M. Albrecht, Y. Sonobe, Y. Ikeda, S. Sun, and E. E. Fullerton, "Magnetic recording: advancing into the future", *Journal of Physics D: Applied Physics* **35(19)**, R157 (2002). 2

[19] S. S. P. Parkin, M. Hayashi, and L. Thomas, "Magnetic Domain-Wall Racetrack Memory", *Science* **320(5873)**, 190 (2008). 2

[20] K. Vahaplar, A. M. Kalashnikova, A. V. Kimel, D. Hinzke, U. Nowak, R. Chantrell, A. Tsukamoto, A. Itoh, A. Kirilyuk, and T. Rasing, "Ultrafast Path for Optical Magnetization Reversal via a Strongly Nonequilibrium State", *Phys. Rev. Lett.* **103**, 117201 (2009). 2, 14, 87

[21] T. Ostler, J. Barker, R. Evans, R. Chantrell, U. Atxitia, O. Chubykalo-Fesenko, S. El Moussaoui, L. Le Guyader, E. Mengotti, L. Heyderman, F. Nolting, A. Tsukamoto, A. Itoh, D. Afanasiev, B. Ivanov, A. Kalashnikova, K. Vahaplar, J. Mentink, A. Kirilyuk, T. Rasing, and A. Kimel, "Ultrafast heating as a sufficient

stimulus for magnetization reversal in a ferrimagnet", *Nat Commun* **3**, 666 (2012). 2, 14

[22] J. Stöhr and H. Siegmann, *Magnetism. From Fundamentals to Nanoscale Dynamics*, (Springer 2006). 2, 5, 6, 7, 8, 31, 33

[23] T. H. Maiman, "Stimulated Optical Radiation in Ruby", *Nature* **187(4736)**, 493 (1960). 2

[24] D. E. Spence, P. N. Kean, and W. Sibbett, "60-fsec pulse generation from a self-mode-locked Ti:sapphire laser", *Opt. Lett.* **16(1)**, 42 (1991). 2

[25] A. McPherson, G. Gibson, H. Jara, U. Johann, T. S. Luk, I. A. McIntyre, K. Boyer, and C. K. Rhodes, "Studies of multiphoton production of vacuum-ultraviolet radiation in the rare gases", *J. Opt. Soc. Am. B* **4(4)**, 595 (1987). 2, 36

[26] M. Ferray, A. L'Huillier, X. F. Li, L. A. Lompre, G. Mainfray, and C. Manus, "Multiple-harmonic conversion of 1064 nm radiation in rare gases", *Journal of Physics B: Atomic, Molecular and Optical Physics* **21(3)**, L31 (1988). 2, 36

[27] M. Lewenstein, P. Balcou, M. Y. Ivanov, A. L'Huillier, and P. B. Corkum, "Theory of high-harmonic generation by low-frequency laser fields", *Phys. Rev. A* **49**, 2117 (1994). 2, 37, 38

[28] T. Brabec and F. Krausz, "Intense few-cycle laser fields: Frontiers of nonlinear optics", *Rev. Mod. Phys.* **72**, 545 (2000). 2

[29] H. C. Kapteyn, M. M. Murnane, and I. P. Christov, "Extreme Nonlinear Optics: Coherent X Rays from Lasers", *Physics Today* **58(3)**, 39 (2005). 2

[30] F. Krausz and M. Ivanov, "Attosecond physics", *Rev. Mod. Phys.* **81**, 163 (2009). 2

[31] T. Popmintchev, M.-C. Chen, D. Popmintchev, P. Arpin, S. Brown, S. Ališauskas, G. Andriukaitis, T. Balčiunas, O. D. Mücke, A. Pugzlys, A. Baltuška, B. Shim, S. E. Schrauth, A. Gaeta, C. Hernández-García, L. Plaja, A. Becker, A. Jaron-Becker, M. M. Murnane, and H. C. Kapteyn, "Bright Coherent Ultrahigh Harmonics in the keV X-ray Regime from Mid-Infrared Femtosecond Lasers", *Science* **336(6086)**, 1287 (2012). 2, 36, 39, 40

[32] T. Koide, T. Shidara, H. Fukutani, K. Yamaguchi, A. Fujimori, and S. Kimura, "Strong magnetic circular dichroism at the $M_{2,3}$ edges in ferromagnetic Ni and ferrimagnetic Fe_3O_4", *Phys. Rev. B* **44**, 4697 (1991). 3, 31, 32

[33] H. Höchst, D. Rioux, D. Zhao, and D. L. Huber, "Magnetic linear dichroism effects in reflection spectroscopy: A case study at the Fe $M_{2,3}$ edge", *Journal of Applied Physics* **81(11)**, 7584 (1997). 34

[34] M. Pretorius, J. Friedrich, A. Ranck, M. Schroeder, J. Voss, V. Wedemeier, D. Spanke, D. Knabben, I. Rozhko, H. Ohldag, F. U. Hillebrecht, and E. Kisker, "Transverse magneto-optical Kerr effect of Fe at the Fe 3p threshold", *Phys. Rev. B* **55**, 14133 (1997). 34

[35] S. Valencia, A. Gaupp, W. Gudat, H.-C. Mertins, P. M. Oppeneer, D. Abramsohn, and C. M. Schneider, "Faraday rotation spectra at shallow core levels: 3p edges of Fe, Co and Ni", *New Journal of Physics* **8**, 254 (2006). 34, 35

[36] P. Grychtol, R. Adam, S. Valencia, S. Cramm, D. E. Bürgler, and C. M. Schneider, "Resonant magnetic reflectivity in the extreme ultraviolet spectral range: Interlayer-coupled Co/Si/Ni/Fe multilayer system", *Phys. Rev. B* **82**, 054433 (2010). 3, 31, 34

[37] C. La-O-Vorakiat, M. Siemens, M. M. Murnane, H. C. Kapteyn, S. Mathias, M. Aeschlimann, P. Grychtol, R. Adam, C. M. Schneider, J. M. Shaw, H. T. Nembach, and T. J. Silva, "Ultrafast Soft X-Ray Magneto-Optics at the M-edge Using a Tabletop High-Harmonic Source", *Phys. Rev. Lett.* **103**, 257402 (2009). 3, 87

[38] R. Knorren, K. H. Bennemann, R. Burgermeister, and M. Aeschlimann, "Dynamics of excited electrons in copper and ferromagnetic transition metals: Theory and experiment", *Phys. Rev. B* **61**, 9427 (2000). 3, 17, 20, 21, 76, 82

[39] E. Beaurepaire, J.-C. Merle, A. Daunois, and J.-Y. Bigot, "Ultrafast Spin Dynamics in Ferromagnetic Nickel", *Phys. Rev. Lett.* **76**, 4250 (1996). 3, 10, 11, 12, 13, 87

[40] D. Rudolf, C. La-O-Vorakiat, M. Battiato, R. Adam, J. M. Shaw, E. Turgut, P. Maldonado, S. Mathias, P. Grychtol, H. T. Nembach, T. J. Silva, M. Aeschlimann, H. C. Kapteyn, M. M. Murnane, C. M. Schneider, and P. M. Oppeneer, "Ultrafast magnetization enhancement in metallic multilayers driven by superdiffusive spin current", *Nat Commun* **3**, 1037 (2012). 3, 69, 74, 75, 76, 77, 78, 79, 80, 81, 86, 90

[41] M. Battiato, K. Carva, and P. M. Oppeneer, "Superdiffusive Spin Transport as a Mechanism of Ultrafast Demagnetization", *Phys. Rev. Lett.* **105**, 027203 (2010). 4, 21, 75, 87

[42] R. Skomski, *Simple Models of Magnetism*, (Oxford University Press 2008). 5, 6, 9

[43] N. W. Ashcroft and N. D. Mermin, *Solid State Physics*, (Saunders College Publishing 1976). 5, 20, 76

[44] H. Ibach and H. Lüth, *Solid-State Physics*, (Springer 2009). 5, 6, 7, 11

[45] P. Mohn, *Magnetism in the Solid State*, (Springer 2006). 6, 7

[46] D. E. Bürgler, P. Grünberg, S. O. Demokritov, and M. T. Johnson, "Interlayer Exchange Coupling in Layered Magnetic Structures", vol. 13 of *Handbook of Magnetic Materials*, 1 – 85, (Elsevier 2001). 7, 8, 57

[47] S. S. P. Parkin, N. More, and K. P. Roche, "Oscillations in exchange coupling and magnetoresistance in metallic superlattice structures: Co/Ru, Co/Cr, and Fe/Cr", *Phys. Rev. Lett.* **64**, 2304 (1990). 8, 59

[48] P. Bruno, "Theory of interlayer magnetic coupling", *Phys. Rev. B* **52**, 411 (1995). 8, 60, 67

[49] D. J. Craik and M. J. Wood, "Thermally Activated Domain Wall Movement", *physica status solidi (b)* **16(1)**, 321 (1966). 8

[50] A. Kirilyuk, A. V. Kimel, and T. Rasing, "Ultrafast optical manipulation of magnetic order", *Rev. Mod. Phys.* **82**, 2731 (2010). 8, 9, 16, 89

[51] R. Hertel, "Micromagnetism", in "Spintronics-From GMR to Quantum Information", Lecture Notes of the 40th Spring School, (Forschungszentrum Jülich GmbH 2009). 9

[52] T. Gilbert, "A phenomenological theory of damping in ferromagnetic materials", *Magnetics, IEEE Transactions on* **40(6)**, 3443 (2004). 9, 14

[53] R. Hertel and J. Kirschner, "Resonant modes of vortex structures in soft-magnetic nanodiscs", *Journal of Magnetism and Magnetic Materials* **272-276, Part 1(0)**, 655 (2004). 9

[54] M. B. Agranat, S. I. Ashkitov, A. B. Granovskij, and G. I. Rukman, "Interaction of picosecond laser pulses with the electron, spin and phonon subsystems of nickel", *Zh. Eksp. Teor. Fiz.* **86**, 1376 (1984). 10

[55] G. L. Bona, F. Meier, G. Schönhense, M. Aeschlimann, M. Stampanoni, G. Zampieri, and H. C. Siegmann, "Spin-polarized photoemission from iron by pulsed laser radiation", *Phys. Rev. B* **34**, 7784 (1986). 10

[56] A. Vaterlaus, D. Guarisco, M. Lutz, M. Aeschlimann, M. Stampanoni, and F. Meier, "Different spin and lattice temperatures observed by spin-polarized photoemission with picosecond laser pulses", *Journal of Applied Physics* **67(9)**, 5661 (1990). 10

[57] A. Vaterlaus, T. Beutler, and F. Meier, "Spin-lattice relaxation time of ferromagnetic gadolinium determined with time-resolved spin-polarized photoemission", *Phys. Rev. Lett.* **67**, 3314 (1991). 10

[58] R. Chimata, A. Bergman, L. Bergqvist, B. Sanyal, and O. Eriksson, "Microscopic Model for Ultrafast Remagnetization Dynamics", *Phys. Rev. Lett.* **109**, 157201 (2012). 10, 11, 13, 87

[59] M. van Kampen, *Ultrafast spin dynamics in ferromagnetic metals*, Ph.D. thesis, Technische Universiteit Eindhoven (2003). 10, 11

[60] S. I. Anisimov, B. L. Kapeliovich, and T. L. Perel'man, "Electron emission from the metal surfaces exposed to ultrashort laser pulses", *Zh. Eksp. Teor. Fiz.* **66**, 776 (1974). 10

[61] J. Tomiska, Q. Jiang, and R. Lück, "Heat capacities of the nickel - palladium system", *Z. Metallkd.* **84**, 755 (1993). 11, 12, 13

[62] J. Hohlfeld, S.-S. Wellershoff, J. Güdde, U. Conrad, V. Jähnke, and E. Matthias, "Electron and lattice dynamics following optical excitation of metals", *Chemical Physics* **251**, 237 (2000). 11, 13, 20

[63] M. Bonn, D. N. Denzler, S. Funk, M. Wolf, S.-S. Wellershoff, and J. Hohlfeld, "Ultrafast electron dynamics at metal surfaces: Competition between electron-phonon coupling and hot-electron transport", *Phys. Rev. B* **61**, 1101 (2000). 11

[64] N. Kazantseva, U. Nowak, R. W. Chantrell, J. Hohlfeld, and A. Rebei, "Slow recovery of the magnetisation after a sub-picosecond heat pulse", *EPL (Europhysics Letters)* **81(2)**, 27004 (2008). 13, 14, 87

[65] R. Carley, K. Döbrich, B. Frietsch, C. Gahl, M. Teichmann, O. Schwarzkopf, P. Wernet, and M. Weinelt, "Femtosecond Laser Excitation Drives Ferromagnetic Gadolinium out of Magnetic Equilibrium", *Phys. Rev. Lett.* **109**, 057401 (2012). 13, 66, 88

[66] B. Y. Mueller, T. Roth, M. Cinchetti, M. Aeschlimann, and B. Rethfeld, "Driving force of ultrafast magnetization dynamics", *New Journal of Physics* **13(12)**, 123010 (2011). 13, 87

[67] N. Kazantseva, D. Hinzke, U. Nowak, R. W. Chantrell, U. Atxitia, and O. Chubykalo-Fesenko, "Towards multiscale modeling of magnetic materials: Simulations of FePt", *Phys. Rev. B* **77**, 184428 (2008). 13, 87

[68] I. Radu, K. Vahaplar, C. Stamm, T. Kachel, N. Pontius, H. A. Durr, T. A. Ostler, J. Barker, R. F. L. Evans, R. W. Chantrell, A. Tsukamoto, A. Itoh, A. Kirilyuk, T. Rasing, and A. V. Kimel, "Transient ferromagnetic-like state mediating ultrafast reversal of antiferromagnetically coupled spins", *Nature* **472(7342)**, 205 (2011). 14, 89

[69] U. Nowak, *Classical Spin Models*, vol. 2, handbook of magnetism and advanced magnetic materials ed., (John Wiley & Sons 2007). 14

[70] U. Atxitia, O. Chubykalo-Fesenko, N. Kazantseva, D. Hinzke, U. Nowak, and R. W. Chantrell, "Micromagnetic modeling of laser-induced magnetization dynamics using the Landau-Lifshitz-Bloch equation", *Applied Physics Letters* **91(23)**, 232507 (2007). 14, 15

[71] D. A. Garanin, "Fokker-Planck and Landau-Lifshitz-Bloch equations for classical ferromagnets", *Phys. Rev. B* **55**, 3050 (1997). 14

[72] U. Atxitia, O. Chubykalo-Fesenko, J. Walowski, A. Mann, and M. Münzenberg, "Evidence for thermal mechanisms in laser-induced femtosecond spin dynamics", *Phys. Rev. B* **81**, 174401 (2010). 15, 87

[73] U. Atxitia and O. Chubykalo-Fesenko, "Ultrafast magnetization dynamics rates within the Landau-Lifshitz-Bloch model", *Phys. Rev. B* **84**, 144414 (2011). 15, 19, 87

[74] B. Koopmans, G. Malinowski, F. Dalla Longa, D. Steiauf, M. Fähnle, T. Roth, M. Cinchetti, and M. Aeschlimann, "Explaining the paradoxical diversity of ultrafast laser-induced demagnetization", *Nature Materials* **9**, 259 (2010). 15, 18, 19, 87, 88

[75] G. P. Zhang, W. Hübner, E. Beaurepaire, and J.-Y. Bigot, *Spin Dynamics in Confined Magnetic Structures I*, (Springer 2002). 15

[76] B. Koopmans, J. Ruigrok, F. Dalla Longa, and W. de Jonge, "Unifying Ultrafast Magnetization Dynamics", *Phys. Rev. Lett.* **95**, 267207 (2005). 15, 18

[77] G. P. Zhang, W. Hubner, G. Lefkidis, Y. Bai, and T. F. George, "Paradigm of the time-resolved magneto-optical Kerr effect for femtosecond magnetism", *Nat Phys* **5(7)**, 499 (2009). 16

[78] K. Carva, M. Battiato, and P. M. Oppeneer, "Is the controversy over femtosecond magneto-optics really solved?", *Nat Phys* **7(9)**, 665 (2011).

[79] G. P. Zhang, W. Hubner, G. Lefkidis, Y. Bai, and T. F. George, "Reply: "Is the controversy over femtosecond magneto-optics really solved?"", *Nat Phys* **7(9)**, 665 (2011). 16

[80] B. Koopmans, M. van Kampen, J. T. Kohlhepp, and W. J. M. de Jonge, "Ultrafast Magneto-Optics in Nickel: Magnetism or Optics?", *Phys. Rev. Lett.* **85**, 844 (2000). 16, 65, 72, 88

[81] P. M. Oppeneer and A. Liebsch, "Ultrafast demagnetization in Ni: theory of magneto-optics for non-equilibrium electron distributions", *Journal of Physics: Condensed Matter* **16(30)**, 5519 (2004). 16, 21, 72, 88

[82] J.-Y. Bigot, M. Vomir, and E. Beaurepaire, "Coherent ultrafast magnetism induced by femtosecond laser pulses", *Nat Phys* **5(7)**, 515 (2009). 16, 87

[83] H. Vonesch and J.-Y. Bigot, "Ultrafast spin-photon interaction investigated with coherent magneto-optics", *Phys. Rev. B* **85**, 180407 (2012). 16, 87

[84] B. Koopmans, H. Kicken, M. van Kampen, and W. de Jonge, "Microscopic model for femtosecond magnetization dynamics", *Journal of Magnetism and Magnetic Materials* **286(0)**, 271 (2005). 17

[85] Y. Yafet, "g Factors and Spin-Lattice Relaxation of Conduction Electrons", vol. 14 of *Solid State Physics*, 1 – 98, (Academic Press 1963). 17

[86] F. Dalla Longa, *Laser-induced magnetization dynamics*, Ph.D. thesis, Technische Universiteit Eindhoven (2008). 18

[87] T. Roth, *The Phenomenon of Laser-Induced Femtosecond Magnetism*, Ph.D. thesis, Technische Universität Kaiserslautern (2011). 18

[88] J. Walowski, G. Müller, M. Djordjevic, M. Münzenberg, M. Kläui, C. A. F. Vaz, and J. A. C. Bland, "Energy Equilibration Processes of Electrons, Magnons, and Phonons at the Femtosecond Time Scale", *Phys. Rev. Lett.* **101**, 237401 (2008). 18

[89] I. Radu, G. Woltersdorf, M. Kiessling, A. Melnikov, U. Bovensiepen, J.-U. Thiele, and C. H. Back, "Laser-Induced Magnetization Dynamics of Lanthanide-Doped Permalloy Thin Films", *Phys. Rev. Lett.* **102**, 117201 (2009). 18

[90] D. Steiauf and M. Fähnle, "Elliott-Yafet mechanism and the discussion of femtosecond magnetization dynamics", *Phys. Rev. B* **79**, 140401 (2009). 19

[91] K. Carva, M. Battiato, and P. M. Oppeneer, "*Ab Initio* Investigation of the Elliott-Yafet Electron-Phonon Mechanism in Laser-Induced Ultrafast Demagnetization", *Phys. Rev. Lett.* **107**, 207201 (2011). 19

[92] R. J. Elliott, "Theory of the Effect of Spin-Orbit Coupling on Magnetic Resonance in Some Semiconductors", *Phys. Rev.* **96**, 266 (1954). 19

[93] M. Cinchetti, M. Sánchez Albaneda, D. Hoffmann, T. Roth, J.-P. Wüstenberg, M. Krauß, O. Andreyev, H. C. Schneider, M. Bauer, and M. Aeschlimann, "Spin-Flip Processes and Ultrafast Magnetization Dynamics in Co: Unifying the Microscopic and Macroscopic View of Femtosecond Magnetism", *Phys. Rev. Lett.* **97**, 177201 (2006). 19, 87

[94] E. Carpene, E. Mancini, C. Dallera, M. Brenna, E. Puppin, and S. De Silvestri, "Dynamics of electron-magnon interaction and ultrafast demagnetization in thin iron films", *Phys. Rev. B* **78**, 174422 (2008). 20, 82, 87

[95] P. B. Allen, "Theory of thermal relaxation of electrons in metals", *Phys. Rev. Lett.* **59**, 1460 (1987). 20

[96] A. B. Schmidt, M. Pickel, M. Donath, P. Buczek, A. Ernst, V. P. Zhukov, P. M. Echenique, L. M. Sandratskii, E. V. Chulkov, and M. Weinelt, "Ultrafast Magnon Generation in an Fe Film on Cu(100)", *Phys. Rev. Lett.* **105**, 197401 (2010). 20, 87

[97] N. Del Fatti, C. Voisin, M. Achermann, S. Tzortzakis, D. Christofilos, and F. Vallée, "Nonequilibrium electron dynamics in noble metals", *Phys. Rev. B* **61**, 16956 (2000). 20, 76

[98] M. Aeschlimann, M. Bauer, and S. Pawlik, "Competing nonradiative channels for hot electron induced surface photochemistry", *Chemical Physics* **205**, 127 (1996). 20

[99] S. D. Brorson, J. G. Fujimoto, and E. P. Ippen, "Femtosecond electronic heat-transport dynamics in thin gold films", *Phys. Rev. Lett.* **59**, 1962 (1987). 20, 69

[100] A. Melnikov, I. Razdolski, T. O. Wehling, E. T. Papaioannou, V. Roddatis, P. Fumagalli, O. Aktsipetrov, A. I. Lichtenstein, and U. Bovensiepen, "Ultrafast Transport of Laser-Excited Spin-Polarized Carriers in Au/Fe/MgO(001)", *Phys. Rev. Lett.* **107**, 076601 (2011). 20, 69, 86, 90

[101] V. P. Zhukov, E. V. Chulkov, and P. M. Echenique, "Lifetimes and inelastic mean free path of low-energy excited electrons in Fe, Ni, Pt, and Au: *Ab initio* GW + T calculations", *Phys. Rev. B* **73**, 125105 (2006). 21, 76, 82

[102] M. Battiato, K. Carva, and P. M. Oppeneer, "Theory of laser-induced ultrafast superdiffusive spin transport in layered heterostructures", *Phys. Rev. B* **86**, 024404 (2012). 21, 75, 76, 87

[103] V. P. Zhukov, E. V. Chulkov, and P. M. Echenique, "GW + T theory of excited electron lifetimes in metals", *Phys. Rev. B* **72**, 155109 (2005). 21

[104] J. Jackson, *Classical Electrodynamics*, (John Wiley & Sons 1999). 25

[105] M. Pretorius, *Magnetooptische Effekte mit linear polarisierter Synchrotronstrahlung im Bereich der 3p-Absorptionskanten der 3d-Übergangsmetalle Fe, Co und Ni*, Ph.D. thesis, Universität Hamburg (1999). 25, 26, 27, 29, 34, 35

[106] S. Lovesey and S. Collins, *X-Ray Scattering and Absorption by Magnetic Materials*, (Clarendon Press, Oxford 1996). 26, 31, 32

[107] M. Freiser, "A Survey of Magnetooptic Effects", *IEEE Transactions on Magnetics* **4**, 152 (1968). 26

[108] P. M. Oppeneer, "Magneto-Optical Kerr Spectra", vol. 13 of *Handbook of Magnetic Materials*, 229 – 422, (Elsevier 2001). 26

[109] H. R. Hulme, "The Faraday Effect in Ferromagnetics", *Proceedings of the Royal Society of London. Series A* **135(826)**, 237 (1932). 30

[110] O. Halpern, "Notiz über die Rotationspolarisation ferromagnetischer Körper", *Annalen der Physik* **404(2)**, 181 (1932). 30

[111] P. N. Argyres, "Theory of the Faraday and Kerr Effects in Ferromagnetics", *Phys. Rev.* **97**, 334 (1955). 30

[112] K. Buschow, "Chapter 5: Magneto-optical properties of alloys and intermetallic compounds", vol. 4 of *Handbook of Ferromagnetic Materials*, 493 – 595, (Elsevier 1988). 30

[113] P. M. Oppeneer, J. Sticht, T. Maurer, and J. Kübler, "Ab initio investigation of microscopic enhancement factors in tuning the magneto-optical Kerr effect", *Zeitschrift für Physik B Condensed Matter* **88**, 309 (1992). 31

[114] C. S. Wang and J. Callaway, "Band structure of nickel: Spin-orbit coupling, the Fermi surface, and the optical conductivity", *Phys. Rev. B* **9**, 4897 (1974). 31

[115] J. L. Erskine and E. A. Stern, "Calculation of the M_{23} magneto-optical absorption spectrum of ferromagnetic nickel", *Phys. Rev. B* **12**, 5016 (1975). 31, 32

[116] H. Höchst, D. Zhao, and D. L. Huber, "$M_{2,3}$ magnetic circular dichroism (MCD) measurements of Fe, Co and Ni using a newly developed quadruple reflection phase shifter", *Surface Science* **352-354(0)**, 998 (1996). 31

[117] F. U. Hillebrecht, T. Kinoshita, D. Spanke, J. Dresselhaus, C. Roth, H. B. Rose, and E. Kisker, "New Magnetic Linear Dichroism in Total Photoelectron Yield for Magnetic Domain Imaging", *Phys. Rev. Lett.* **75**, 2224 (1995). 34

[118] Y. Liu, Z. Xu, P. D. Johnson, and G. van der Laan, "Spin-orbit coupling, exchange interaction, and hybridization in the photoexcitation of the Ni 3 p core level", *Phys. Rev. B* **52**, R8593 (1995).

[119] M. Sacchi, G. Panaccione, J. Vogel, A. Mirone, and G. v. d. Laan, "Magnetic dichroism in reflectivity and photoemission using linearly polarized light: 3p core level of Ni(110)", *Phys. Rev. B* **58**, 3750 (1998).

[120] M. Hecker, P. M. Oppeneer, S. Valencia, H. C. Mertins, and C. M. Schneider, "Soft X-ray magnetic reflection spectroscopy at the 3p absorption edges of thin Fe films", *Journal of Electron Spectroscopy and Related Phenomena* **144-147(0)**, 881 (2005). 34

[121] P. Grychtol, R. Adam, A. M. Kaiser, S. Cramm, D. Bürgler, and C. M. Schneider, "Layer-selective studies of an anti-ferromagnetically coupled multilayer by resonant magnetic reflectivity in the extreme ultraviolet range", *Journal of Electron Spectroscopy and Related Phenomena* **184(3-6)**, 287 (2011). 31, 34

[122] B. T. Thole, P. Carra, F. Sette, and G. van der Laan, "X-ray circular dichroism as a probe of orbital magnetization", *Phys. Rev. Lett.* **68**, 1943 (1992). 31

[123] C. Kao, J. B. Hastings, E. D. Johnson, D. P. Siddons, G. C. Smith, and G. A. Prinz, "Magnetic-resonance exchange scattering at the iron L_{II} and L_{III} edges", *Phys. Rev. Lett.* **65**, 373 (1990). 31, 32

[124] J. B. Kortright, M. Rice, and R. Carr, "Soft-x-ray Faraday rotation at Fe $L_{2,3}$ edges", *Phys. Rev. B* **51**, 10240 (1995). 32

[125] H.-C. Mertins, D. Abramsohn, A. Gaupp, F. Schäfers, W. Gudat, O. Zaharko, H. Grimmer, and P. M. Oppeneer, "Resonant magnetic reflection coefficients at the Fe 2p edge obtained with linearly and circularly polarized soft x rays", *Phys. Rev. B* **66**, 184404 (2002).

[126] H.-C. Mertins, S. Valencia, D. Abramsohn, A. Gaupp, W. Gudat, and P. M. Oppeneer, "X-ray Kerr rotation and ellipticity spectra at the 2p edges of Fe, Co, and Ni", *Phys. Rev. B* **69**, 064407 (2004).

[127] H.-C. Mertins, S. Valencia, A. Gaupp, W. Gudat, P. M. Oppeneer, and C. M. Schneider, "Magneto-optical polarization spectroscopy with soft X-rays", *Applied Physics A* **80**, 1011 (2005). 31, 32

[128] K. Namikawa, M. Ando, T. Nakajima, and H. Kawata, "X-Ray Resonance Magnetic Scattering", *Journal of the Physical Society of Japan* **54(11)**, 4099 (1985). 31, 32

[129] K. Namikawa, M. Ando, T. Nakajima, and H. Kawata, "X-Ray Resonance Magnetic Scattering", *Journal of the Physical Society of Japan* **55(8)**, 2906 (1986). 31, 32

[130] H. Ebert, "Fully relativistic treatment of core states for spin-dependent potential", *Journal of Physics: Condensed Matter* **1(46)**, 9111 (1989). 33

[131] G. Schütz, E. Zech, E. Hagn, and P. Kienle, "Anisotropy of x-rays and spin dependence of the photoabsorption of circularly polarized soft x-rays in magnetized Fe", *Hyperfine Interactions* **16**, 1039 (1983). 32

[132] A. Yoshida and T. Jo, "Calculation of Magnetic CircularDichroism in 3*p*-Core XAS for Ni", *Journal of the Physical Society of Japan* **60(6)**, 2098 (1991). 32

[133] S. Valencia, A. Kleibert, A. Gaupp, J. Rusz, D. Legut, J. Bansmann, W. Gudat, and P. M. Oppeneer, "Quadratic X-Ray Magneto-Optical Effect upon Reflection in a Near-Normal-Incidence Configuration at the *M* Edges of 3*d*-Transition Metals", *Phys. Rev. Lett.* **104**, 187401 (2010). 34

[134] P. Grychtol, *Element-selective and time-resolved magnetic investigations in the extreme ultraviolet range*, Ph.D. thesis, Research Centre Jülich (2011). 34

[135] R. Adam, P. Grychtol, S. Cramm, and C. M. Schneider, "Time-resolved measurements of $Ni_{80}Fe_{20}$/MgO/Co trilayers in the extreme ultraviolet range", *Journal of Electron Spectroscopy and Related Phenomena* **184**, 291 (2011). 34

[136] S. Višňovský, "Optics of Magnetic Multilayers", *Czechoslovak Journal of Physics* **41**, 663 (1991). 34

[137] P. Yeh, "Optics of anisotropic layered media: A new 4 x 4 matrix algebra", *Surface Science* **96(1-3)**, 41 (1980). 34

[138] http://hdl.handle.net/2128/2605 (2011). 35

[139] P. A. Franken, A. E. Hill, C. W. Peters, and G. Weinreich, "Generation of Optical Harmonics", *Phys. Rev. Lett.* **7**, 118 (1961). 36

[140] R. A. Bartels, A. Paul, H. Green, H. C. Kapteyn, M. M. Murnane, S. Backus, I. P. Christov, Y. Liu, D. Attwood, and C. Jacobsen, "Generation of Spatially Coherent Light at Extreme Ultraviolet Wavelengths", *Science* **297(5580)**, 376 (2002). 36

[141] D. Hemmers and G. Pretzler, "Multi-color XUV interferometry using high-order harmonics", *Applied Physics B* **95**, 667 (2009). 36

[142] T. Pfeifer, C. Spielmann, and G. Gerber, "Femtosecond x-ray science", *Reports on Progress in Physics* **69(2)**, 443 (2006). 36, 37, 38, 39

[143] Y. Baba and V. Rakov, "Present Understanding of the Lightning Return Stroke", in H. D. Betz (Editor), "Lightning: Principles, Instruments and Applications", , (Springer 2009). 36

[144] P. B. Corkum, "Plasma perspective on strong field multiphoton ionization", *Phys. Rev. Lett.* **71**, 1994 (1993). 36, 37, 38

[145] J. L. Krause, K. J. Schafer, and K. C. Kulander, "High-order harmonic generation from atoms and ions in the high intensity regime", *Phys. Rev. Lett.* **68**, 3535 (1992). 37

[146] D. N. Fittinghoff, P. R. Bolton, B. Chang, and K. C. Kulander, "Observation of nonsequential double ionization of helium with optical tunneling", *Phys. Rev. Lett.* **69**, 2642 (1992). 38

[147] U. Mohideen, M. H. Sher, H. W. K. Tom, G. D. Aumiller, O. R. Wood, R. R. Freeman, J. Boker, and P. H. Bucksbaum, "High intensity above-threshold ionization of He", *Phys. Rev. Lett.* **71**, 509 (1993). 38

[148] A. L'Huillier, K. J. Schafer, and K. C. Kulander, "Higher-order harmonic generation in xenon at 1064 nm: The role of phase matching", *Phys. Rev. Lett.* **66**, 2200 (1991). 38

[149] A. L'Huillier and P. Balcou, "High-order harmonic generation in rare gases with a 1-ps 1053-nm laser", *Phys. Rev. Lett.* **70**, 774 (1993). 39

[150] J. Zhou, J. Peatross, M. M. Murnane, H. C. Kapteyn, and I. P. Christov, "Enhanced High-Harmonic Generation Using 25 fs Laser Pulses", *Phys. Rev. Lett.* **76**, 752 (1996).

[151] P. Salières, B. Carré, L. Le Déroff, F. Grasbon, G. G. Paulus, H. Walther, R. Kopold, W. Becker, D. B. Milošević, A. Sanpera, and M. Lewenstein, "Feynman's Path-Integral Approach for Intense-Laser-Atom Interactions", *Science* **292(5518)**, 902 (2001).

[152] M. Nisoli, E. Priori, G. Sansone, S. Stagira, G. Cerullo, S. De Silvestri, C. Altucci, R. Bruzzese, C. de Lisio, P. Villoresi, L. Poletto, M. Pascolini, and G. Tondello, "High-Brightness High-Order Harmonic Generation by Truncated Bessel Beams in the Sub-10-fs Regime", *Phys. Rev. Lett.* **88**, 033902 (2002). 39

[153] A. Rundquist, C. G. Durfee, Z. Chang, C. Herne, S. Backus, M. M. Murnane, and H. C. Kapteyn, "Phase-Matched Generation of Coherent Soft X-rays", *Science* **280(5368)**, 1412 (1998). 39

[154] M. Schnürer, Z. Cheng, S. Sartania, M. Hentschel, G. Tempea, T. Brabec, and F. Krausz, "Guiding and high-harmonic generation of sub-10-fs pulses in hollow-core fibers at 1015 W/cm2", *Applied Physics B* **67**, 263 (1998).

[155] C. G. Durfee, A. R. Rundquist, S. Backus, C. Herne, M. M. Murnane, and H. C. Kapteyn, "Phase Matching of High-Order Harmonics in Hollow Waveguides", *Phys. Rev. Lett.* **83**, 2187 (1999).

[156] Y. Tamaki, Y. Nagata, M. Obara, and K. Midorikawa, "Phase-matched high-order-harmonic generation in a gas-filled hollow fiber", *Phys. Rev. A* **59**, 4041 (1999). 39

[157] A. Siegman, *Lasers*, (University Science Books 1986). 39

[158] M. Geissler, G. Tempea, and T. Brabec, "Phase-matched high-order harmonic generation in the nonadiabatic limit", *Phys. Rev. A* **62**, 033817 (2000). 39, 40

[159] J. Seres, E. Seres, A. J. Verhoef, G. Tempea, C. Streli, P. Wobrauschek, V. Yakovlev, A. Scrinzi, C. Spielmann, and F. Krausz, "Laser technology: Source of coherent kiloelectronvolt X-rays", *Nature* **433(7026)**, 596 (2005). 39

[160] E. Constant, D. Garzella, P. Breger, E. Mével, C. Dorrer, C. Le Blanc, F. Salin, and P. Agostini, "Optimizing High Harmonic Generation in Absorbing Gases: Model and Experiment", *Phys. Rev. Lett.* **82**, 1668 (1999). 39

[161] C. Winterfeldt, C. Spielmann, and G. Gerber, "Colloquium: Optimal control of high-harmonic generation", *Rev. Mod. Phys.* **80**, 117 (2008). 39

[162] D. Walter, T. Pfeifer, C. Winterfeldt, R. Kemmer, R. Spitzenpfeil, G. Gerber, and C. Spielmann, "Adaptive spatial control of fiber modes and their excitation for high-harmonic generation", *Opt. Express* **14(8)**, 3433 (2006). 39

[163] M. V. Frolov, N. L. Manakov, and A. F. Starace, "Wavelength Scaling of High-Harmonic Yield: Threshold Phenomena and Bound State Symmetry Dependence", *Phys. Rev. Lett.* **100**, 173001 (2008). 39

[164] E. A. Gibson, A. Paul, N. Wagner, R. Tobey, D. Gaudiosi, S. Backus, I. P. Christov, A. Aquila, E. M. Gullikson, D. T. Attwood, M. M. Murnane, and H. C. Kapteyn, "Coherent Soft X-ray Generation in the Water Window with Quasi-Phase Matching", *Science* **302(5642)**, 95 (2003). 39

[165] E. Seres, J. Seres, F. Krausz, and C. Spielmann, "Generation of Coherent Soft-X-Ray Radiation Extending Far Beyond the Titanium *L* Edge", *Phys. Rev. Lett.* **92**, 163002 (2004). 39

[166] C. La-o vorakiat, *Element-Selective Ultrafast Magnetization Dynamics with a Tabletop Light Source*, Ph.D. thesis, University of Colorado (2011). 41, 44, 45

[167] D. Strickland and G. Mourou, "Compression of amplified chirped optical pulses", *Optics Communications* **55(6)**, 447 (1985). 41

[168] N. Keul, *Realisierung eines SHG-FROG zur Charakterisierung eines Laserverstärkersystems für die Erzeugung von Höheren Harmonischen in Edelgasen*, Master's thesis, Fachhochschule Koblenz, RheinAhrCampus Remagen (2010). 41

[169] D. Rudolf, C. La-o vorakiat, E. Turgut, P. Grychtol, R. Adam, S. Mathias, J. M. Shaw, H. T. Nembach, T. J. Silva, M. Aeschlimann, C. M. Schneider, M. M. Murnane, and H. C. Kapteyn, "Andor CCD camera application note: Element-selective ultrafast magnetization dynamics", *Tech. rep.*, LOT-Oriel (2012). 43

[170] G. P. Williams, *X-Ray Data Booklet*, chap. Electron Binding Energies, (Lawrence Berkeley National Laboratory 2001). 44

[171] A. L'Huillier, P. Balcou, S. Candel, K. J. Schafer, and K. C. Kulander, "Calculations of high-order harmonic-generation processes in xenon at 1064 nm", *Phys. Rev. A* **46**, 2778 (1992). 44, 45

[172] B. Henke, E. Gullikson, and J. Davis, "X-Ray Interactions: Photoabsorption, Scattering, Transmission, and Reflection at E = 50-30,000 eV, Z = 1-92", *Atomic Data and Nuclear Data Tables* **54(2)**, 181 (1993). 46, 48

[173] G. Bohm and G. Zech, *Introduction to Statistics and Data Analysis for Physicists*, (Verlag Deutsches Elektronen-Synchrotron 2010). 46

[174] Z.-H. Loh, M. Khalil, R. E. Correa, and S. R. Leone, "A tabletop femtosecond time-resolved soft x-ray transient absorption spectrometer", *Review of Scientific Instruments* **79(7)**, 073101 (2008). 48

[175] S. Mathias, C. La-O-Vorakiat, P. Grychtol, P. Granitzka, E. Turgut, J. M. Shaw, R. Adam, H. T. Nembach, M. E. Siemens, S. Eich, C. M. Schneider, T. J. Silva, M. Aeschlimann, M. M. Murnane, and H. C. Kapteyn, "Probing the timescale of the exchange interaction in a ferromagnetic alloy", *Proceedings of the National Academy of Sciences of the United States of America* **109**, 4792 (2012). 48, 73, 74, 87, 88

[176] J. Hauck, R. Freiberger, and L. Juschkin, "Performance benchmark of a gateable microchannel plate detector for extreme ultraviolet radiation with high temporal resolution", *SPIE Proceedings, EUV and X-Ray Optics: Synergy between Laboratory and Space II* **8076**, 80760R (2011). 48

[177] R. Freiberger, J. Hauck, D. Lvovsky, R. Adam, S. Danylyuk, and L. Juschkin, "Gateable micro channel plate detector for extreme ultraviolet radiation with high temporal resolution", *JARA-FIT Annual Report* 145–146 (2011). 48

[178] T. Mocek, J. Polan, P. Homer, K. Jakubczak, B. Rus, I. J. Kim, C. M. Kim, G. H. Lee, C. H. Nam, V. Hajkova, J. Chalupsky, and L. Juha, "Surface modification of organic polymer by dual action of extreme ultraviolet/visible-near infrared ultrashort pulses", *Journal of Applied Physics* **105(2)**, 026105 (2009). 48

[179] The bandwidth of a single high harmonic depends on the laser parameters, e.g. pulse duration, chirp, photon energy, intensity etc. and amounts to 1–1.5 eV in our experiment. (Private communication with H. C. Kapteyn). 51

[180] Private communication with J. M. Shaw. 56, 73

[181] http://henke.lbl.gov/optical_constants/ (2011). 56

[182] S. Parkin and D. Mauri, "Spin engineering: Direct determination of the Ruderman-Kittel-Kasuya-Yosida far-field range function in ruthenium", *Phys. Rev. B* **44**, 7131 (1991). 56, 59

[183] F. Nguyen van Dau, A. Fert, P. Etienne, M. N. Baibich, J. M. Broto, J. Chazelas, G. Creuzet, A. Friederich, S. Hadjoudj, H. Hurdequint, J. P. Redoulès, and J. Massies, "Magnetic Properties of (001)Fe/(001)Cr bcc Multilayers", *J. Phys. Colloques* **49**, C8 (1988). 58

[184] S. S. P. Parkin, A. Mansour, and G. P. Felcher, "Antiferromagnetic interlayer exchange coupling in sputtered Fe/Cr multilayers: Dependence on number of Fe layers", *Applied Physics Letters* **58(14)**, 1473 (1991). 58

[185] R. C. O'Handley, *Modern Magnetic Materials: Principles and Applications*, (John Wiley & Sons, Inc. 2000). 59

[186] S. S. P. Parkin, "Systematic variation of the strength and oscillation period of indirect magnetic exchange coupling through the $3d$, $4d$ and $5d$ transition metals", *Phys. Rev. Lett.* **67**, 3598 (1991). 59

[187] D. M. Edwards, J. Mathon, R. B. Muniz, and M. S. Phan, "Oscillations of the exchange in magnetic multilayers as an analog of de Haas/van Alphen effect", *Phys. Rev. Lett.* **67**, 493 (1991). 60

[188] A. T. Costa, J. d'Albuquerque e Castro, M. S. Ferreira, and R. B. Muniz, "Inadequacy of the asymptotic approximation for the interlayer coupling in Fe/Ag/Fe and Fe/Au/Fe (001) trilayers", *Phys. Rev. B* **60**, 11894 (1999). 60

[189] S. Schwieger and W. Nolting, "Origin of the temperature dependence of interlayer exchange coupling in metallic trilayers", *Phys. Rev. B* **69**, 224413 (2004). 60, 62

[190] M. A. Plötzing, *Ultrafast Demagnetization Dynamics in Ni_xPd_{1-x} alloys*, Master's thesis, Forschungszentrum Jülich (2011). 63

[191] B. Heller, *Studies on magnetic multilayers and alloys employing the magneto-optical Kerr-effect in the visible and XUV ranges*, Master's thesis, Forschungszentrum Jülich (2011). 63, 70

[192] T. Kampfrath, R. G. Ulbrich, F. Leuenberger, M. Münzenberg, B. Sass, and W. Felsch, "Ultrafast magneto-optical response of iron thin films", *Phys. Rev. B* **65**, 104429 (2002). 65, 72, 82, 87

[193] H.-S. Rhie, H. A. Dürr, and W. Eberhardt, "Femtosecond Electron and Spin Dynamics in Ni/W(110) Films", *Phys. Rev. Lett.* **90**, 247201 (2003). 66, 88

[194] H. Kubota, S. Ishio, T. Miyazaki, and Z. Stadnik, "Giant magnetoresistance and interlayer exchange coupling in Ni-Co/Cu multilayer films", *Journal of Magnetism and Magnetic Materials* **129**, 383 (1994). 67

[195] G. Ju, A. V. Nurmikko, R. F. C. Farrow, R. F. Marks, M. J. Carey, and B. A. Gurney, "Ultrafast Time Resolved Photoinduced Magnetization Rotation in a Ferromagnetic/Antiferromagnetic Exchange Coupled System", *Phys. Rev. Lett.* **82**, 3705 (1999). 67, 89

[196] F. Dalla Longa, J. T. Kohlhepp, W. J. M. de Jonge, and B. Koopmans, "Resolving the genuine laser-induced ultrafast dynamics of exchange interaction in ferromagnet/antiferromagnet bilayers", *Phys. Rev. B* **81**, 094435 (2010). 67, 89

[197] G. Malinowski, F. Dalla Longa, J. Rietjens, P. Paluskar, R. Huijink, H. Swagten, and B. Koopmans, "Control of speed and efficiency of ultrafast demagnetization by direct transfer of spin angular momentum", *Nature Physics* **4**, 855 (2008). 69, 86, 90

[198] B. Pfau, S. Schaffert, L. Müller, C. Gutt, A. Al-Shemmary, F. Büttner, R. Delaunay, S. Düsterer, S. Flewett, R. Frömter, J. Geilhufe, E. Guehrs, C. Günther, R. Hawaldar, M. Hille, N. Jaouen, A. Kobs, K. Li, J. Mohanty, H. Redlin, W. Schlotter, D. Stickler, R. Treusch, B. Vodungbo, M. Kläui, H. Oepen, J. Lüning, G. Grübel, and S. Eisebitt, "Ultrafast optical demagnetization manipulates nanoscale spin structure in domain walls", *Nat Commun* **3**, 1100 (2012). 90

[199] T. Kampfrath, M. Battiato, P. Maldonado, G. Eilers, J. Nötzold, S. Mährlein, V. Zbarsky, F. Freimuth, Y. Mokrousov, S. Blügel, M. Wolf, I. Radu, P. M. Oppeneer, and M. Münzenberg, "Terahertz spin current pulses controlled by magnetic heterostructures", *Nat Nano* **8(4)**, 256 (2013). 81, 90

[200] E. Turgut, C. La-O-Vorakiat, J. M. Shaw, P. Grychtol, H. T. Nembach, D. Rudolf, R. Adam, M. Aeschlimann, C. M. Schneider, T. J. Silva, M. M. Murnane, H. C.

Kapteyn, and S. Mathias, "Controlling the competition between optically induced ultrafast spin-flip scattering and spin transport in magnetic multilayers", *accepted in Phys. Rev. Lett.* (2013). 82, 86, 90

[201] A. Eschenlohr, M. Battiato, P. Maldonado, N. Pontius, T. Kachel, K. Holldack, R. Mitzner, A. Föhlisch, P. M. Oppeneer, and C. Stamm, "Ultrafast spin transport as key to femtosecond demagnetization", *Nat Mater* **advance online publication**, (2013). 69, 86, 91

[202] B. Koopmans, *Handbook of Magnetism and Advanced Magnetic Materials*, vol. 3, chap. Time-resolved Kerr-effect and Spin Dynamics in Itinerant Ferromagnets, 1589–1613, (Wiley 2007). 69

[203] D. Steil, S. Alebrand, T. Roth, M. Krauß, T. Kubota, M. Oogane, Y. Ando, H. C. Schneider, M. Aeschlimann, and M. Cinchetti, "Band-Structure-Dependent Demagnetization in the Heusler Alloy $Co_2Mn_{1-x}Fe_xSi$", *Phys. Rev. Lett.* **105**, 217202 (2010). 70

[204] K. Carva, D. Legut, and P. M. Oppeneer, "Influence of laser-excited electron distributions on the X-ray magnetic circular dichroism spectra: Implications for femtosecond demagnetization in Ni", *EPL* **86**, 57002 (2009). 72

[205] C. La-O-Vorakiat, E. Turgut, C. A. Teale, H. C. Kapteyn, M. M. Murnane, S. Mathias, M. Aeschlimann, C. M. Schneider, J. M. Shaw, H. T. Nembach, and T. J. Silva, "Ultrafast Demagnetization Measurements Using Extreme Ultraviolet Light: Comparison of Electronic and Magnetic Contributions", *Phys. Rev. X* **2**, 011005 (2012). 72

[206] P. Yeh, *Optical Waves in Layered Media*, (John Wiley & Sons 1988). 73

[207] Private communication with T. J. Silva and E. Turgut. 73

[208] The measurements were performed by C. La–O–Vorakiat and E. Turgut at JILA, University of Colorado (Boulder). 77

[209] E. D. Palik (Editor), *Handbook of optical constants of solids*, (Academic Press 1998). 73

[210] S. Mao, F. Quéré, S. Guizard, X. Mao, R. Russo, G. Petite, and P. Martin, "Dynamics of femtosecond laser interactions with dielectrics", *Applied Physics A* **79**, 1695 (2004). 73

[211] L. Guidoni, E. Beaurepaire, and J.-Y. Bigot, "Magneto-optics in the Ultrafast Regime: Thermalization of Spin Populations in Ferromagnetic Films", *Phys. Rev. Lett.* **89**, 017401 (2002). 73, 87, 88

[212] M. Aeschlimann, M. Bauer, S. Pawlik, W. Weber, R. Burgermeister, D. Oberli, and H. C. Siegmann, "Ultrafast Spin-Dependent Electron Dynamics in fcc Co", *Phys. Rev. Lett.* **79**, 5158 (1997). 76

[213] S. van Dijken, X. Jiang, and S. S. P. Parkin, "Spin-dependent hot electron transport in $Ni_{81}Fe_{19}$ and $Co_{84}Fe_{16}$ films on GaAs(001)", *Phys. Rev. B* **66**, 094417 (2002). 76, 82

[214] L. Braicovich and G. van der Laan, "Rationale for femtosecond magnetism explored with x-ray core-hole excitation", *Phys. Rev. B* **78**, 174421 (2008). 76

[215] The calculations were performed by M. Battiato, P. Maldonado and P. M. Oppeneer from the Uppsala University in Sweden. 80, 81

[216] J. Bass and W. P. Pratt Jr, "Spin-diffusion lengths in metals and alloys, and spin-flipping at metal/metal interfaces: an experimentalist's critical review", *Journal of Physics: Condensed Matter* **19(18)**, 183201 (2007). 81

[217] F. Liu, T. Makino, T. Yamasaki, K. Ueno, A. Tsukazaki, T. Fukumura, Y. Kong, and M. Kawasaki, "Ultrafast Time-Resolved Faraday Rotation in EuO Thin Films", *Phys. Rev. Lett.* **108**, 257401 (2012). 82, 89

[218] J. Wang, I. Cotoros, K. M. Dani, X. Liu, J. K. Furdyna, and D. S. Chemla, "Ultrafast Enhancement of Ferromagnetism via Photoexcited Holes in GaMnAs", *Phys. Rev. Lett.* **98**, 217401 (2007). 82, 89

[219] D. Ralph and M. Stiles, "Spin transfer torques", *Journal of Magnetism and Magnetic Materials* **320(7)**, 1190 (2008). 83

[220] J. A. Katine, F. J. Albert, R. A. Buhrman, E. B. Myers, and D. C. Ralph, "Current-Driven Magnetization Reversal and Spin-Wave Excitations in Co /Cu /Co Pillars", *Phys. Rev. Lett.* **84**, 3149 (2000). 83

[221] Y. Acremann, J. P. Strachan, V. Chembrolu, S. D. Andrews, T. Tyliszczak, J. A. Katine, M. J. Carey, B. M. Clemens, H. C. Siegmann, and J. Stöhr, "Time-Resolved Imaging of Spin Transfer Switching: Beyond the Macrospin Concept", *Phys. Rev. Lett.* **96**, 217202 (2006). 83

[222] J. Hohlfeld, E. Matthias, R. Knorren, and K. H. Bennemann, "Nonequilibrium Magnetization Dynamics of Nickel", *Phys. Rev. Lett.* **78**, 4861 (1997). 87

[223] C. Stamm, T. Kachel, N. Pontius, R. Mitzner, T. Quast, K. Holldack, S. Khan, C. Lupulescu, E. Aziz, H. Wietstruk, M.and Dürr, and W. Eberhardt, "Femtosecond modification of electron localization and transfer of angular momentum in nickel", *Nature Materials* **6**, 740 (2007). 87

[224] G. P. Zhang and W. Hübner, "Laser-Induced Ultrafast Demagnetization in Ferromagnetic Metals", *Phys. Rev. Lett.* **85**, 3025 (2000). 87

[225] M. Krauß, T. Roth, S. Alebrand, D. Steil, M. Cinchetti, M. Aeschlimann, and H. C. Schneider, "Ultrafast demagnetization of ferromagnetic transition metals: The role of the Coulomb interaction", *Phys. Rev. B* **80**, 180407 (2009). 87

[226] T. Roth, A. J. Schellekens, S. Alebrand, O. Schmitt, D. Steil, B. Koopmans, M. Cinchetti, and M. Aeschlimann, "Temperature Dependence of Laser-Induced Demagnetization in Ni: A Key for Identifying the Underlying Mechanism", *Phys. Rev. X* **2**, 021006 (2012). 87, 88

[227] M. Wietstruk, A. Melnikov, C. Stamm, T. Kachel, N. Pontius, M. Sultan, C. Gahl, M. Weinelt, H. A. Dürr, and U. Bovensiepen, "Hot-Electron-Driven Enhancement of Spin-Lattice Coupling in Gd and Tb $4f$ Ferromagnets Observed by Femtosecond X-Ray Magnetic Circular Dichroism", *Phys. Rev. Lett.* **106**, 127401 (2011). 88

[228] G. M. Müller, J. Walowski, M. Djordjevic, G.-X. Miao, A. Gupta, A. V. Ramos, K. Gehrke, V. Moshnyaga, K. Samwer, J. Schmalhorst, A. Thomas, A. Hütten, G. Reiss, J. S. Moodera, and M. Münzenberg, "Spin polarization in half-metals probed by femtosecond spin excitation", *Nat Mater* **8(1)**, 56 (2009). 88

[229] A. V. Kimel, R. V. Pisarev, J. Hohlfeld, and T. Rasing, "Ultrafast Quenching of the Antiferromagnetic Order in $FeBO_3$: Direct Optical Probing of the Phonon-Magnon Coupling", *Phys. Rev. Lett.* **89**, 287401 (2002). 88

[230] T. Ogasawara, K. Ohgushi, Y. Tomioka, K. S. Takahashi, H. Okamoto, M. Kawasaki, and Y. Tokura, "General Features of Photoinduced Spin Dynamics in Ferromagnetic and Ferrimagnetic Compounds", *Phys. Rev. Lett.* **94**, 087202 (2005). 88

[231] E. Beaurepaire, G. M. Turner, S. M. Harrel, M. C. Beard, J.-Y. Bigot, and C. A. Schmuttenmaer, "Coherent terahertz emission from ferromagnetic films excited by femtosecond laser pulses", *Applied Physics Letters* **84(18)**, 3465 (2004). 88

[232] D. J. Hilton, R. D. Averitt, C. A. Meserole, G. L. Fisher, D. J. Funk, J. D. Thompson, and A. J. Taylor, "Terahertz emission via ultrashort-pulse excitation of magnetic metalfilms", *Opt. Lett.* **29(15)**, 1805 (2004). 88

[233] C. Boeglin, E. Beaurepaire, V. Halté, V. López-Flores, C. Stamm, N. Pontius, H. Dürr, and J.-Y. Bigot, "Distinguishing the ultrafast dynamics of spin and orbital moments in solids", *Nature* **465**, 458 (2010). 88

[234] C. Stamm, N. Pontius, T. Kachel, M. Wietstruk, and H. A. Dürr, "Femtosecond x-ray absorption spectroscopy of spin and orbital angular momentum in photoexcited Ni films during ultrafast demagnetization", *Phys. Rev. B* **81**, 104425 (2010). 88

[235] C. D. Stanciu, A. Tsukamoto, A. V. Kimel, F. Hansteen, A. Kirilyuk, A. Itoh, and T. Rasing, "Subpicosecond Magnetization Reversal across Ferrimagnetic Compensation Points", *Phys. Rev. Lett.* **99**, 217204 (2007). 88

[236] C. D. Stanciu, F. Hansteen, A. V. Kimel, A. Kirilyuk, A. Tsukamoto, A. Itoh, and T. Rasing, "All-Optical Magnetic Recording with Circulary Polarized Light", *Phys. Rev. Lett.* **99**, 047601 (2007). 88

[237] S. Alebrand, M. Gottwald, M. Hehn, D. Steil, M. Cinchetti, D. Lacour, E. E. Fullerton, M. Aeschlimann, and S. Mangin, "Light-induced magnetization reversal of high-anisotropy TbCo alloy films", *Applied Physics Letters* **101(16)**, 162408 (2012). 88

[238] A. V. Kimel, A. Kirilyuk, P. A. Usachev, R. V. Pisarev, A. M. Balbashov, and T. Rasing, "Ultrafast non-thermal control of magnetization by instantaneous photomagnetic pulses", *Nature* **435(7042)**, 655 (2005). 89

[239] P. Nemec, E. Rozkotova, N. Tesarova, F. Trojanek, E. De Ranieri, K. Olejnik, J. Zemen, V. Novak, M. Cukr, P. Maly, and T. Jungwirth, "Experimental observation of the optical spin transfer torque", *Nat Phys* **8(5)**, 411 (2012). 89

[240] E. Beaurepaire, M. Maret, V. Halté, J.-C. Merle, A. Daunois, and J.-Y. Bigot, "Spin dynamics in $CoPt_3$ alloy films: A magnetic phase transition in the femtosecond time scale", *Phys. Rev. B* **58**, 12134 (1998). 89

[241] G. Ju, J. Hohlfeld, B. Bergman, R. J. M. van de Veerdonk, O. N. Mryasov, J.-Y. Kim, X. Wu, D. Weller, and B. Koopmans, "Ultrafast Generation of Ferromagnetic Order via a Laser-Induced Phase Transformation in FeRh Thin Films", *Phys. Rev. Lett.* **93**, 197403 (2004). 89

[242] J.-U. Thiele, M. Buess, and C. H. Back, "Spin dynamics of the antiferromagnetic-to-ferromagnetic phase transition in FeRh on a sub-picosecond time scale", *Applied Physics Letters* **85(14)**, 2857 (2004). 89

[243] I. Radu, C. Stamm, N. Pontius, T. Kachel, P. Ramm, J.-U. Thiele, H. A. Dürr, and C. H. Back, "Laser-induced generation and quenching of magnetization on FeRh studied with time-resolved x-ray magnetic circular dichroism", *Phys. Rev. B* **81**, 104415 (2010). 89

[244] F. Quirin, M. Vattilana, U. Shymanovich, A.-E. El-Kamhawy, A. Tarasevitch, J. Hohlfeld, D. von der Linde, and K. Sokolowski-Tinten, "Structural dynamics in FeRh during a laser-induced metamagnetic phase transition", *Phys. Rev. B* **85**, 020103 (2012). 89

[245] A. V. Kimel, A. Kirilyuk, A. Tsvetkov, R. V. Pisarev, and T. Rasing, "Laser-induced ultrafast spin reorientation in the antiferromagnet $TmFeO_3$", *Nature* **429(6994)**, 850 (2004). 89

[246] G. V. Astakhov, A. V. Kimel, G. M. Schott, A. A. Tsvetkov, A. Kirilyuk, D. R. Yakovlev, G. Karczewski, W. Ossau, G. Schmidt, L. W. Molenkamp, and T. Rasing, "Magnetization manipulation in (Ga,Mn)As by subpicosecond optical excitation", *Applied Physics Letters* **86(15)**, 152506 (2005). 89

Publications

R. Freiberger, J. Hauck, **D. Lvovsky**, R. Adam, S. Danylyuk, and L. Juschkin, "Gateable micro channel plate detector for extreme ultraviolet radiation with high temporal resolution", *JARA-FIT Annual Report*, 145-146 (2011)

D. Rudolf, C. La-O-Vorakiat, M. Battiato, R. Adam, J. M. Shaw, E. Turgut, P. Maldonado, S. Mathias, P. Grychtol, H. T. Nembach, T. J. Silva, M. Aeschlimann, H. C. Kapteyn, M. M. Murnane, C. M. Schneider, and P. M. Oppeneer, "Ultrafast magnetization enhancement in metallic multilayers driven by superdiffusive spin current", *Nat Commun* **3**, 1037 (2012)

S. Mathias, C. La-O-Vorakiat, J. M. Shaw, E. Turgut, P. Grychtol, R. Adam, **D. Rudolf**, H. T. Nembach, T. J. Silva, M. Aeschlimann, C. M. Schneider, H. C. Kapteyn, and M. M. Murnane, "Ultrafast element-specific magnetization dynamics of complex magnetic materials on a table-top", *Journal of Electron Spectroscopy and Related Phenomena* (2012), doi: 10.1016/j.elspec.2012.11.013

E. Turgut, C. La-O-Vorakiat, J. M. Shaw, P. Grychtol, H. T. Nembach, **D. Rudolf**, R. Adam, M. Aeschlimann, C. M. Schneider, T. J. Silva, M. M. Murnane, H. C. Kapteyn, and S. Mathias, "Controlling the competition between optically induced ultrafast spin-flip scattering and spin transport in magnetic multilayers", *accepted by Phys. Rev. Lett.* (2013)

C. Weier, R. Adam, **D. Rudolf**, R. Frömter, P. Grychtol, G. Winkler, A. Kobs, H. P. Oepen, H. C. Kapteyn, M. M. Murnane, and C. M. Schneider, "Domain size effects in Co/Pt multilayers studied by magnetic resonant scattering of laser-generated, extreme ultraviolet light," *in preparation* (2013)

Acknowledgements

Without the help of many people this work would not be possible, and therefore, first, I would like to thank Prof. Dr. C. M. Schneider for giving me the possibility to work in his institute and for his continuous support and interest, as well as Prof. Dr. M. Aeschlimann for being my co-referee. Furthermore, I am grateful to all the colleagues from the Peter Grünberg Institut, and especially, Dr. R. Adam, who adviced, supported and motivated me, Dr. P. Grychtol for helping me at the early stage of this work, B. Heller for his measurements and C. Weier for many helpful discussions and proof-reading the thesis. I enjoyed working with my laser group colleagues M. Plötzing, M. Eschbach, J. Martin, A. Bauer, A. Kamay, A. Bartuli and N. Keul. The enlightening discussions with Dr. D. Bürgler and the introduction to the Yeh-MOKE program by Dr. M. Buchmeier are gratefully acknowledged. Without the experience, skills, creative ideas, and, simply, everyday technical support from B. Küpper (CAD construction, vacuum technology, mechanics), K. Bickmann (CAD construction, vacuum technology), J. Lauer (LabView programming, computer support), H. Pfeifer (electronics), T. Jansen (thin film deposition), R. Borowski (clean room technology) and Dr. S. Trellenkamp (electron beam writing), no experiments would be possible.

Next, many thanks to Prof. Dr. M. M. Murnane and Prof. Dr. H. C. Kapteyn for the possibility to conduct experiments in their labs at JILA in Boulder. I would like to thank Dr. C. La-O-Vorakiat and E. Turgut not only for their experimental skills and knowledge about time-resolved T-MOKE measurements with high harmonics, but also for the warm-hearted welcome to Boulder during the measurement time. I am grateful for the constructive discourse with Dr. S. Mathias, Dr. T. J. Silva, Dr. J. M. Shaw and Dr. H. T. Nembach in the process of the manuscript writing and thank Dr. J. M. Shaw for sample preparation.

Moreover, I am very indebted to Prof. Dr. P. M. Oppeneer, M. Battiato and Dr. P. Maldonado for the interpretation of our experimental data and for providing calculations for the publication. In particular, I enjoyed the visit of Prof. Dr. P. M. Oppeneer and M. Battiato to the Research Centre Jülich and learned a lot during the discussions.

Acknowledgements

Next, many thanks to Dr. N. Anderson, Dr. B. Langdon and A. Auger from KMLabs, M. Reuter, M. Hytra and N. Baum from Nexlase and H. Hechler from Spectra Physics for their tireless support with lasers.
Finally, I would like to thank my wife Katharina, my parents Grigori and Marina, Mrs. O. B. and Mr. E. A. Rudolf and all my family.

Curriculum Vitae

Personal Data

Name	Denis Rudolf geb. Lvovsky
Address	Breite Str. 142
	41460 Neuss
E-Mail	d.rudolf@fz-juelich.de
Birthday	01.12.1982
Birthplace	Moscow, Russia
Marital Status	married, one child

Education

from January 2010	Ph.D. work at PGI-6, Research Centre Jülich on
	'Time- and Layer-Resolved Femtosecond
	Spin Dynamics in Magnetic Multilayers
	Employing Laser-Generated High Harmonics'
January 2009-January 2010	diploma thesis at the Fraunhofer Institute for Laser
	Technology in Aachen on
	'Integrated Planar Waveguides
	Prepared by Pulsed Laser Deposition'
April 2007	'Vordiplom' in physics
from summer semester 2005	studies of physics at RWTH Aachen
winter semester 2004/2005	studies of electrical engineering at RWTH Aachen
1994-2003	Geschwister-Scholl-Gymnasium in Pulheim,
	Abitur, final mark: 1.5
1989-1994	primary school in Moscow, Russia

Schriften des Forschungszentrums Jülich
Reihe Schlüsseltechnologien / Key Technologies

Band / Volume 56
Interplay between magnetic and dielectric phenomena at transition metal oxide interfaces
D. Schumacher (2013), IV, 128 pp
ISBN: 978-3-89336-855-6

Band / Volume 57
Single $NdPc_2$ Molecules on Surfaces: Adsorption, Interaction, and Molecular Magnetism
S. Fahrendorf (2013), viii, 100 pp
ISBN: 978-3-89336-856-3

Band / Volume 58
Heyd-Scuseria-Ernzerhof Screened-Exchange Hybrid Functional for Complex Materials: All-Electron Implementation and Application
M. Schlipf (2013), XV, 170 pp
ISBN: 978-3-89336-857-0

Band / Volume 59
Orbital-dependent exchange-correlation functionals in density-functional theory realized by the FLAPW method
M. Betzinger (2013), vi, 173 pp
ISBN: 978-3-89336-858-7

Band / Volume 60
Structural influences on electrical transport in nanostructures
R. D. Frielinghaus (2013), viii, 190 pp
ISBN: 978-3-89336-867-9

Band / Volume 61
Study of intermolecular interactions in hetero-organic thin films
B. Stadtmüller (2013), viii, 198 pp
ISBN: 978-3-89336-871-6

Band / Volume 62
Structure, magnetism and excitations in some Mn-based magnetocaloric effect compounds
M. Gottschlich (2013), 175 pp
ISBN: 978-3-89336-874-7

Band / Volume 63
Neutron Scattering
Lectures of the JCNS Laboratory Course held at Forschungszentrum Jülich and the research reactor FRM II of TU Munich
edited by Th. Brückel, G. Heger, D. Richter, G. Roth and R. Zorn (2013),
ca 350 pages
ISBN: 978-3-89336-880-8

Schriften des Forschungszentrums Jülich
Reihe Schlüsseltechnologien / Key Technologies

Band / Volume 64
Neutron Scattering
Experiment Manuals of the JCNS Laborator Course held at Forschungszentrum Jülich and the research reactorFRM II of TU Munich
edited by Th. Brückel, G. Heger, D. Richter, G. Roth and R. Zorn (2013),
ca. 150 pages
ISBN: 978-3-89336-881-5

Band / Volume 65
Solutions of Exercises in "An Introduction to Dynamics of Colloids"
J. K. G. Dhont, K. Kang (2013), 143 pp
ISBN: 978-3-89336-882-2

Band / Volume 66
Strukturelle und chemische Charakterisierung von selbst-assemblierten Monolagen organischer Moleküle auf Oberflächen
M. Müller (2013), 168 pp
ISBN: 978-3-89336-883-9

Band / Volume 67
Adsorption of (hetero-)organic Phthalocyanine and PTCDA thin films on Ag(111)
C. Kleimann (2013), iv, 149 pp
ISBN: 978-3-89336-888-4

Band / Volume 68
High-energy high-momentum surface spin waves of ultrathin epitaxial 3d transition metal films
R. Jayaraman (2013), ix, 135 pp
ISBN: 978-3-89336-890-7

Band / Volume 69
Magnetic Oxide Heterostructures: EuO on Cubic Oxides and on Silicon
C. Caspers (2013), xiii, 153 pp
ISBN: 978-3-89336-891-4

Band / Volume 70
Femtosecond Spin Dynamics in Magnetic Multilayers Employing High Harmonics of Laser Radiation
D. Rudolf (2013), vi, 121 pp
ISBN: 978-3-89336-894-5

Weitere ***Schriften des Verlags im Forschungszentrum Jülich*** unter
http://wwwzb1.fz-juelich.de/verlagextern1/index.asp

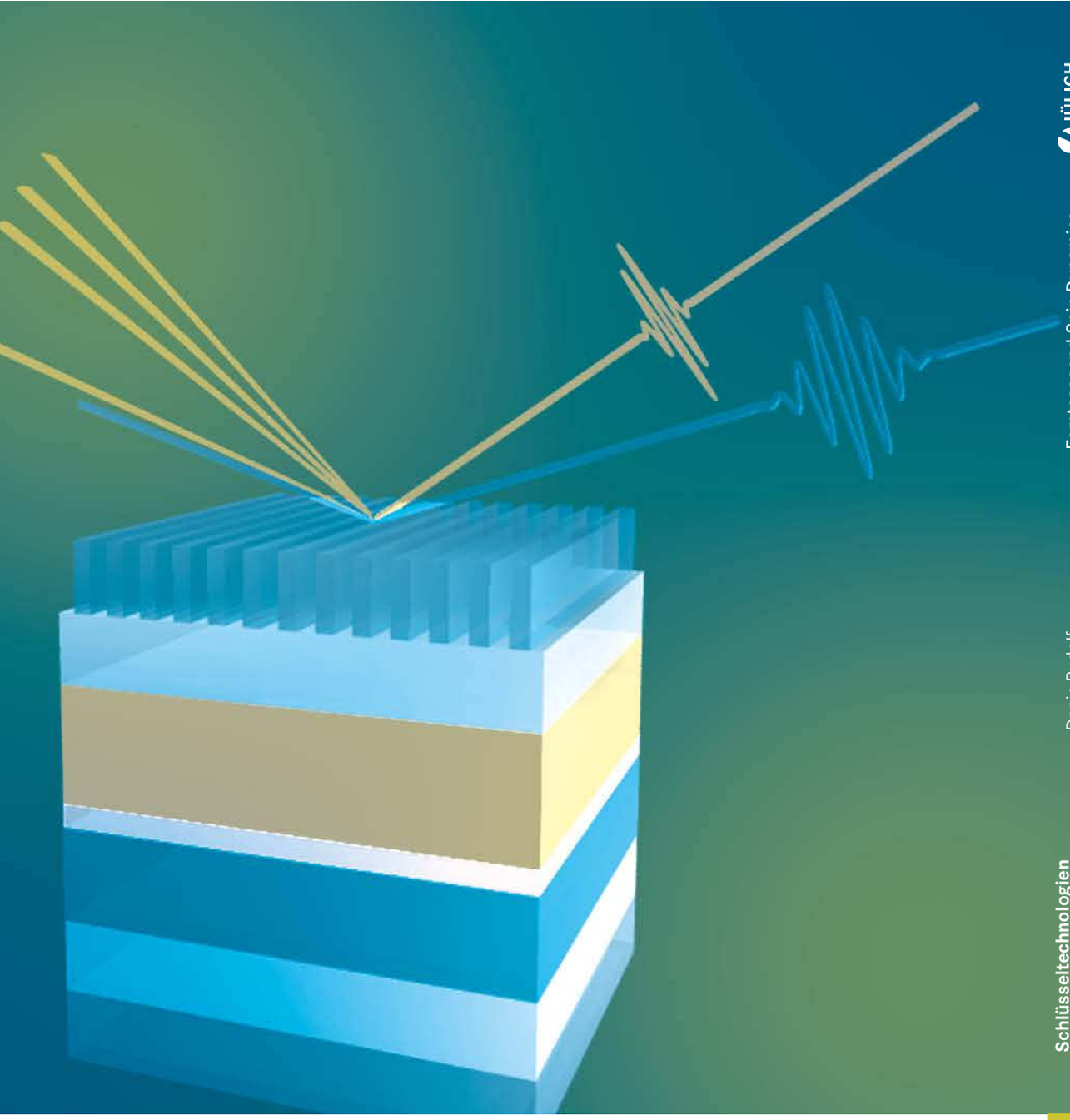

Femtosecond Spin Dynamics

Denis Rudolf

JÜLICH
FORSCHUNGSZENTRUM

Schlüsseltechnologien
Key Technologies

Schlüsseltechnologien / Key Technologies
Band / Volume 70
ISBN 978-3-89336-894-5

JÜLICH
FORSCHUNGSZENTRUM

70

Member of the Helmholtz Association

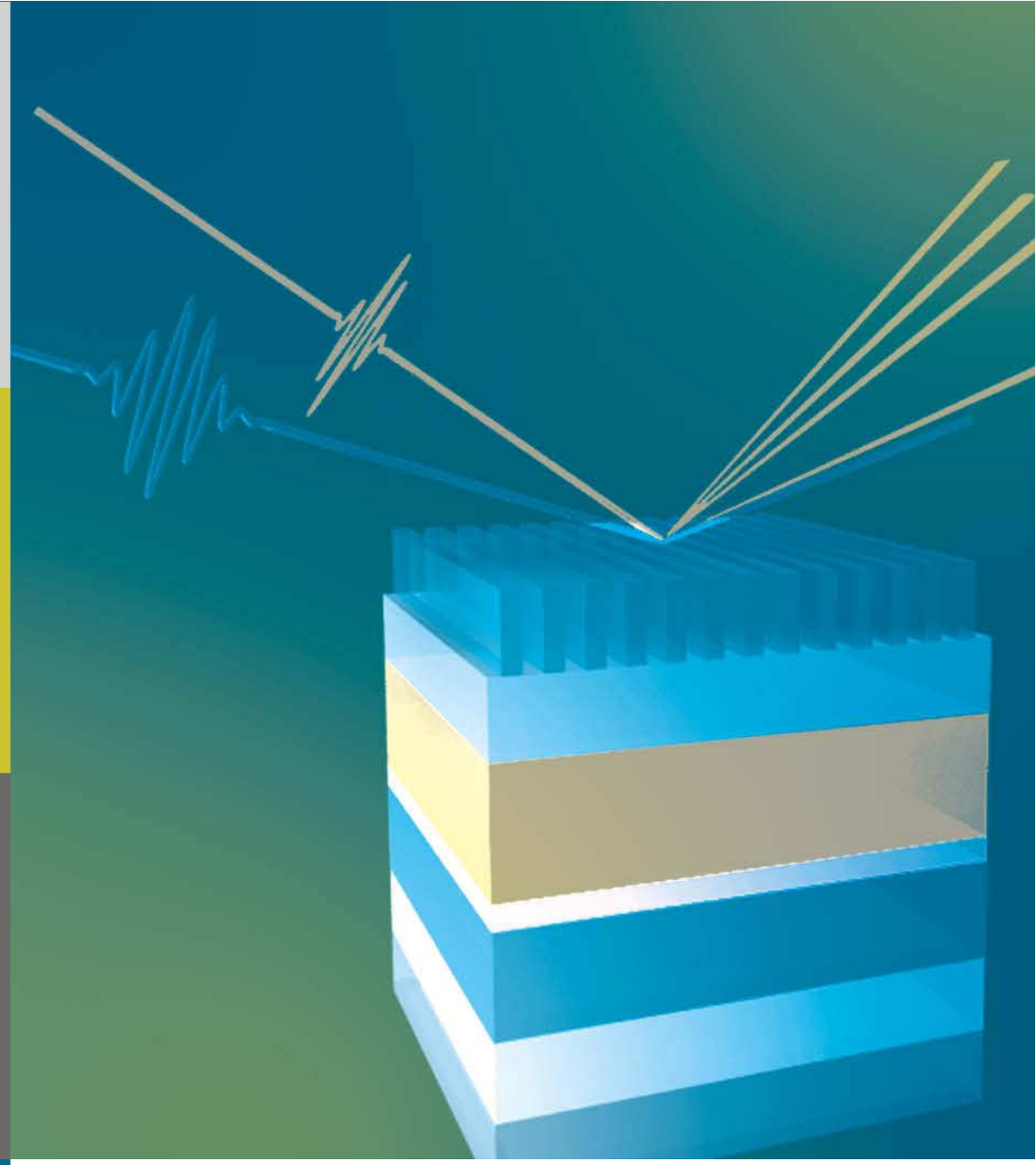

Femtosecond Spin Dynamics in Magnetic Multilayers Employing High Harmonics of Laser Radiation

Denis Rudolf

JÜLICH
FORSCHUNGSZENTRUM